2012 Volume 3

The Journal on Advanced Studies in Theoretical and Experimental Physics, including Related Themes from Mathematics

PROGRESS IN PHYSICS

"All scientists shall have the right to present their scientific research results, in whole or in part, at relevant scientific conferences, and to publish the same in printed scientific journals, electronic archives, and any other media."
— Declaration of Academic Freedom, Article 8

ISSN 1555-5534

The Journal on Advanced Studies in Theoretical and Experimental Physics, including Related Themes from Mathematics

PROGRESS IN PHYSICS

A quarterly issue scientific journal, registered with the Library of Congress (DC, USA). This journal is peer reviewed and included in the abstracting and indexing coverage of: Mathematical Reviews and MathSciNet (AMS, USA), DOAJ of Lund University (Sweden), Zentralblatt MATH (Germany), Scientific Commons of the University of St. Gallen (Switzerland), Open-J-Gate (India), Referativnyi Zhurnal VINITI (Russia), etc.

Electronic version of this journal:
http://www.ptep-online.com

Postal Address

Department of Mathematics and Science,
University of New Mexico,
705 Gurley Ave., Gallup, NM 87301, USA

ISSN: 1555-5534 (print)
ISSN: 1555-5615 (online)

Standard Address Number: 297-5092
Printed in the United States of America

JULY 2012 **VOLUME 3**

CONTENTS

Information for Authors and Subscribers

Progress in Physics has been created for publications on advanced studies in theoretical and experimental physics, including related themes from mathematics and astronomy. All submitted papers should be professional, in good English, containing a brief review of a problem and obtained results.

All submissions should be designed in LaTeX format using *Progress in Physics* template. This template can be downloaded from *Progress in Physics* home page http://www.ptep-online.com. Abstract and the necessary information about author(s) should be included into the papers. To submit a paper, mail the file(s) to the Editor-in-Chief.

All submitted papers should be as brief as possible. We accept brief papers, no larger than 8 typeset journal pages. Short articles are preferable. Large papers can be considered in exceptional cases to the section *Special Reports* intended for such publications in the journal. Letters related to the publications in the journal or to the events among the science community can be applied to the section *Letters to Progress in Physics*.

All that has been accepted for the online issue of *Progress in Physics* is printed in the paper version of the journal. To order printed issues, contact the Editors.

This journal is non-commercial, academic edition. It is printed from private donations. (Look for the current author fee in the online version of the journal.)

Characterisation of Low Frequency Gravitational Waves from Dual RF Coaxial-Cable Detector: Fractal Textured Dynamical 3-Space

Reginald T. Cahill

School of Chemical and Physical Sciences, Flinders University, Adelaide 5001, Australia
E-mail: Reg.Cahill@flinders.edu.au

Experiments have revealed that the Fresnel drag effect is not present in RF coaxial cables, contrary to a previous report. This enables a very sensitive, robust and compact detector, that is 1st order in v/c and using one clock, to detect the dynamical space passing the earth, revealing the sidereal rotation of the earth, together with significant wave/turbulence effects. These are "gravitational waves", and previously detected by Cahill 2006, using an Optical-Fibre – RF Coaxial Cable Detector, and Cahill 2009, using a preliminary version of the Dual RF Coaxial Cable Detector. The gravitational waves have a 1/f spectrum, implying a fractal structure to the textured dynamical 3-space.

1 Introduction

Data from a new gravitational wave experiment is reported*, revealing a fractal 3-space, flowing past the earth at ∼500 km/s. The wave/turbulence or "gravitational waves" have a significant magnitude, and are now known to have been detected numerous times over the last 125 years. The detector uses a single clock with RF EM waves propagating through dual coaxial cables, and is 1st order in v/c. The detector is sensitive, simple to operate, robust and compact. It uses the surprising discovery that there is no Fresnel drag effect in coaxial cables, whereas there is in gases, optical fibres, liquids etc. Data from an analogous detector using optical fibres and single coaxial cables was reported in 2006 [1, 2]. Because of the discovery reported herein that detector calibration has now been correctly redetermined. Results from Michelson-Morley [3, 4], Miller [5], Torr and Kolen [6] and DeWitte [7], are now in remarkable agreement with the velocity of absolute motion of the earth determined from NASA spacecraft earth-flyby Doppler shift data [8, 9], all revealing a light/EM speed anisotropy of some 486km/s in the direction RA=4.29^h, Dec=-75.0°: that speed is ∼300,000-500 km/s for radiation travelling in that direction, and ∼300,000+500 km/s travelling in the opposite, northerly direction: a significant observed anisotropy that physics has ignored. The actual daily average velocity varies with days of the year because of the orbital motion of the earth - the aberration effect discovered by Miller, but shows fluctuations over all time scales.

In 2002 it was discovered that the Michelson-Morley 1887 light-speed anisotropy experiment, using the interferometer in gas mode, had indeed detected anisotropy, by taking account of both the Lorentz length contraction effect for the interferometer arms, and the refractive index effect of the air in the light paths [3, 4]. These gas-mode interferometer experiments show the difference between Lorentzian Relativity (LR) and Special Relativity (SR). In LR the length contraction effect is caused by motion of a rod, say, through the dynamical 3-space, whereas in SR the length contraction is only a perspective effect, supposedly occurring only when the rod is moving relative to an observer. This was further clarified when an exact mapping between Galilean space and time coordinates and the Minkowski-Einstein spacetime coordinates was recently discovered [10].

The Michelson interferometer, having the calibration constant $k^2 = (n^2-1)(n^2-2)$ where n is the refractive index of the light-path medium, has zero sensitivity to EM anisotropy and gravitational waves when operated in vacuum-mode ($n = 1$). Fortunately the early experiments had air present in the light paths†. A very compact and cheap Michelson interferometric anisotropy and gravitational wave detector may be constructed using optical fibres [11], but for most fibres $n \approx \sqrt{2}$ near room temperature, and so needs to be operated at say 0°C. The $(n^2 - 2)$ factor is caused by the Fresnel drag [12]. The detection of light speed anisotropy - revealing a flow of space past the detector, is now entering an era of precision measurements, as reported herein. These are particularly important because experiments have shown large turbulence effects in the flow, and are beginning to characterise this turbulence. Such turbulence can be shown to correspond to what are, conventionally, known as gravitational waves, although not those implied by General Relativity, but more precisely are revealing a fractal structure to dynamical 3-space.

*This report is from the Gravitational Wave Detector Project at Flinders University.

†Michelson and Morley implicitly assumed that $k^2 = 1$, which considerably overestimated the sensitivity of their detector by a factor of ∼ 1700 (air has $n = 1.00029$). This error lead to the invention of "spacetime" in 1905. Miller avoided any assumptions about the sensitivity of his detector, and used the earth orbit effect to estimate the calibration factor k^2 from his data, although even that is now known to be incorrect: the sun 3-space inflow component was unknown to Miller. It was only in 2002 that the design flaw in the Michelson interferometer was finally understood [3, 4].

2 Fresnel Drag

The detection and characterisation of these wave/turbulence effects requires only the development of small and cheap detectors, as these effects are large. However in all detectors the EM signals travel through a dielectric, either in bulk or optical fibre or through RF coaxial cables. For this reason it is important to understand the so-called Fresnel drag effect. In optical fibres the Fresnel drag effect has been established, as this is important in the operation of Sagnac optical fibre gyroscopes, for only then is the calibration independent of the fibre refractive index, as observed. The Fresnel drag effect is a phenomenological formalism that characterises the effect of the absolute motion of the propagation medium, say a dielectric, upon the speed of the EM radiation relative to that medium.

The Fresnel drag expression is that a dielectric in absolute motion through space at speed v, relative to space itself, causes the EM radiation to travel at speed

$$V(v) = \frac{c}{n} + v\left(1 - \frac{1}{n^2}\right) \qquad (1)$$

wrt the dielectric, when V and v have the same direction. Here n is the dielectric refractive index. The 2nd term is known as the Fresnel drag, appearing to show that the moving dielectric "drags" the EM radiation, although this is a misleading interpretation; see [13] for a derivation*. If the Fresnel drag is always applicable then, as shown herein, a 1st order in v/c detector requires two clocks, though not necessarily synchronised, but requiring a rotation of the detector arm to extract the v-dependent term. However, as we show herein, if the Fresnel drag is not present in RF coaxial cables, then a detector 1st order in v/c and using one clock, can detect and characterise the dynamical space. In [13] it was incorrectly concluded that the Fresnel effect was present in RF coaxial cables, for reasons related to the temperature effects, and discussed later.

3 Dynamical 3-Space

We briefly outline the dynamical modelling of 3-space. It involves the space velocity field $\mathbf{v}(\mathbf{r}, t)$, defined relative to an observer's frame of reference.

$$\nabla \cdot \left(\frac{\partial \mathbf{v}}{\partial t} + (\mathbf{v}\cdot\nabla)\,\mathbf{v}\right) + \frac{\alpha}{8}\left((\mathrm{tr}D)^2 - \mathrm{tr}(D)^2\right) + .. = -4\pi G\rho \qquad (2)$$

$\nabla \times \mathbf{v} = \mathbf{0}$ and $D_{ij} = \partial v_i \partial x_j$. The velocity field $\mathbf{v}$ describes classically the time evolution of the substratum quantum foam. The bore hole g anomaly data has revealed $\alpha = 1/137$, the fine structure constant. The matter acceleration is found by determining the trajectory of a quantum matter wavepacket. This is most easily done by maximising the proper travel time τ:

$$\tau = \int dt \sqrt{1 - \frac{\mathbf{v}_R^2(\mathbf{r}_0(t), t)}{c^2}} \qquad (3)$$

where $\mathbf{v}_R(\mathbf{r}_o(t), t) = \mathbf{v}_o(t) - \mathbf{v}(\mathbf{r}_o(t), t)$, is the velocity of the wave packet, at position $\mathbf{r}_0(t)$, wrt the local space – a neo-Lorentzian Relativity effect. This ensures that quantum waves propagating along neighbouring paths are in phase, and so interfere constructively. This maximisation gives the quantum matter geodesic equation for $\mathbf{r}_0(t)$

$$\mathbf{g} = \frac{\partial \mathbf{v}}{\partial t} + (\mathbf{v}\cdot\nabla)\mathbf{v} + (\nabla\times\mathbf{v})\times\mathbf{v}_R - \frac{\mathbf{v}_R}{1 - \dfrac{\mathbf{v}_R^2}{c^2}}\,\frac{1}{2}\,\frac{d}{dt}\left(\frac{\mathbf{v}_R^2}{c^2}\right) + ... \qquad (4)$$

with $\mathbf{g} \equiv d\mathbf{v}_o/dt = d^2\mathbf{r}_o/dt^2$. The 1st term in $\mathbf{g}$ is the Euler space acceleration $\mathbf{a}$, the 2nd term explains the Lense-Thirring effect, when the vorticity is non-zero, and the last term explains the precession of orbits. While the velocity field has been repeatedly detected since the Michelson-Morley 1887 experiment, the best detection has been using

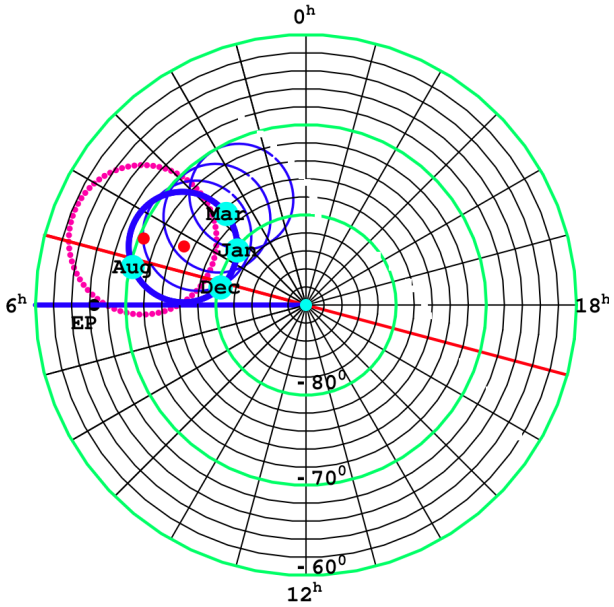

Fig. 1: South celestial pole region. The dot (red) at RA=4.29^h, Dec=-75°, and with speed 486 km/s, is the direction of motion of the solar system through space determined from spacecraft earth-flyby Doppler shifts [9], revealing the EM radiation speed anisotropy. The thick (blue) circle centred on this direction is the observed velocity direction for different days of the year, caused by earth orbital motion and sun space inflow. The corresponding results from Miller gas-mode interferometer are shown by 2nd dot (red) and its aberration circle (red dots) [5]. For March the velocity is RA=2.75^h, Dec=-76.6°, and with speed 499.2 km/s, see Table 2 of [9].

*The Fresnel Drag in (1) can be "derived" from the Special Relativity velocity-addition formula, but there v is the speed of the dielectric wrt to the observer, and as well common to both dielectrics and coaxial cables.

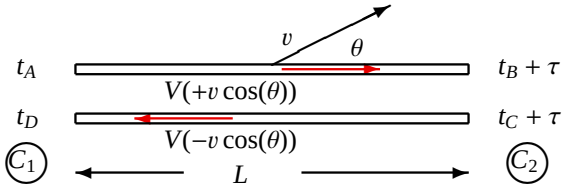

Fig. 2: Schematic layout for measuring the one-way speed of light in either free-space, optical fibres or RF coaxial cables, without requiring the synchronisation of the clocks C_1 and C_2: here τ is the unknown offset time between the clocks. V is the speed of EM radiation wrt the apparatus, with or without the Fresnel drag in (1), and v is the speed of the apparatus through space, in direction θ. DeWitte used this technique in 1991 with 1.5 km RF cables and Cesium atomic clocks [7]. In comparison with data from spacecraft earth-flyby Doppler shifts [9] this experiments confirms that there is no Fresnel drag effect in RF coaxial cables.

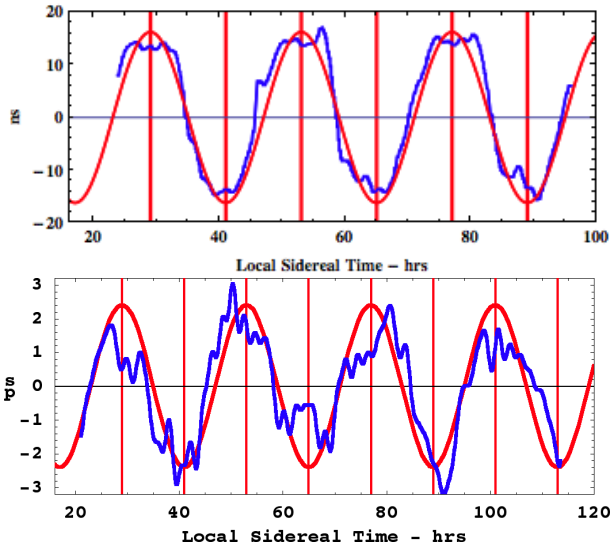

Fig. 3: Top: Data from the 1991 DeWitte NS horizontal coaxial cable experiment, L = 1.5 km, n = 1.5, using the arrangement shown in Fig. 2. The time variation of ~ 28 ns is consistent with the Doppler shift results with speed 500 km/s, but using Dec=-65°: the month for this data is unknown, and the vertical red lines are at RA=5^h. If a Fresnel drag effect is included the speed would have to be 1125 km/s, in disagreement with the Doppler shift data, demonstrating that there is no Fresnel drag in coaxial cables. Bottom: Dual coaxial cable detector data from May 2009 using the technique in Fig. 5 and without looping: L = 20 m, Doppler shift data predicts Dec= −77°, v = 480 km/s giving a sidereal dynamic range of 5.06 ps, very close to that observed. The vertical red lines are at RA=5^h. In both data sets we see the earth sidereal rotation effect together with significant wave/turbulence effects.

the spacecraft earth-flyby Doppler shift data [9], see Fig1. The above reveals gravity to be an emergent phenomenon where quantum matter waves are refracted by the time dependent and inhomogeneous 3-space velocity field. The α-term in (2) explains the so-called "dark matter" effects: if $\alpha \to 0$ and $v_R/c \to 0$ we recover Newtonian gravity, for then $\nabla\cdot\mathbf{g} = -4\pi G\rho$ [12]. Note that the relativistic term in (4) arises from the quantum matter dynamics – not from the space dynamics.

4 Gravitational Waves: Dynamical Fractal 3-Space

Eqn. (3) for the elapsed proper time maybe written in differential form as

$$d\tau^2 = dt^2 - \frac{1}{c^2}(d\mathbf{r}(t) - \mathbf{v}(\mathbf{r}(t), t)dt)^2 = g_{\mu\nu}(x)dx^\mu dx^\nu \qquad (5)$$

which introduces a curved spacetime metric $g_{\mu\nu}$ for which the geodesics are the quantum matter trajectories when freely propagating through the dynamical 3-space. Gravitational wave are traditionally thought of as "ripples" in the spacetime metric $g_{\mu\nu}$. But the discovery of the dynamical 3-space means that they are more appropriately understood to be turbulence effects of the dynamical 3-space vector $\mathbf{v}$, because it is $\mathbf{v}$ that is directly detectable, whereas $g_{\mu\nu}$ is merely an induced mathematical artefact. When the matter density $\rho = 0$, (2) will have a time-dependent fractal structured solutions, as there is no length scale. The wave/turbulence effects reported herein confirm that prediction, see Fig. 9.

5 First Order in v/c Speed of EMR Experiments

Fig. 2 shows the arrangement for measuring the one-way speed of light, either in vacuum, a dielectric, or RF coaxial cable. It is usually argued that one-way speed of light measurements are not possible because the clocks C_1 and C_2 cannot be synchronised. However this is false, and at the same time shows an important consequence of (1). In the upper part of Fig. 2 the actual travel time t_{AB} from A to B is determined by

$$V(v\cos(\theta))t_{AB} = L + v\cos(\theta)t_{AB} \qquad (6)$$

where the 2nd term comes from the end B moving an additional distance $v\cos(\theta)t_{AB}$ during time interval t_{AB}. Then

$$t_{AB} = \frac{L}{V(v\cos(\theta)) - v\cos(\theta)} = \frac{nL}{c} + \frac{v\cos(\theta)L}{c^2} + .. \qquad (7)$$

$$t_{CD} = \frac{L}{V(v\cos(\theta)) + v\cos(\theta)} = \frac{nL}{c} - \frac{v\cos(\theta)L}{c^2} + .. \qquad (8)$$

on using (1), i.e. assuming the validity of the Fresnel effect, and expanding to 1st oder in v/c. However if there is no Fresnel drag effect then we obtain

$$t_{AB} = \frac{L}{V(v\cos(\theta)) - v\cos(\theta)} = \frac{nL}{c} + \frac{v\cos(\theta)Ln^2}{c^2} + .. \qquad (9)$$

$$t_{CD} = \frac{L}{V(v\cos(\theta)) + v\cos(\theta)} = \frac{nL}{c} - \frac{v\cos(\theta)Ln^2}{c^2} + .. \qquad (10)$$

The important observation is that the v/c terms are independent of the dielectric refractive index n in (7) and (8), but

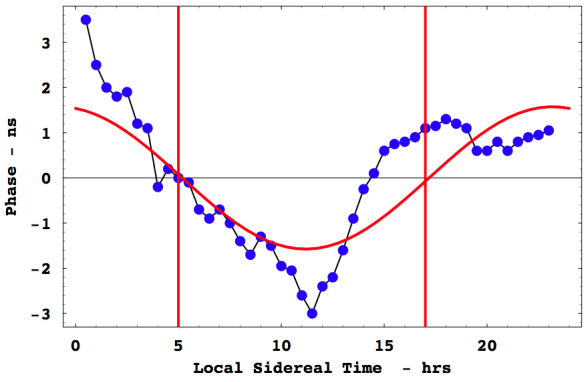

Fig. 4: Data from the 1981 Torr-Kolen experiment at Logan, Utah [6]. The data shows variations in travel times (ns), for local sidereal times, of an RF signal travelling through 500 m of coaxial cable orientated in an EW direction. The red curve is sidereal effect prediction for February, for a 3-space speed of 480 km/s from the direction, RA=5^h, Dec=-70°.

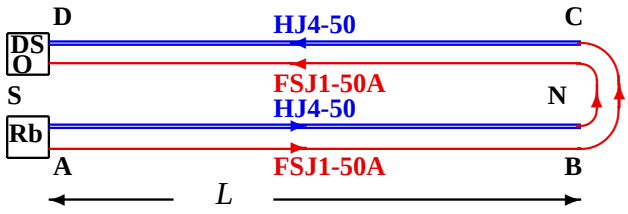

Fig. 5: Because Fresnel drag is absent in RF coaxial cables this dual cable setup, using one clock, is capable of detecting the absolute motion of the detector wrt to space, revealing the sidereal rotation effect as well as wave/turbulence effects. In the 1st trial of this detector this arrangement was used, with the cables laid out on a laboratory floor, and preliminary results are shown in Figs. 3. In the new design the cables in each circuit are configured into 8 loops, as in Fig. 6, giving $L = 8 \times 1.85$ m $= 14.8$ m. In [1] a version with optical fibres in place of the HJ4-50 coaxial cables was used, see Fig. 11. There the optical fibre has a Fresnel drag effect while the coaxial cable did not. In that experiment optical-electrical converters were used to modulate/demodulate infrared light.

have an n^2 dependence in (9) and (10), in the absence of the Fresnel drag effect.

If the clocks are not synchronised then t_{AB} is not known, but by changing direction of the light path, that is varying θ, the magnitude of the 2nd term may be separated from the magnitude of the 1st term, and v and its direction determined. The clocks may then be synchronised. For a small detector the change in θ can be achieved by a direct rotation. Results (7) and (8), or (9) and (10), have been exploited in various detector designs.

6 DeWitte 1st Order in v/c Detector

The DeWitte $L = 1.5$ km RF coaxial cable experiment, Brussels 1991, was a double 1st order in v/c detector, using the scheme in Fig.2, and employing 3 Caesium atomic clocks at each end, and overall measuring $t_{AB} - t_{CD}$. The orientation was NS and rotation was achieved by that of the earth [7].

$$t_{AB} - t_{CD} = \frac{2v\cos(\theta)Ln^2}{c^2} \qquad (11)$$

The dynamic range of $\cos(\theta)$ is $2\sin(\lambda-\beta)\cos(\delta)$, caused by the earth rotation, where λ is the latitude of the detector location, β is the local inclination to the horizontal, here $\beta = 0$, and δ is the declination of **v**. The data shows remarkable agreement with the velocity vector from the flyby Doppler shift data, see Fig. 3. However if there is Fresnel drag in the coaxial cables, there would be no n^2 factor in (11), and the DeWitte data would give a much larger speed $v = 1125$ km/s, in strong disagreement with the flyby data.

7 Torr and Kolen 1st Order in v/c Detector

A one-way coaxial cable experiment was performed at the Utah University in 1981 by Torr and Kolen [6]. This involved two Rb clocks placed approximately 500 m apart with a 5 MHz sinewave RF signal propagating between the clocks via a nitrogen filled coaxial cable buried in the ground and maintained at a constant pressure of ~2 psi. Torr and Kolen observed variations in the one-way travel time, as shown in Fig.4 by the data points. The theoretical predictions for the Torr-Kolen experiment for a cosmic speed of 480 km/s from the direction, RA=5^h, Dec=-70°, as shown in Fig. 4. The maximum/minimum effects occurred, typically, at the predicted times. Torr and Kolen reported fluctuations in both the magnitude, from 1–3 ns, and time of the maximum variations in travel time, just as observed in all later experiments, namely wave effects.

8 Dual RF Coaxial Cable Detector

The Dual RF Coaxial Cable Detector exploits the Fresnel drag anomaly, in that there is no Fresnel drag effect in RF coaxial cables. Then from (9) and (10) the round trip travel time is, see Fig. 5,

$$t_{AB} + t_{CD} = \frac{2nL}{c} + \frac{v\cos(\theta)L(n_1^2 - n_2^2)}{c^2} + .. \qquad (12)$$

where n_1 and n_2 are the effective refractive indices for the two different RF coaxial cables, with two separate circuits to reduce temperature effects. Shown in Fig. 6 is a photograph. The Andrews Phase Stabilised FSJ1-50A has $n_1 = 1.19$, while the HJ4-50 has $n_2 = 1.11$. One measures the travel time difference of two RF signals from a Rubidium frequency standard (Rb) with a Digital Storage Oscilloscope (DSO). In each circuit the RF signal travels one-way in one type of coaxial cable, and returns via a different kind of coaxial cable. Two circuits are used so that temperature effects cancel - if a temperature change alters the speed in one type of cable, and so the travel time, that travel time change is the

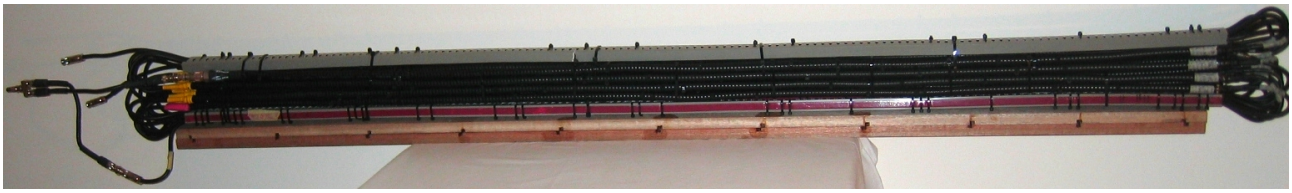

Fig. 6: Photograph of the RF coaxial cables arrangement, based upon 16 ×1.85 m lengths of phase stabilised Andrew HJ4-50 coaxial cable. These are joined to 16 lengths of phase stabilised Andrew FSJ1-50A cable, in the manner shown schematically in Fig. 5. The 16 HJ4-50 coaxial cables have been tightly bound into a 4×4 array, so that the cables, locally, have the same temperature, with cables in one of the circuits embedded between cables in the 2nd circuit. This arrangement of the cables permits the cancellation of temperature differential effects in the cables. A similar array of the smaller diameter FSJ1-50A cables is located inside the grey-coloured conduit boxes.

same in both circuits, and cancels in the difference. The travel time difference of the two circuits at the DSO is

$$\Delta t = \frac{2v\cos(\theta)L(n_1^2 - n_2^2)}{c^2} + .. \qquad (13)$$

If the Fresnel drag effect occurred in RF coaxial cables, we would use (7) and (8) instead, and then the $n_1^2 - n_2^2$ term is replaced by 0, i.e. there is no 1st order term in v. That is contrary to the actual data in Figs. 3 and 7.

The preliminary layout for this detector used cables laid out as in Fig.5, and the data is shown in Fig.3. In the compact design the Andrew HJ4-50 cables are cut into 8×1.85 m shorter lengths in each circuit, corresponding to a net length of $L = 8 \times 1.85 = 14.8$ m, and the Andrew FSJ1-50A cables are also cut, but into longer lengths to enable joining. However the curved parts of the Andrew FSJ1-50A cables contribute only at 2nd order in v/c. The apparatus was horizontal, $\beta = 0$, and orientated NS, and used the rotation of the earth to change the angle θ. The dynamic range of $\cos(\theta)$, caused by the earth rotation only, is again $2\sin(\lambda - \beta)\cos(\delta)$, where $\lambda = -35^\circ$ is the latitude of Adelaide. Inclining the detector at angle $\beta = \lambda$ removes the earth rotation effect, as now the detector arm is parallel to the earth's spin axis, permitting a more accurate characterisation of the wave effects.

9 Temperature Effects

The cable travel times and the DSO phase measurements are temperature dependent, and these effects are removed from the data, rather than attempt to maintain a constant temperature, which is impractical because of the heat output of the Rb clock and DSO. The detector was located in a closed room in which the temperature changed slowly over many days, with variations originating from changing external weather driven temperature changes. The temperature of the detector was measured, and it was assumed that the timing errors were proportional to changes in that one measured temperature. These timing errors were some 30ps, compared to the true signal of some 8ps. Because the temperature timing errors are much larger, the temperature induced $\Delta t = a + b\Delta T$ was fitted to the timing data, and the coefficients a and b determined. Then this Δt time series was subtracted from the data, leaving the actual required phase data. This is particularly effective as the temperature variations had a distinctive signature. The resulting data is shown in Fig.8. In an earlier test for the Fresnel drag effect in RF coaxial cables [13] the technique for removing the temperature induced timing errors was inadequate, resulting in the wrong conclusion that there was Fresnel drag in RF coaxial cables.

10 Dual RF Coaxial Cable Detector: Data

The phase data, after removing the temperature effects, is shown in Fig. 8 (top), with the data compared with predictions for the sidereal effect only from the flyby Doppler shift data. As well that data is separated into two frequency bands (bottom), so that the sidereal effect is partially separated from the

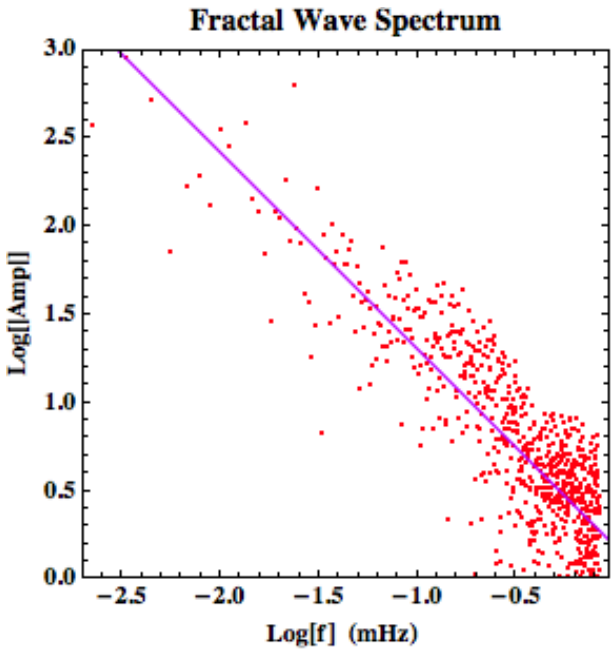

Fig. 7: Log-Log plot of the data (top) in Fig. 7, with the straight line being $A \propto 1/f$, indicating a $1/f$ fractal wave spectrum. The interpretation for this is the 3-space structure shown in Fig. 9.

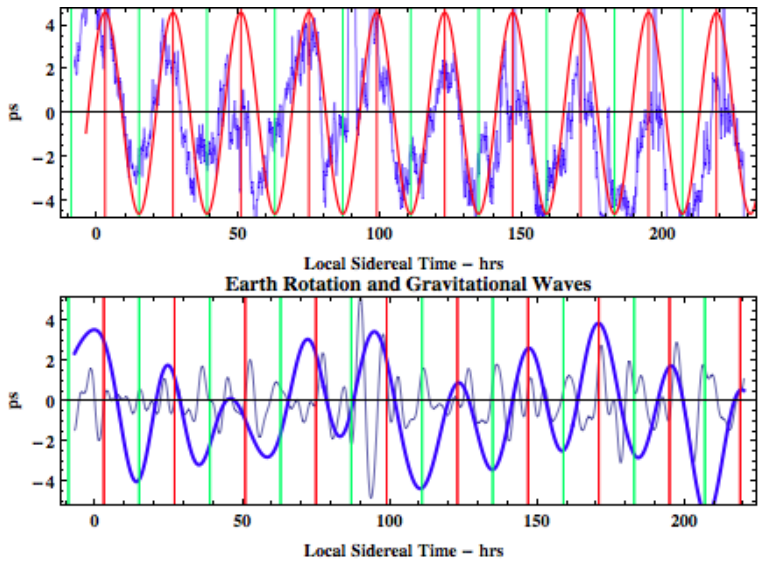

Fig. 8: Top: Travel time differences (ps) between the two coaxial cable circuits in Fig. 5, orientated NS and horizontal, over 9 days (March 4-12, 2012, Adelaide) plotted against local sidereal time. Sinewave, with dynamic range 8.03 ps, is prediction for sidereal effect from flyby Doppler shift data for RA=2.75^h (shown by red fudicial lines), Dec=-76.6°, and with speed 499.2 km/s, see Table 2 of [9], also shown in from Fig. 1. Data shows sidereal effect and significant wave/turbulence effects. Bottom: Data filtered into two frequency bands 3.4×10^{-3} mHz $< f <$ 0.018 mHz (81.4 $h > T >$ 15.3 h) and 0.018 mHz $< f <$ 0.067 mHz (15.3 $h > T >$ 4.14 h), showing more clearly the earth rotation sidereal effect (plus vlf waves) and the turbulence without the sidereal effect. Frequency spectrum of top data is shown in Fig. 7.

gravitational wave effect, *viz* 3-space wave/turbulence. Being 1st order in v/c it is easily determined that the space flow is from the southerly direction, as also reported in [1]. Miller reported the same sense, i.e. the flow is essentially from S to N, though using a 2nd order detector that is more difficult to determine. The frequency spectrum of this data is shown in Fig. 7, revealing a fractal $1/f$ form. This implies the fractal structure of the 3-space indicated in Fig. 9.

11 Optical Fibre RF Coaxial Cable Detector

An earlier 1st order in v/c gravitational wave detector design is shown in Fig. 11, with some data shown in Fig. 10. Only now is it known why that detector also worked, namely that there is a Fresnel drag effect in the optical fibres, but not in the RF coaxial cable. Then the travel time difference, measured at the DSO is given by

$$\Delta t = \frac{2v\cos(\theta)L(n_1^2 - 1)}{c^2} + .. \qquad (14)$$

where n_1 is the effective refractive index of the RF coaxial cable. Again the data is in remarkable agreement with the flyby determined **v**.

12 2nd Order in v/c Gas-Mode Detectors

It is important that the gas-mode 2nd order in v/c data from Michelson and Morley, 1887, and from Miller, 1925/26, be reviewed in the light of the recent experiments and flyby data. Shown in Fig. 12 (top) is Miller data from September 16, 1925, $4^h40'$ Local Sidereal Time (LST) - an average of data from 20 turns of the gas-mode Michelson interferometer. Plot and data after fitting and then subtracting both the temperature drift and Hicks effects from both, leaving the expected si-

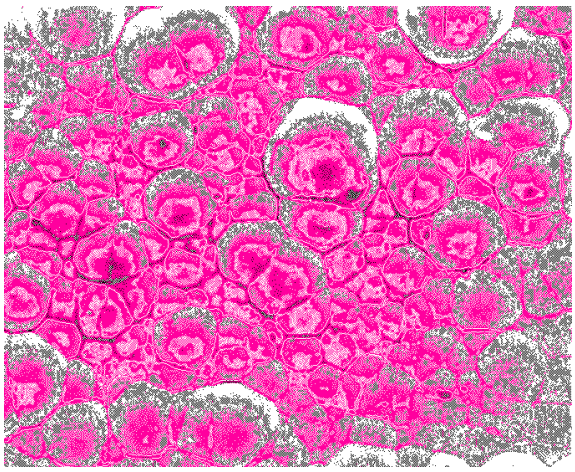

Fig. 9: Representation of the fractal wave data as a revealing the fractal textured structure of the 3-space, with cells of space having slightly different velocities, and continually changing, and moving wrt the earth with a speed of ~500 km/s.

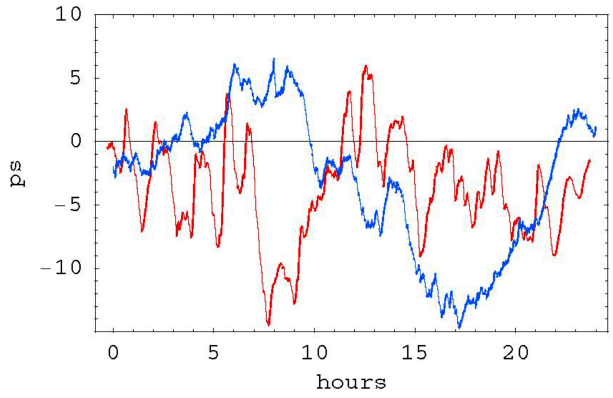

Fig. 10: Phase difference (ps), with arbitrary zero, versus local time data plots from the Optical Fibre - Coaxial Cable Detector, see Fig. 11 and [1, 2], showing the sidereal time effect and significant wave/turbulence effects. The plot (blue) with the most easily identified minimum at ~17 hrs local Adelaide time is from June 9, 2006, while the plot (red) with the minimum at ~8.5 hrs local time is from August 23, 2006. We see that the minimum has moved forward in time by approximately 8.5 hrs. The expected sidereal shift for this 65 day difference, without wave effects, is 4.3 hrs, to which must be added another ~1h from the aberration effects shown in Fig. 1, giving 5.3hrs, in agreement with the data, considering that on individual days the min/max fluctuates by ±2hrs. This sidereal time shift is a critical test for the detector. From the flyby Doppler data we have for August RA=5^h, Dec=-70°, and speed 478 km/s, see Table 2 of [9], the predicted sidereal effect dynamic range to be 8.6 ps, very close to that observed.

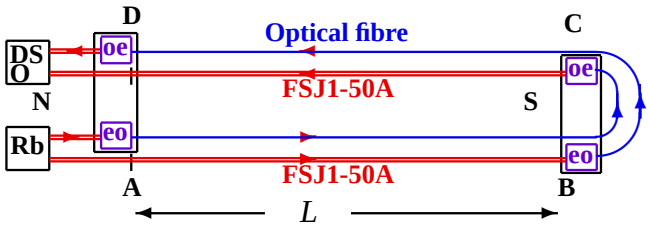

Fig. 11: Layout of the optical fibre - coaxial cable detector, with L = 5.0 m. 10 MHz RF signals come from the Rubidium atomic clock (Rb). The Electrical to Optical converters (EO) use the RF signals to modulate 1.3 μm infrared signals that propagate through the single-mode optical fibres. The Optical to Electrical converters (OE) demodulate that signal and give the two RF signals that finally reach the Digital Storage Oscilloscope (DSO), which measures their phase difference. The key effects are that the propagation speeds through the coaxial cables and optical fibres respond differently to their absolute motion through space, with no Fresnel drag in the coaxial cables, and Fresnel drag effect in the optical fibres. Without this key difference this detector does not work.

nusoidal form. The error bars are determined as the rms error in this fitting procedure, and show how exceptionally small were the errors, and which agree with Miller's claim for the errors. Best result from the Michelson-Morley 1887 data - an average of 6 turns, at 7^h LST on July 11, 1887, is shown in Fig.12 (bottom). Again the rms error is remarkably small. In both cases the indicated speed is v_P - the 3-space speed projected onto the plane of the interferometer. The angle is the azimuth of the 3-space speed projection at the particular LST. Fig. 13 shows speed fluctuations from day to day significantly exceed these errors, and reveal the existence of 3-space flow turbulence - i.e gravitational waves. The data shows considerable fluctuations, from hour to hour, and also day to day, as this is a composite day. The dashed curve shows the non-fluctuating best-fit sidereal effect variation over one day, as the earth rotates, causing the projection onto the plane of the interferometer of the velocity of the average direction of the space flow to change. The predicted projected sidereal speed variation for Mt Wilson is 251 to 415 km/s, using the Casinni flyby data and the STP air refractive index of $n = 1.00026$ appropriate atop Mt. Wilson, and the min/max occur at approximately 5hrs and 17hrs local sidereal time (Right Ascension). For the Michelson-Morley experiment in Cleveland the predicted projected sidereal speed variation is 239 to 465 km/s. Note that the Cassini flyby in August gives a RA= 5.15^h, close to the RA apparent in the above plot. The green data points, showing daily fluctuation bars, at 5^h and 13^h, are from the Michelson-Morley 1887 data, from averaging (excluding only the July 8 data for 7^h because it has poor S/N), and with same rms error analysis. The fiducial time lines are at 5^h and 17^h. The data indicates the presence of turbulence in the 3-space flow, i.e gravitational waves, being first seen in the Michelson-Morley experiment.

13 Conclusions

The Dual RF Coaxial Cable Detecto, exploits the Fresnel drag anomaly in RF coaxial cables, *viz* the drag effect is absent in such cables, for reasons unknown, and this 1st order in v/c detector is compact, robust and uses one clock. This anomaly now explains the operation of the Optical-Fibre - Coaxial Cable Detector, and permits a new calibration. These detectors have confirmed the absolute motion of the solar system and the gravitational wave effects seen in the earlier experiments of Michelson-Morley, Miller, DeWitte and Torr and Kolen. Most significantly these experiments agree with one another, and with the absolute motion velocity vector determined from spacecraft earth-flyby Doppler shifts. The observed significant wave/turbulence effects reveal that the so-called "gravitational waves" are easily detectable in small scale laboratory detectors, and are considerably larger than those predicted by GR. These effects are not detectable in vacuum-mode Michelson terrestrial interferometers, nor by their analogue vacuum-mode resonant cavity experiments.

The new Dual RF Coaxial Cable Detector permits a detailed study and characterisation of the wave effects, and with the detector having the inclination equal to the local latitude the earth rotation effect may be removed, as the detector is

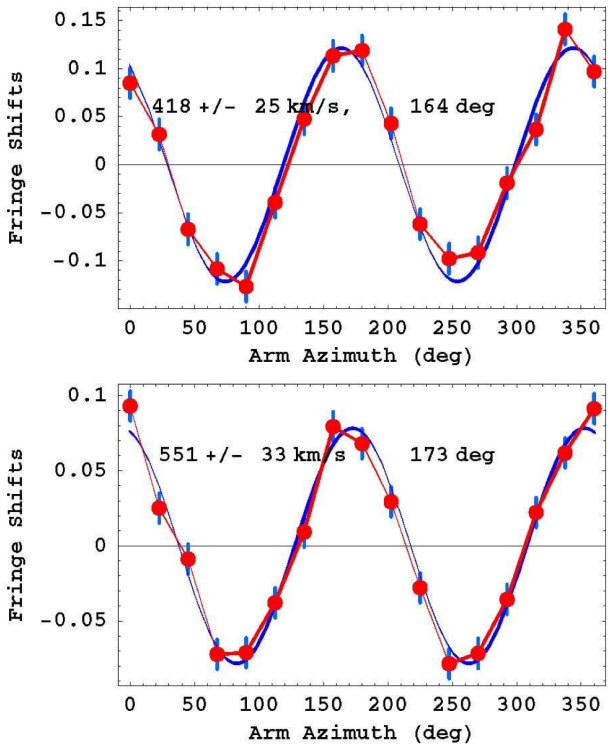

Fig. 12: Top: Typical Miller data from 1925/26 gas-mode Michelson interferometer, from 360° rotation. Bottom: Data from Michelson-Morley 1887 gas-mode interferometer, from 360° rotation.

then parallel to the earth's spin axis, enabling a more accurate characterisation of the wave effects. The major discovery arising from these various results is that 3-space is directly detectable and has a fractal textured structure. This and numerous other effects are consistent with the dynamical theory for this 3-space. We are seeing the emergence of fundamentally new physics, with space being a a non-geometrical dynamical system, and fractal down to the smallest scales describable by a classical velocity field, and below that by quantum foam dynamics [12]. Imperfect and incomplete is the geometrical model of space.

Acknowledgements

The Dual RF Coaxial Cable Detector is part of the Flinders University Gravitational Wave Detector Project. The DSO, Rb RF frequency source and coaxial cables were funded by an Australian Research Council Discovery Grant: *Development and Study of a New Theory of Gravity*. Special thanks to CERN for donating the phase stabilised optical fibre, and to Fiber-Span for donating the optical-electrical converters. Thanks for support to Professor Warren Lawrance, Bill Drury, Professor Igor Bray, Finn Stokes and Dr David Brotherton.

Submitted on April 17, 2012 / Accepted on April 21, 2012

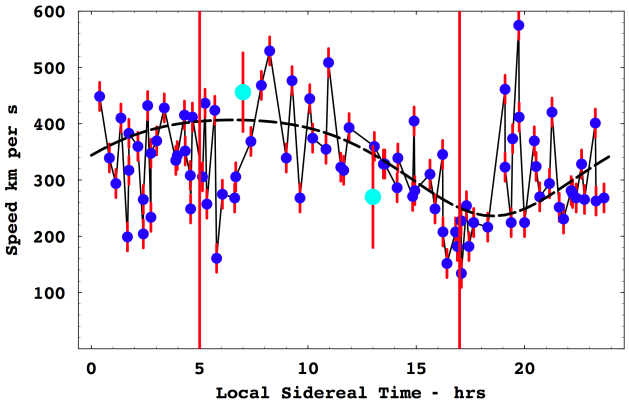

Fig. 13: Miller data for composite day in September 1925, and also showing Michelson-Morley 1887 July data at local sidereal times of 7^h and 13^h. The waved/turbulence effects are very evident, and comparable to data reported herein from the new detector.

References

1. Cahill R.T. A New Light-Speed Anisotropy Experiment: Absolute Motion and Gravitational Waves. *Progress in Physics*, 2006, v. 4, 73–92.
2. Cahill R.T. Absolute Motion and Gravitational Wave Experiment Results. Contribution to *Australian Institute of Physics National Congress*, Brisbane, Paper No. 202, 2006.
3. Cahill R.T. and Kitto K. Michelson-Morley Experiments Revisited. *Apeiron*, 2003, v. 10(2), 104–117.
4. Cahill R.T. The Michelson and Morley 1887 Experiment and the Discovery of Absolute Motion. *Progress in Physics*, 2005, v. 3, 25–29.
5. Miller D.C. The Ether-Drift Experiment and the Determination of the Absolute Motion of the Earth. *Reviews of Modern Physics*, 1933, v. 5, 203–242.
6. Torr D.G. and Kolen P. in: Precision Measurements and Fundamental Constants, Taylor B.N. and Phillips W.D. (eds.) *National Bureau of Standards (U.S.), Spec. Pub.*, 1984, 617–675.
7. Cahill R.T. The Roland De Witte 1991 Experiment. *Progress in Physics*, 2006, v. 3, 60–65.
8. Anderson J.D., Campbell J.K., Ekelund J.E., Ellis J. and Jordan J.F. Anomalous Orbital-Energy Changes Observed during Spacecraft Flybys of Earth. *Physical Review Letters*, 2008, v. 100, 091102.
9. Cahill R.T. Combining NASA/JPL One-Way Optical-fibre Light-Speed Data with Spacecraft Earth-Flyby Doppler-Shift Data to Characterise 3-Space Flow. *Progress in Physics*, 2009, v. 4, 50–64.
10. Cahill R.T. Unravelling Lorentz Covariance and the Spacetime Formalism. *Progress in Physics*, 2008, v. 4, 19–24.
11. Cahill R.T. and Stokes F. Correlated Detection of sub-mHz Gravitational Waves by Two Optical-fibre Interferometers. *Progress in Physics*, 2008, v. 2, 103–110.
12. Cahill R.T. Process Physics: From Information Theory to Quantum Space and Matter. Nova Science Pub., New York, 2005.
13. Cahill R.T. and Brotherton D., Experimental Investigation of the Fresnel Drag Effect in RF Coaxial Cables. *Progress in Physics*, 2011, v. 1, 43–48.

Synchronous Measurements of Alpha-Decay of ^{239}Pu Carried out at North Pole, Antarctic, and in Puschino Confirm that the Shapes of the Respective Histograms Depend on the Diurnal Rotation of the Earth and on the Direction of the Alpha-Particle Beam

S. E. Shnoll[*§¶], M. E. Astashev[*], I. A. Rubinshtein[†], V. A. Kolombet[*], S. N. Shapovalov[‡], B. I. Bokalenko[‡], A. A. Andreeva[*], D. P. Kharakoz[*], I. A. Melnikov[‖]

[*]Institute of Theoretical and Experimental Biophysics, Russ. Acad. Sciences. E-mail: shnoll@mail.ru (Simon E. Shnoll)
[†]Skobeltsyn Institute of Nuclear Physics, Moscow State University. E-mail: iarubinst@mail.ru (Ilia A. Rubinstein)
[‡]Arctic and Antarctic Research Institute
[§]Physics Department, Moscow State University
[¶]Puschino Institute for Natural Sciences
[‖]Shirshov Institute of Oceanology, Russ. Acad. Sciences

Dependence of histogram shapes from Earth diurnal rotation, and from direction of alpha-particles issue at ^{239}Pu radioactive decay is confirmed by simultaneous measurements of fluctuation amplitude spectra — shapes of corresponding histograms. The measurements were made with various methods and in different places: at the North Pole, in Antarctic (Novolazarevskaya station), and in Puschino.

1 Introduction

Fine structure of an amplitude fluctuation spectrum (i.e., that of "data spread") can be determined during measurements of different nature changes with the Earth rotation around its axis and its movement along its orbit.

This follows from the regular changes in the shape of the respective histograms with diurnal and annual periods. Well-defined periods are observed: those of "stellar" (1,436 minutes) and "solar" (1,440 minutes) days, "calendar" (365 average solar days), "tropical" (365 solar days 5 hours 48 minutes) and "sidereal" (365 days 6 hours 9 minutes) years [1].

Experiments with collimators that allow studies of alpha-particle beams with definite directions indicate that this regularity is related to non-uniformity (anisotropy) of space [1, 6].

Dependence on the diurnal Earth rotation shows in high probability of shape similarity of histograms obtained during measurements in different locations at the same local time, as well as in the disappearance of diurnal periods near the North Pole [2]. However, together with synchronous changes in histogram shapes according to the local time, some experiments show changes in histogram changes simultaneously according to an absolute time [2]. It was discovered that synchronism with regard to absolute time (e.g. during measurements in Antarctic and in Puschino, Moscow Region) observed during measurements of alpha-decay of ^{239}Pu, depends on the spatial orientation of the collimators [1, 3, 5].

In order to study dependences of the absolute synchronism phenomenon, experiments carried out near the North Pole, which would minimize effects of the Earth's diurnal rotation, were required,.

The first such attempt was undertaken in 2001 by joint efforts of Inst. Theor. & Experim. Biophysics of Russ. Acad. Sciences (ITEB RAS) and Arctic & Antarctic Res. Inst. (AARI), when twenty-four-hour measurements of ^{239}Pu alpha-decay with a counter without collimator were carried out continuously during several days in a North Pole expedition on the "Akademik Fedorov" research vessel.

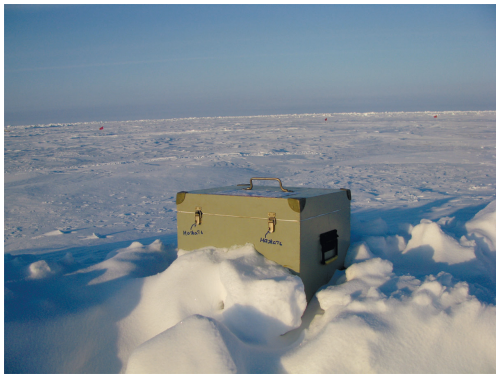

Fig. 1: Measuring device at North Pole.

However, the ship was not able to come closer than latitude 82° North to the North Pole. But even this incomplete approaching to the North pole has shown almost complete disappearance of diurnal changes in the histogram shapes that were observed during the same period of time in Puschino (latitude 54° North) [2].

In 2003, we found out that diurnal changes in histogram shapes also disappear when alpha-radioactivity is measured with collimators that issue alpha-particle beams directed towards the Pole star. This indicated that histogram shapes depend on a space direction of a process[1, 6].

This conclusion was later repeatedly confirmed by experiments with collimators directed westward, eastward, northward, or rotated in the horizontal plane counterclockwise with

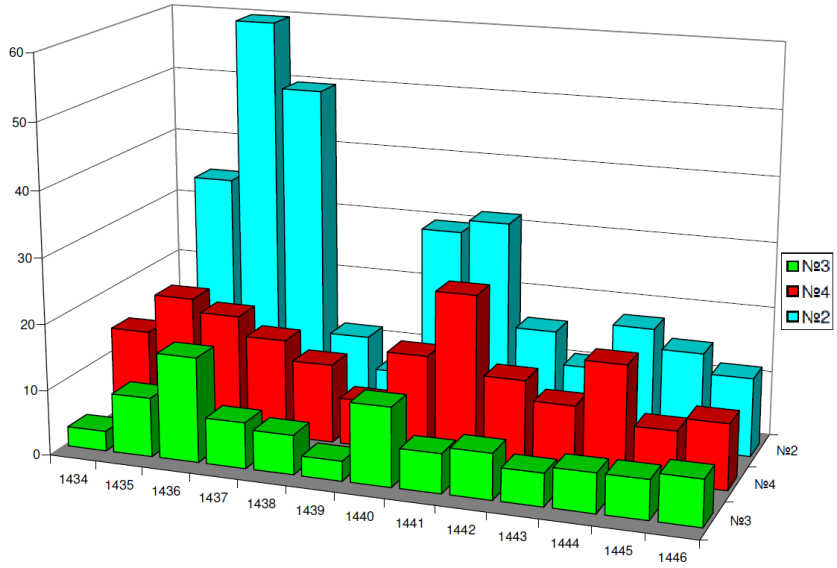

Fig. 2: During the ^{239}Pu alpha-decay measurements at the North Pole, the effect of the daily period disappearance is more pronounced for the vertical detector (device no. 3) than for the horizontal one (device no. 4). For comparison, daily period is shown for synchronous measurements in Puschino with a westward-directed collimator (device no. 2). The abscissa axis shows minutes. The ordinate axis shows the number of the similar pairs obtained during this period with a total number of the compared rows of 360.

periods of 1, 2, 3, 4, 5, 6, 12 hours. The histogram shape changed with the respective periods.

In 2011, we were able to carry out synchronous experiments on ^{239}Pu alpha-decay using nine different devices, two of which were located at the North Pole during the period of work at the Pan-Arctic ice drifting station (latitude 89° 01 — 89° 13 North, longitude 121° 34 —140° 20 East), one in Antarctic (the Novolazarevskaia station, latitude 70° South, longitude 11° East), and six more having different collimators in Puschino (latitude 54° North, longitude 37° East).

As a result of this project, we were able to confirm the conclusion that histogram shapes depend on the diurnal rotation of the Earth, and to show that, when alpha-particle beam is directed along the meridian, the histogram shape changes synchronously from the North Pole to the Antarctic.

2 Materials and methods

The device was installed on the surface of drifting ice near the geographic North Pole (Fig. 1) and worked continuously since April 5, 11 till April 12, 11, until its accumulators were out of charge.

The measurement results obtained at the North Pole since April 5, 11 till April 12, 11 were analyzed in the ITEB RAS in Puschino. The analysis was, as usual, comparison of histogram shapes for measurements made with different devices. A detailed description of the methods of histogram construction and shape comparison can be found in [1].

This paper is based on the results obtained from the simultaneous measurements of alpha-activity of the ^{239}Pu samples with the activity of 100–300 registered decay events per second using 9 different devices with semiconductor alpha-particle detectors constructed by one of the authors (I. A. Rubinshtein) with and without collimators [6] and registration system constructed by M. E. Astashev (see [7]).

The main characteristics of the devices used in this study are given in Table 1.

Because of special complications presented by the conditions at the North Pole (no sources of electricity, significant temperature variations) a special experimental system with autonomous electricity source, thermostat, and time recording was created by M. E. Astashev. This device contained two independent alpha-particle counters (I. A. Rubinshtein), one directed upwards and another one directed sidewards, which were combined with a special recording system.

A system based on the computing module Arduino Nano V.5 [7–1] was used for registering the signals from the alpha-particle counter. The software provided all service functions for impulse registration, formation of the text data for the flash card, obtaining the time data, regulation of the heater, obtaining the temperature and the battery charge data. The data were recorded onto a 1 Gb microSD card, and the function library Fat16.h, real time clock were implemented using the DS1302 chip [7–2] with a lithium battery CR2032 independent power supply [7–3]. Power supply of the registering system and alpha-particle counters was provided by four waterproof unattended geleous lead batteries of 336 W× h total capacity [7–3]. To provide working conditions for the batteries and stability of the system, a 12 W electric heater with pulse-duration control and temperature detector AD22100 was added [7–4]. Pulse counters were implemented by processing external hardware interruptions of the computing module. The data were recorded onto the card as plain text.

Number	Device type	Coordinates	The expected purpose, i.e. registration of the histogram shape changes caused by:
1	Collimator, directed eastward	Puschino, lat. 54° North, long. 37° East	diurnal Earth rotation
2	Collimator, directed westward	Puschino, lat. 54° North, long. 37° East	diurnal Earth rotation
3	Flat detector without collimator, directed "upwards"	North Pole	Earth circumsolar rotation
4	Flat detector without collimator, directed "sidewards"	North Pole	combined, diurnal and circumsolar, Earth rotation
5	Collimator, directed towards the Polar Star	Puschino, lat. 54° North, long. 37° East	circumsolar Earth rotation
6	Polar Star directed collimator-free flat detector	Puschino, lat. 54° North, long. 37° East	combined, diurnal and circumsolar, Earth rotation
7	Sun directed collimator, clockwise rotation	Puschino, lat. 54° North, long. 37° East	circumsolar Earth rotation
8	Collimator-free flat detector, directed "upwards"	Puschino, lat. 54° North, long. 37° East	combined, diurnal and circumsolar, Earth rotation
9	Horizontal collimator, directed northward	Puschino, lat. 54° North, long. 37° East	combined, diurnal and circumsolar, Earth rotation

Table 1: The devices for the measurements of ^{239}Pu alpha-decay used in this study.

3 Results

3.1 Daily periods of the histogram shape changes depend on the detector orientation

Fig. 2 shows that measurement of ^{239}Pu alpha-activity in Puschino with a westward-directed collimator (device no. 2) leads to appearance of similar histograms with two clearly distinguished periods, which are equal to a sidereal day (1,436 min) and a solar day (1,440 min). During measurements at the North Pole with flat detectors, daily periods almost disappear. It can be noticed, however, that daily periods are slightly more pronounced for the flat detector directed sidewards (horizontally; device no. 4). The periods disappear for measurements at the North Pole with a detector directed upwards (vertically; device no 3).

Dependence of the effects observed at the North Pole on the detector orientations, which was revealed while looking for the diurnal periods, indicates that these effects were not caused by any influence by some "geophysic" impacts on the studied processes or on the measurement system. Not location of the device but rather orientation of the detector determines the outcome. A similar result was observed for two other Pole Star-directed detectors in Puschino, one of which was flat and another had a collimator (data not shown). The main effect, disappearance of the daily period, was significantly more pronounce with a collimator-equipped detector.

3.2 The absolute time synchronism of the changes in the histogram shapes, in the ^{239}Pu alpha-activity measurements in Antarctic, at the North Pole and in Puschino depends on the orientation of the detectors

The main role of the spatial orientation rather than geographical localization in the studied phenomena is clearly seen from the high probability of the histogram similarity if they are measured simultaneously at the same absolute time using a vertical detector at the North Pole and a Pole Star-directed detector with a collimator in Puschino (Fig. 3A, B)

Dependence of the synchronism with regard to the absolute time on the spatial orientation of the detectors was particularly clearly revealed during comparison of the histograms constructed on the basis of ^{239}Pu alpha-activity measurements in Antarctic, at the North Pole, and in Puschino.

In Fig. 4 A and B, we can see high probability of absolute synchronism for measurements performed on April 8, 2011 and on April 9, 2011 in Antarctic (no. 8) with a vertical detector located at the North Pole (no. 3), and in Puschino with a collimator directed at the Sun (no. 7). There is no synchronism for experiments with a horizontal detector at the North Pole (no.4) and detector in Antarctic (no. 8).

Therefore, during measurements at the North Pole with a vertical detector, or with collimator-equipped detectors aimed at the Sun or at the Pole Star in Puschino, that is both detectors cannot depend upon Earth diurnal rotation, there was an absolute synchronism of the histogram shape change with histogram shape changes in Antarctic.

Another illustration of the role of detector orientation for the measurements at the North Pole is given in Fig.5. Absolute synchronism of the histogram shape change is more pronounced for comparison of the ^{239}Pu alpha-activity measurements in Puschino with a collimator constantly directed at the Sun and at the North Pole with a vertically-directed collimator.

4 Discussion

The results of the present study confirm that the changes in the histogram shape depend on the diurnal rotation of the

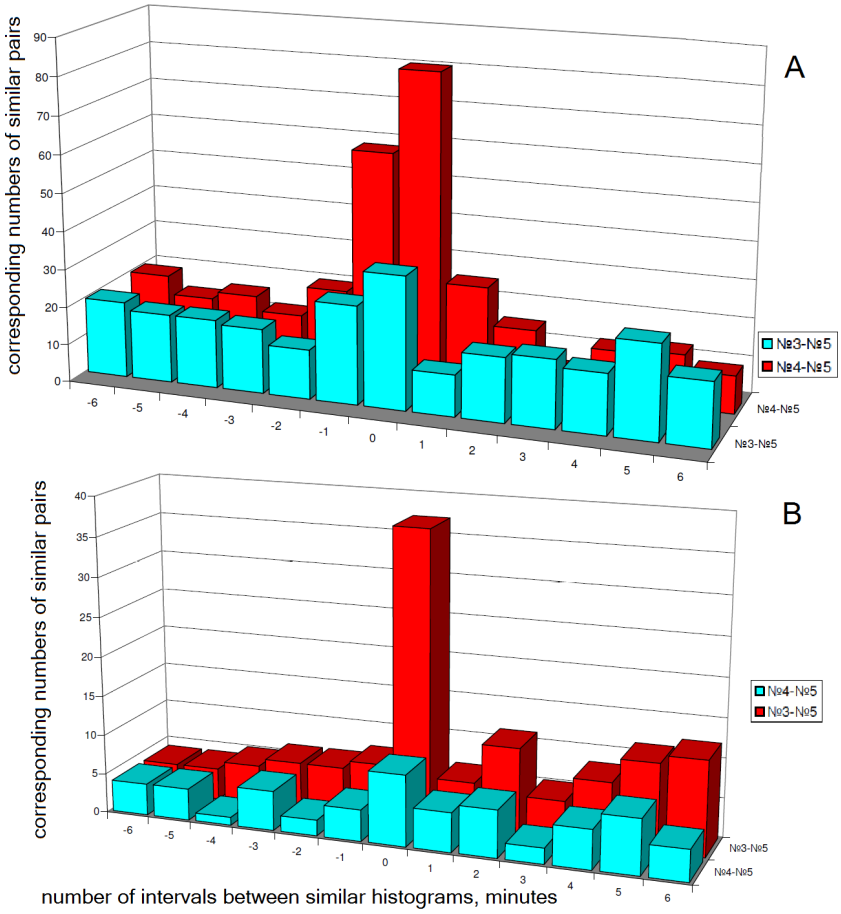

Fig. 3: Two experiments were performed on April 8, 2011(A) and April 9, 2011(B). High probability of the histogram shape similarity at the same absolute time is observed for measurements in Puschino using Pole Star-directed detector with a collimator (device no. 5) and at the North Pole with a vertical detector (device no. 3). There is no similarity during similar measurements in Puschino (the same device no. 5) and at the North Pole with a horizontal detector (device no. 4). X-axis is numbers of intervals between similar histograms, min.; Y-axis is correspondent numbers of similar pairs.

Earth and that this dependence is caused by anisotropy of our space. Daily periods of the changes in the histogram shapes are not observed when alpha-particle beams are parallel to the Earth axis.

Absolute synchronism of the changes in the histogram shapes is observed in experiments with collimators directed at the Pole Star and at the Sun in Puschino (latitude 54° North) (no. 5). and for measurements at the North Pole (latitude 90° North) with a "vertical" detector only (no. 3). There is no absolute synchronism with the "horizontal" counter (no. 4). By analogy, absolute synchronism of the changes in the histogram shapes for measurements in Antarctic is observed only for measurements at the North Pole with a "vertical" detector and a Sun-directed detector in Puschino.

Comparison of these data with the "local time effect", i.e. synchronous changes in the histogram shape in different geographical locations at the same local time, allows to suggest that changes in the histogram shapes, which are synchronous in different geographical locations with regard to the absolute time, are caused by the movement of the laboratory with the Earth along the solar orbit, and synchronism with regard to the absolute time is caused by Earth rotations. This conclusion should be a subject of additional studies.

Acknowledgements

This work was made possible through the financial support from the founder of the "Dynasty Foundation", Professor D. B. Zimin. We are grateful to M. N. Kondrashova for important discussions, interest and friendly support. We also gratefully acknowledge important discussions of the research plans and of the obtained results with D. Rabounski. We are grateful to M. A. Panteleev for his helpful advice and English version of the article.

We thank A. G. Malenkov, E. I. Boukalov, and A. B. Tsetlin for their helpful advice on the organization of the studies at the North Pole.

Submitted on March 11, 2012 / Accepted on March 16, 2012

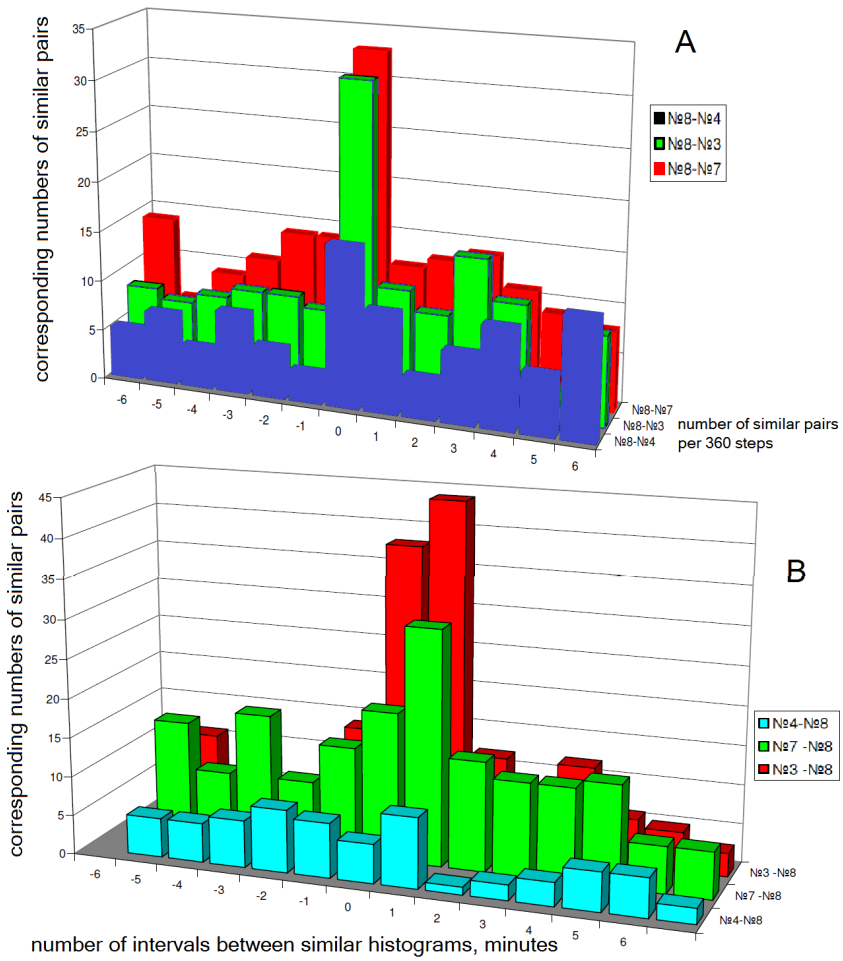

Fig. 4: The experiments, A and B. The shapes of the histograms change synchronously with regard to the absolute time during measurements of the ^{239}Pu alpha-activity in Antarctic and at the North Pole with a vertical detector (no. 8 — no. 3) and in Puschino with a collimator directed at the Sun (no. 8 — no. 7). During measurements at the North Pole with a horisontally-directed collimator, there is no synchronism with Antarctic (no. 8 — no. 4).

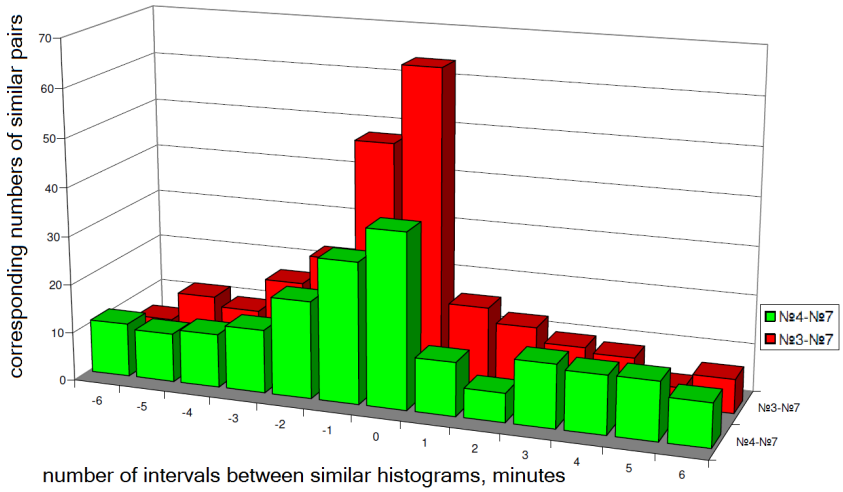

Fig. 5: Absolute synchronism of the changes in the historgram shapes for measurements of ^{239}Pu alpha-activity in Puschino with a collimator directed at the Sun (no. 7) and measurements at the North Pole with a vertical (no. 3) and a horizontal (no. 4) detectors. Absolute synchronism is more pronounced for measurements with a vertical detector.

References

1. Shnoll S. E. Cosmic Physical Factors in Random Processes. Svenska Fisikarkivet, Stockholm, 2009, (*in Russian*)
2. Shnoll S. E., Rubinshtein I. A., Zenchenko K. I., Zenchenko T. A., Udal'tsova N. V., Kondradov A. A., Shapovalov S. N., Makarevich A. V., Gorshkov E. S., Troshichev O. A. Dependence of "macroscopic fluctuations" on geographic coordinates (from materials of Arctic (2000) and Antarctic (2001) expeditions). *Biofizika*, 2003 Nov–Dec, v. 48 (6), 1123–1131 (*in Russian*).
3. Shnoll S. E., Zenchenko K. I., Berulis I. I., Udal'tsova N. V., Zhirkov S. S., Rubinshtein I. A. Dependence of "macroscopic fluctuations" from cosmophysical factors. Spatial anisotropy. *Biofizika*, 2004 Jan–Feb, v. 49 (1), 132–139 (*in Russian*).
4. Shnoll S. E., Rubinshtein I. A., Zenchenko K. I., Shlektarev V. A., Kaminsky A. V., Konradov A. A., Udaltsova N. V. Experiments with rotating collimators cutting out pencil of alpha-particles at radioactive decay of Pu-239 evidence sharp anisotropy of space. *Progress in Physics*, 2005, v. 1 81–84.
5. Shnoll S. E. Changes in fine structure of stochastic distributions as a consequence of space-time fluctuations. *Progress in Physics*, 2006, v. 2 39–45.
6. Shnoll S. E. and Rubinstein I. A.. Changes in fine structure of stochastic distributions as a consequence of space-time fluctuations. *Progress in Physics*, 2009, v. 2 83–95.
7. http://arduino.cc/en/Main/ArduinoBoardNano;
   http://www.henningkarlsen.com/electronics/a_l_ds1302.php;
   http://arduino.cc/forum/index.php/topic,8268.0.html;
   http://www.delta-batt.com/upload/iblock/19e/delta%20hr12-7.2.pdf;
   http://www.analog.com/en/mems-sensors/analog-temperature-sensors/ad22100/products/product.html

Dependence of Changes of Histogram Shapes from Time and Space Direction is the Same when Fluctuation Intensities of Both Light-Diode Light Flow and ^{239}Pu Alpha-Activity are Measured

I. A. Rubinshtein*, S. E. Shnoll†§¶, A. V. Kaminsky‖, V. A. Kolombet†, M. E. Astashev†, S. N. Shapovalov‡, B. I. Bokalenko‡, A. A. Andreeva†, D. P. Kharakoz†

*Skobeltsyn Institute of Nuclear Physics, Moscow State University
E-mail: iarubinst@mail.ru
†Institute of Theoretical and Experimental Biophysics, Russ. Acad. Sciences
E-mail: shnoll@mail.ru
‡Arctic and Antarctic Research Institute
§Physics Faculty, Moscow State University
¶Puschino Institute for Natural Sciences
‖Elfi-tech Ltd., Rekhovot, Israel

The paper tells that spectra of fluctuation amplitudes, that is, shapes of corresponding histograms, resulting measurements of intensity of light fluxes issued by a light-diode and measurements of intensity of ^{239}Pu alpha-particles issues change synchronously. Experiments with light beams show the same diurnal periodicity and space direction dependencies as experiments with radioactivity. Thus new possibilities for investigation of "macroscopic fluctuations" come.

1 Introduction

Previous papers [1] have shown that shapes of fluctuation amplitudes spectra, i.e. shapes of corresponding histograms, constructed by results of measurements of various nature processes — from electronic device noises, rates of chemical and biochemical reactions, and Brownian movement to radioactive decay of various types — are determined by cosmophysical factors: diurnal and circumsolar rotations of the Earth. A histogram shape depends on geographical coordinates and space direction. Shapes of histograms of different nature processes taking place in different geographical locations but at the same local times are the same.

A histogram shape depends on a direction which alpha-particles issued at radioactive decay follow; this was shown in measurements of ^{239}Pu alpha-radioactivity fluctuations. Study of dependence between fluctuations and angle orientation of their source benefits a lot from focusing a source. When diameter of net collimator holes decreases, registered activity of particles flow falls crucially, preventing statistical reliability of results. This adverse effect complicates construction and use of a focused collimator-equipped ^{239}Pu source. For that matter, we have examined similar time and space direction dependencies at measurements of fluctuations of light beams intensity. Regularities of histogram shape changes at measurements of light flux intensity fluctuations were shown to be absolutely the same as those at measurements of radioactive alpha-decay. Use of this fact makes it possible to increase substantially accuracy of spatial resolution at increase of a light beam and to set out a lot of other experiment versions.

2 Devices and methods

2.1 Measurements of variously directed light flows. Sources and detectors of light flows

We measured fluctuations of intensity of light beams provided by a light diode and measured with a photo diode. Values to register were numbers of events, i.e. exceedings of a set threshold of light intensity per a time unit.

AL 307D light diode with ~630 nm wave length and 8 mA direct current was used as source of light. A224 photo diode by FGUP "PULSAR" Federal State Unitary Enterprise was used as a detector. Light and photo diodes were fastened in a tube with light channel; diameter of the tube was 3 mm, and space between diodes was 35 mm (Fig. 1).

The collimator with light and photodiodes can be oriented in a desired direction. Alternate component of the photo diode current comes through the low-noise amplifier to the input of the comparator registering signals that exceed a preset threshold value. The value should provide 200-500 exceeding

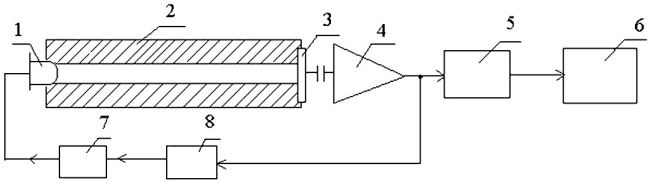

Fig. 1: Functional diagram of device measuring light beam fluctuations 1 — light diode 2 — collimator 3 — photo diode 4 — low-noise amplifier 5 — comparator 6 — impulse counter 7 — stabilizer of mean-square voltage value at amplifier (4) output 8 — light diode current generator

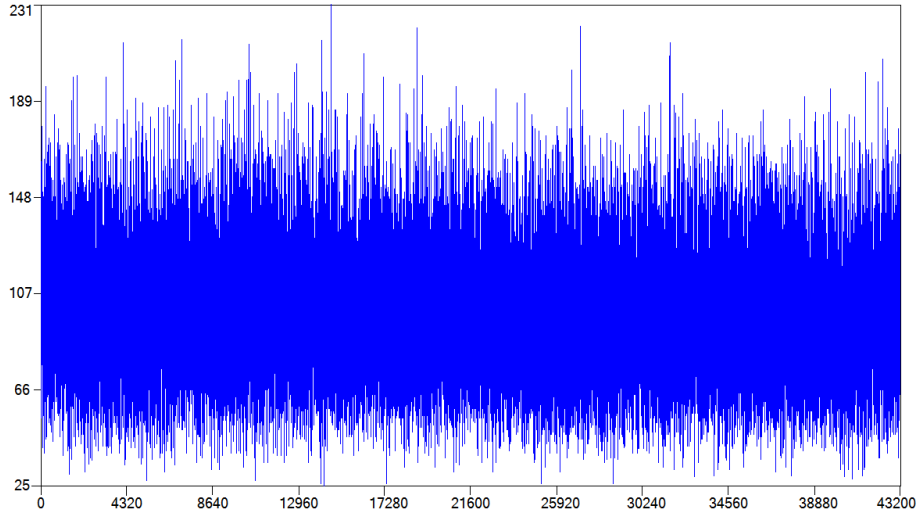

Fig. 2: Illustration of a time series image at measurements of fluctuations of light flow intensity. X-axis is time in seconds. Y-axis is numbers of light flow fluctuations with heights exceeding the device noise.

signals per a second. Besides counting impulses, the device can examine fluctuations of distribution of an amplifier signal heights by digitizing signals with a preset frequency, for example, 300 Hz. Nature of amplifier signal height distribution is electric noise. Its fluctuations can be examined by AD of noise signal followed with histograming of equal time periods.

Impacts of photons falling to photodiode were determined with measurements of mean-square values of amplifier signals, the amplifier being connected to source of current equal to photo diode CD without lighting (1.4 mcA). It equals to 5.6 mV, whereas mean-square value of signals at photons falling is 36 mV. If an electronic device noise consists of two components, its value can be determined by the following expression:

$$U_n = \sqrt{U_{n_1}^2 + U_{n_2}^2} \, .$$

In our case: U_{n_1} is photon noise signal, U_{n_2} is noise signal of current equal to photo diode one, and U_n is total noise signal. From here: U_{n_1} = 32.2 mV, that is ≅6 folds higher than current noise.

2.2 Results of measurements of numbers of discriminator threshold exceedings per a second

They were saved in a computer archive. Histograms were constructed, usually, by 60 results of measurements during one minute total time.

2.3 Computing histograms and analysis of their shapes

They have been multiply described earlier [1]. Shapes of histograms were compared by Edwin Pozharsky auxiliary computer program requiring further expert-made "similar-nonsimilar" diagnosis and by completely automated computer program by Vadim Gruzdev [2].

3 Results

Most of measurements were made at the Institute of Theoretical and Experimental Biophysics of Russian Academy of Sciences (ITEB RAS) in Puschino and in AARI Novolazarevskaya station in Antarctic. In Puschino we used a device with three light beam collimators directed towards West, East, and Polar Star and devices with alpha-activity measuring collimators directed the same towards West, East, and Polar Star. In Novolazarevskaya station we measured alpha-activity with

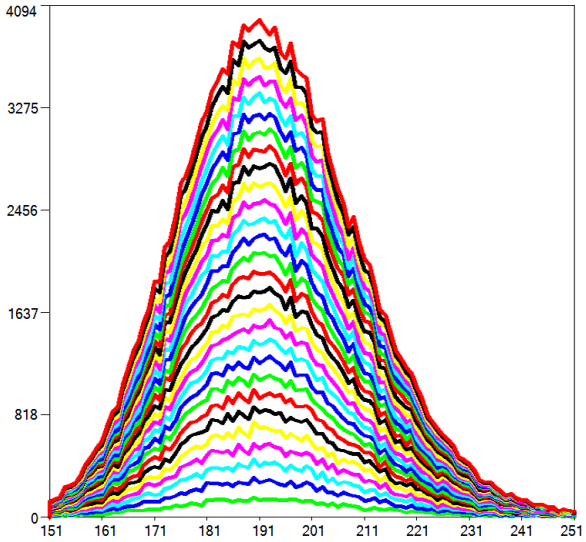

Fig. 3: Change of shapes of non-smoothed summed distributions according to stepwise increase of amount of light flow intensity measurements. 172,800 one-second measurements during two days: May 4 and 5, 2011. The collimator is East-directed. Layer lines mark each 6,000 measurements. X-axis is intensity (amounts of events per a second); Y-axis is amounts of measurements corresponding to the fluctuations intensity.

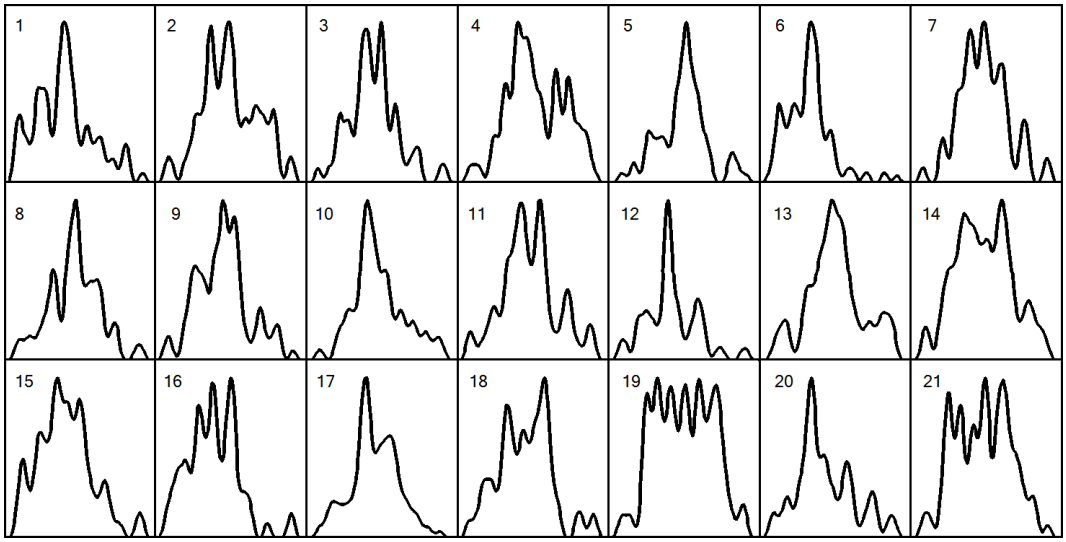

Fig. 4: Fragment of a computer log. Histograms constructed by sixty results of one-second measurements of East-directed light flow fluctuations on May 4, 2011. The histograms are seven times smoothed.

a collimator-free device.

Fig. 2 presents a section of a time series — results of registration of fluctuations of light flows from a West-directed beam. This is a typical stochastic process — white noise.

At this figure a regular fine structure, the same as in investigation of any other process, can be seen. The structure, different in different time periods, does not disappear but becomes more distinct when amount of measurements increase. The nature of this fine structure should become a subject of some special investigations (see in [1]).

The main material of this work is shape of sample distributions, histograms constructed by small (30–60) amount of measurements. The general shape of such histograms was at examination of light flux fluctuations the same as at examination of radioactivity and other processes. This can be seen from Fig. 4.

Similarity of shapes of histograms resulting measurements during other processes is conditioned by a reason shared by all of them. This follows from high probability of histogram shapes similarity at synchronous independent measurements of processes with different nature.

3.1 High probability of similarity of histograms computed by results of simultaneous measurements of light and alpha-decay intensities

Fig. 5 shows high probability of histograms similarity at synchronous measurements of light and alpha-decay intensities.

Comparing series of 360 (1) and 720 (2) histogram pairs we found that shapes of histograms resulting two different processes are high probably similar; this is shown at Fig. 6. Considering the “mirrorness” effect, that is coincidence of shapes of histograms that become similar after mirror overlapping (line 3 at Fig. 5), one can see the same similarity. This

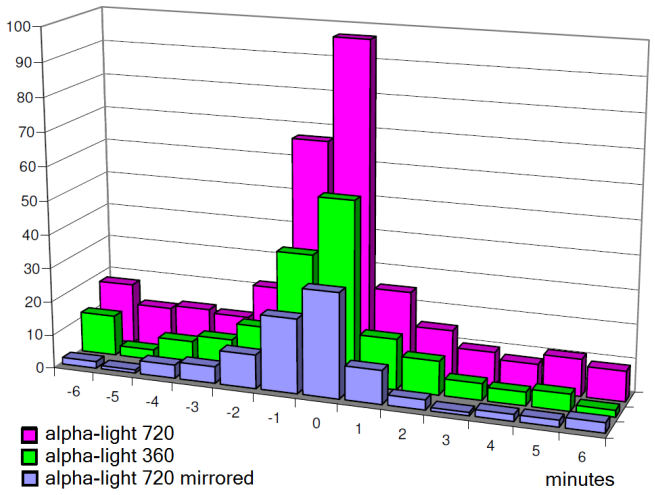

Fig. 5: High probable similarities of shapes of histograms constructed by sixty results of synchronous measurements of alpha-decay fluctuations, and light-beam intensity fluctuations. The measurements were made at West-directions of both 239Pu alpha-particles and light beams. X-axis is values of interval (minutes) between similar histograms. Y-axis is numbers of similar pairs of histograms corresponding to the values. Measurements dated April 4–5, 2011.

and similar experiments confirm the conclusion on the independence of a histogram shape from nature of a process under examination (^{239}Pu alpha-decay and flow of photons from a light diode).

Fig. 6 presents pairs of histograms, comprising the peak corresponding to the maximal probability of histograms similarity at measurements of light and alpha-activity. Shapes of all kinds can be found here. No shapes typical just for synchronism phenomenon are available.

Fig. 7 presents a larger scale of a Fig. 6 part to illustrate

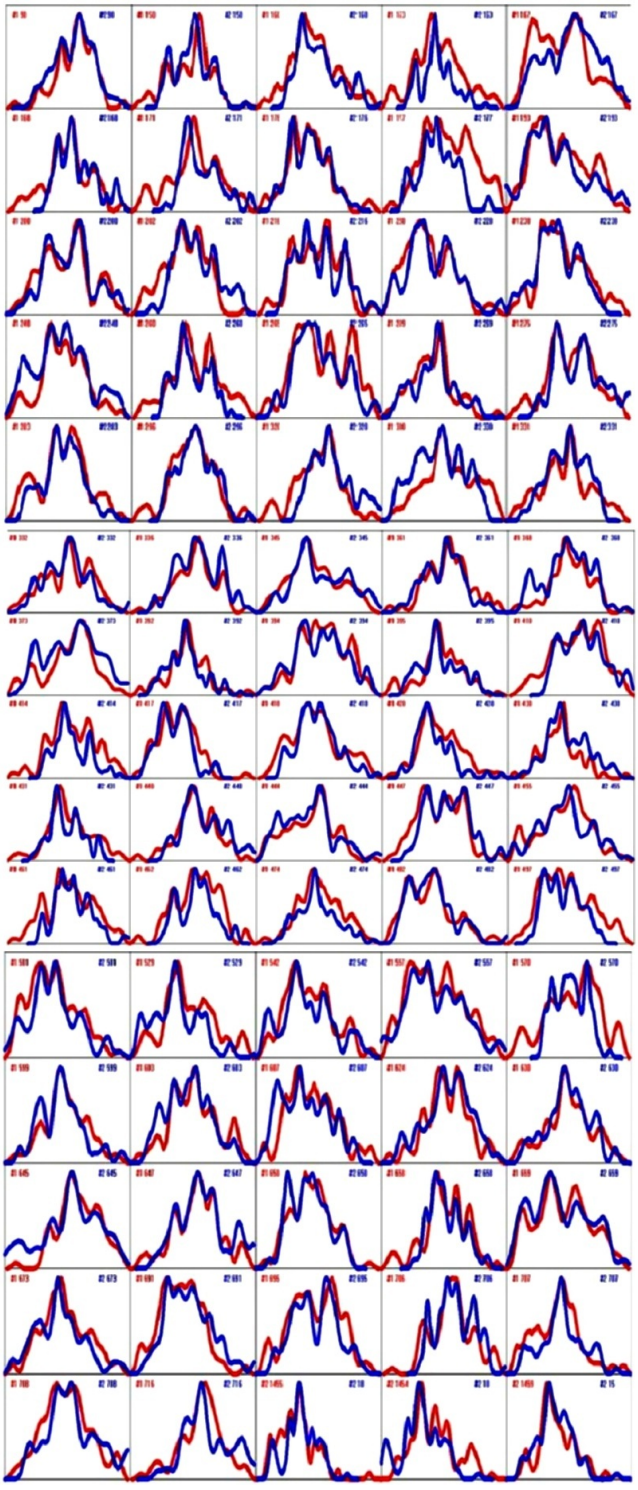

Fig. 6: Fragment of a computer log. Pairs of synchronous histograms from the central peak of Fig. 4. Indicated are numbers of histograms in series.

more visually similarity of shapes of histograms constructed by results of synchronous measurements of α-radioactivity and light intensity fluctuations.

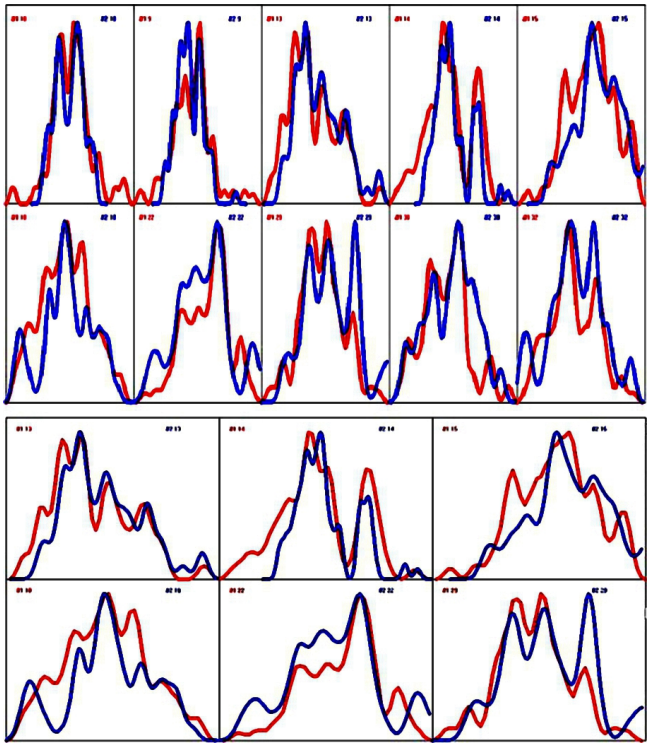

Fig. 7: Enlarged part of Fig. 6.

3.2 Near-a-day periods of similar shape histograms realization at measurements of light intensity fluctuations and their dependence from space direction of a light beam

Fig. 9 presents dependence between a period of similar histograms occurrence and a light beam direction. One can see that star and Sun periods appear equally both at West and East directions of a beam, and disappear completely when a beam is directed towards the Polar Star.

Therefore, changes of histogram shapes at measurements of light flow fluctuation are again related with axial rotation of the Earth. Distinct separation of near-a-day periods into "star" and "Sun" ones, the same as in other cases, means high degree of space anisotropy of observed effects. Difference between star and Sun days is only four minutes, corresponding to 1° in angular measure. These near-a-day periods from Fig. 10 are solved with approximately 20 angular minutes accuracy. Discrimination power of our method may, probably be determined by a collimator aperture, that is narrowness of a light beam.

The absolute lack of near-a-day periods when a light beam is directed towards the Polar Star is the same rather corresponds to ideas on relation of histogram shapes with diurnal Earth rotation. Moreover, the phenomenon means, as was earlier mentioned, that a histogram shape is provided not by some "effects" on a process under examination but only by space anisotropy.

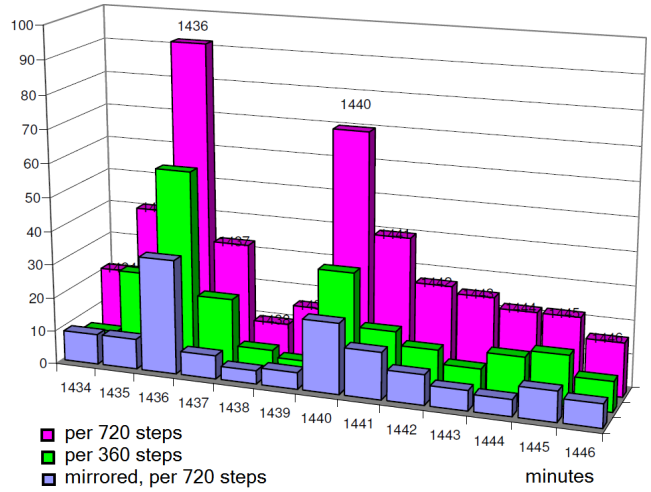

Fig. 8: Shapes of histograms resulting measurements of light intensity, the same as measurements of other nature processes, change with distinct day periods: star (1,436 minutes) and Sun (1,440 minutes) ones. A light beam is directed towards the West. Measurements were made on May 4–5, 2011. Distributions at comparison of lines from 1) 360, 2) 720, and 3) mirror similar pairs only at 760 histograms per a line. X-axis is periods (minutes); Y-axis is numbers of similar pairs after the correspondent time interval.

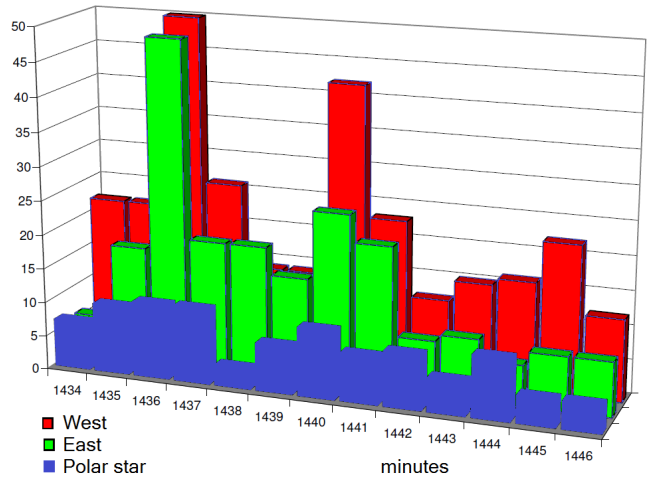

Fig. 9: It can be seen that when a light beam is directed towards the Polar Star no day period presents, and when it is West- or East-directed day periods ("star days" — 1,436 minutes and "Sun Days" — 1,440 minutes) are expressed very distinctly. X-axis is periods (minutes); Y-axis is numbers of similar histogram pairs correspondent to the period value.

3.3 Palindrome effect

A palindrome effect has been presented in [3, 4] when changes of histograms in different days periods were examined. The effect is that succession of histogram shapes since 6 am till 6 pm of accurate local time is like a reverse (inverse) histograms succession since 6 pm till 6 am of a following day. The effect was explained as follows: these are the moments when Earth axial rotation changes its sign relatively its circumsolar rotation: since 6 am till 6 pm ("the day time") these rotations have opposite directions, and 6 pm till 6 am they are co-directed. This implies that a histogram shape is determined by a direction of laboratory rotation corresponding to that of Earth at its diurnal rotation.

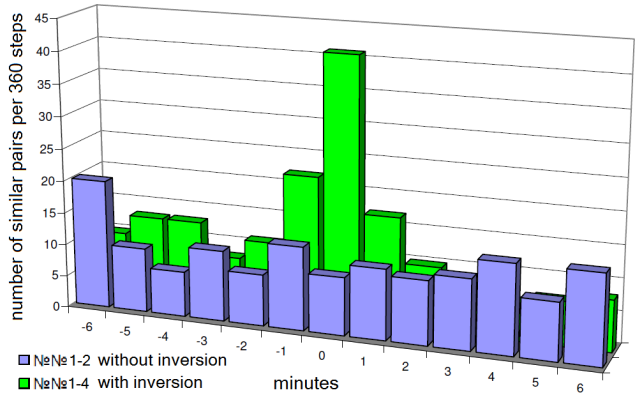

Fig. 10: A palindrome effect in an experiment with light beams. Presence of high similarity of synchronous one-minute histograms at comparison of "daytime" ones with those "nighttime" with inversion of one series and absence of the similarity without inversion. The measurements were made on March 27–28, 2011.

As can be seen from Fig. 10, at examination of histogram shapes in experiments with light beams rather distinct palindrome effect can be seen. When 6 am to 6 pm series of histograms ("day-time histograms") are compared with direct succession of "night-time" histograms their similarity is low probable (a number of similar pairs is little). And when daytime histograms are compared with inverse histogram series probability of synchronous histograms similarity is high.

The palindrome effect seems quite convincing evidence for dependence of a histogram shape from space direction. For this matter, we repeatedly tested its reproducibility at comparison of one-minute histograms with our routine expert method using GM and with just developed by V. A. Gruzdev HC computer program. With the HC program, the palindrome effect was obtained at comparison of ten-minute histograms. 72 "daytime" ten-minute histograms were compared with 72 histograms of direct and inverse series of "nighttime" histograms on "all with all" basis. As one can see from Fig. 11, application of completely automated comparison of histogram shapes with the help of HC program finds the same highly distinct palindrome effect.

3.4 When a light beam is West- or East-directed, similar western histograms are realized 720 minutes later than eastern ones

One of the evidences for relation of a histogram shape with diurnal Earth rotation was results of experiments with alpha-activity measurements with West- and East-directed collimators [5]. No *synchronous* similarity of the histograms could be found in the experiments. When two series — western and eastern ones — are compared, similar histograms occur in

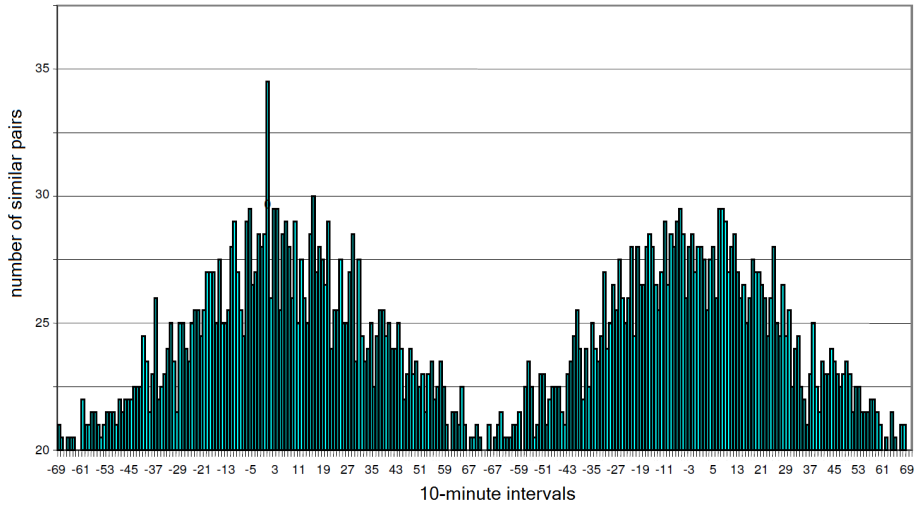

Fig. 11: The palindrome effect in experiments with light. A beam is directed towards West at comparison of ten-minutes histograms with the help of HC computer program. Left: distribution of number of similar histogram pairs at comparison of "daytime" (since 6 am till 6 pm March 27, 2011) histogram series with inverse "nighttime" (since 6 pm March 27 till 6 am March 28, 2011) histogram series; right: the same at comparison of inversion-free series.

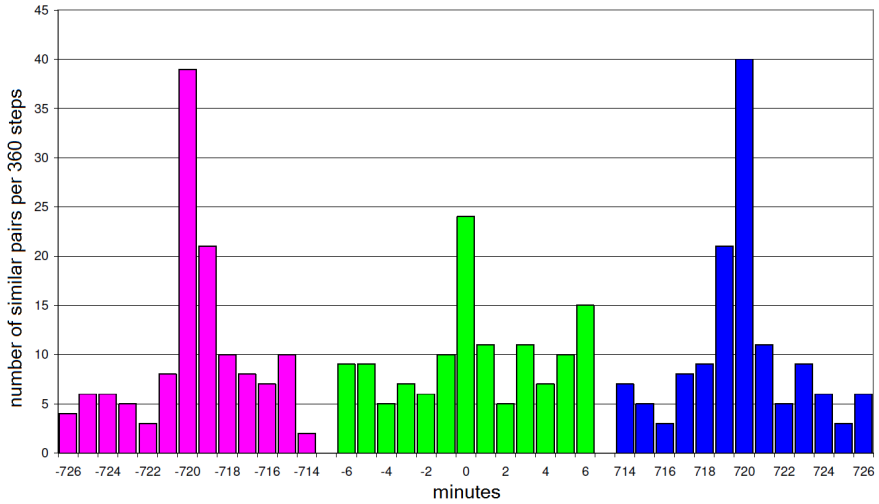

Fig. 12: When a light beam is West- or East-directed, probability of synchronous occurrence of similar histograms is low (intervals are near zero) and that with 720 minutes is high. Measurements from May 4–5, 2011.

720 minutes, that is, in half a day. More detailed investigation allowed us to find a "time arrow" [6]: histograms registered at measurements with eastern collimator were more similar with western in 720 minutes of the following day. In experiments with West- and East-directed light beams, occurrence of similar histograms in 720 minutes and absence of similarity at simultaneous (synchronous) measurements was observed the same rather distinctly. This is illustrated by Figs. 11 and 12.

3.5 Histograms obtained when a light beam is directed towards the Polar Star in Puschino are high probably similar by absolute time with those obtained at measurements of alpha-activity in Antarctic

We observed the same phenomenon earlier at synchronous measurements of alpha-activity in Puschino and in Novolazarevskaya (Antarctic). Histograms resulting measurements of ^{239}Pu alpha-activity in Puschino with a Polar Star directed collimator or with a Sun-directed collimator were high probably similar at one the same time with histograms resulting alpha-activity measurements in Novolazarevskaya with a collimator-free counter. When collimators were West and East directed no synchronism by absolute time between Puschino and Novolazarevskaya was noticed. Expression of synchronism by absolute and local times and its dependence from a space direction are extremely significant phenomena. Appropriate studies we began long ago [7] and continued them in the previous work at simultaneous measurements of alpha-activity in Puschino, Antarctic, and North Pole [8]. In this study we just got added evidence that light beam fluctuations along with alpha-activity measurements could be a quite ap-

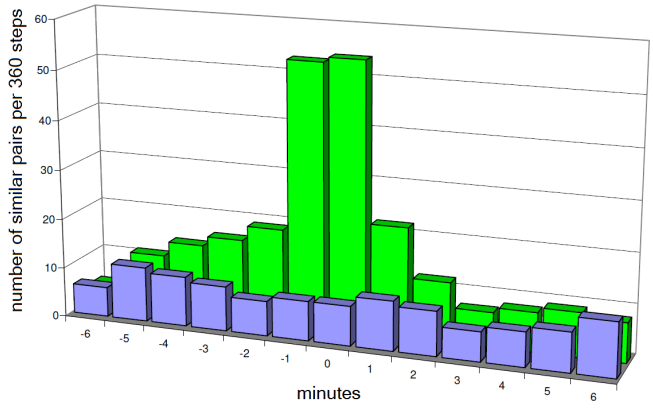

Fig. 13: At 720 minutes shift of eastern histograms measured since 6 am till 6 pm of exact local time to western histograms 6 pm — 6 am of the following day high probable similarity is observed. Without the shift eastern and western histograms are not similar.

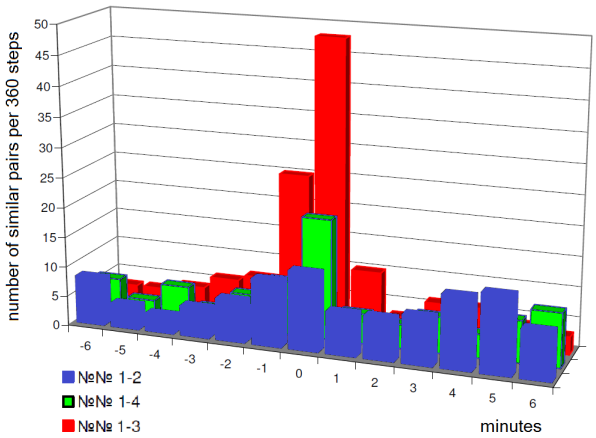

Fig. 14: Time-dependence of numbers of similar pairs of histograms resulting measurements of light beam fluctuations in Puschino and of alpha-activity in Novolazarevskay (1) when a light beam is directed towards Polar Star (3), West (2), and East (4). The origin of X-axis is the moment of absolute time synchronism. Measurements done in May 6, 2011.

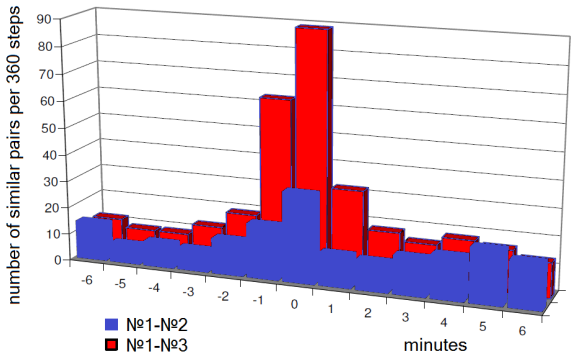

Fig. 15: High probability of absolute time synchronous changes of similarity of shapes of histograms resulting measurements of fluctuations of Polar Star directed light beam in Puschino and fluctuations of alpha-decay in Antarctic. No synchronous similarity can be seen when a light beam is West or East directed. Measurements from May 6, 2011.

propriate object for similar studies. This can be seen from the results of the experiment presented at Figs. 14 and 15.

In this experiment we compared histograms resulting measurements of intensity fluctuations of three light beams: 1) Polar Star, 2) West, and 3) East directed, made in Puschino, with those resulting measurements of alpha-activity with a collimator-free counter, made in Novolazarevskaya. From Figs. 13 and 14 it can be seen that when a light beam is directed highly probable absolute time synchronism of histogram shapes changes in Puschino and in Novolazarevskaya is observed. No synchronism is observed when light beams are West and East directed. The result obtained earlier with collimators and alpha-activity is repeated.

More detailed examinations of these phenomena should become an object for special study.

4 Discussion

Evidence of identical regularities observed at comparison of histogram shapes — spectra of fluctuation amplitudes — of alpha-decay and light diode generated light flow intensities, proves previous conclusion on universality of the phenomenon under examination [1, 9]. This result is not more surprising than identity of regularities at measurements of Brownian movement and radioactivity; or radioactivity and noises in semiconductor schemes [10, 11]. The most significant is an arising possibility to make, with the help of the developed method, more accurate and various examinations of dependence between observed effects and space directions.

As the paper shows, at use of a Polar Star directed light beam absolute (not local) time synchronism in different geographical points — Puschino (54° NL) and Novolazarevskaya (Antarctic, 70° SL) is the same observed. It means that at measurements in such directions factors determining shapes of histograms are expressed, being the same all over the Earth. These regularities, seeming us rather significant, along with others obtained earlier should make body of some special publication.

In conclusion, it should be once more mentioned that to our opinion experiments with light — near-a-day periods, palindrome effects, dependence from a beam direction — also cannot be explained with somewhat universal “effects”. Some “external power” equally affecting alpha-activity, Brownian movement, and fluctuations of photons flow seems unbelievable. The same as earlier, we suppose unevenness and anisotropy of different areas of space-time continuum where examined processes (“laboratories”) get in the result of Earth movement at its diurnal and circumsolar rotations, to be the only general factor determining shapes of histograms of so different processes [1].

Acknowledgements

This study was possible due to the financial support and interest to this line of investigations of the founder of "Dynasty Foundation", Professor D. B. Zimin.

S. E. Shnoll was supported by persistent interest and understanding of M. N. Kondrashova.

We thank V. A. Schlektarev for vivid interest to the study and manufacture of important devices. We are thankful to Olga Seraya for translation of the manuscript.

The continuous support and discussion on the essence of the work with D. Rabounski is of a great importance for S. E. Shnoll.

We are grateful to the colleagues for the discussion, at all stages of the study, at the laboratory seminar. We also thank V. A. Gruzdev for discussion and Fig. 11.

Submitted on March 11, 2012 / March 16, 2012

References

1. Shnoll S. E. Cosmic Physical Factors in Random Processes. Svenska Fisikarkivet, Stockholm, 2009, (*in Russian*)
2. Gruzdev V. A. Algorithmization of histogram comparing process. Calculation of correlations after deduction of normal distribution curves. *Progress in Physics*, 2012, v. 3, 25–28 (this issue).
3. Shnoll S. E., Panchelyuga V. A. and Shnoll A. E. The Palindrome Effect. *Progress in Physics*, 2009, v. 1 3–7.
4. Shnoll S. E. The "Scattering of the Results of Measurements" of Processes of Diverse Nature is Determined by the Earth's Motion in the Inhomogeneous Space-Time Continuum. The Effect of "Half-Year Palindromes". *Progress in Physics*, 2012, v. 1, 3–7.
5. Shnoll S. E., and Rubinstein I. A. Regular Changes in the Fine Structure of Histograms Revealed in the Experiments with Collimators which Isolate Beams of Alpha-Particles Flying at Certain Directions. *Progress in Physics*, 2009, v. 2, 83–95.
6. Shnoll S. E., Rubinstein I. A. and Vedenkin N. N. The "arrow of time" in the experiments in which alpha-activity was measured using collimators directed East and West. *Progress in Physics*, 2010, v. 1, 26–29.
7. Shnoll S. E., Rubinstein I. A., Zenchenko K. I., Zenchenko T. A., Udaltsova N. V., Konradov A. A., Shapovalov S. N., Makarevich A. V., Gorshkov E. S., and Troshichev O. A. Relationship between macroscopic fluctuations and geographical coordinates as inferred from the Data of the 2000 Arctic and 2001 Antarctic expeditions. *Biophysics*, 2003, v. 48 (6), 1039–1047.
8. Shnoll S. E., Astashev M. A., Rubinshtein I. A., Kolombet V. A., Shapovalov S. N., Bokalenko B. I., Andreeva A. A., Kharakoz D. P., and Melnikov I. A. Synchronous measurements of alpha-decay of ^{239}Pu carried out at North Pole, Antarctic, and in Puschino confirm that the shapes of the respective histograms depend on the diurnal rotation of the Earth and on the direction of the alpha-particle beam. *Progress in Physics*, 2012, v. 3, 11–16 (this issue).
9. Shnoll S. E., and Kaminsky A. V. Cosmophysical factors in the fluctuation amplitude spectrum of Brownian motion. *Progress in Physics*, 2010, v. 3, 25–30.
10. Shnoll S. E. and Kaminsky A. V. The study of synchronous (by local time) changes of the statistical properties of thermal noise and alpha-activity fluctuations of a ^{239}Pu sample. arXiv: physics/0605056.

Algorithmization of Histogram Comparing Process. Calculation of Correlations after Deduction of Normal Distribution Curves

Vadim A. Gruzdev
Russian New University
E-mail: 2801218@gmail.com

A newly established computer program for histogram comparing can reproduce main features of the "macroscopic fluctuations" phenomenon: diurnal and yearly periodicity of histogram shapes changing; synchronism of their changing by local and absolute times and "palindrome" phenomenon. The process is comparing of histogram shapes by correlation coefficients and figure areas resulting reducing of picked normal curves from histograms.

1 Introduction

Discovery of macroscopic fluctuations in stochastic processes provided actuality of a computer able to compare shapes of histograms releasing an expert from this labor [1]. Fuzziness of examined shapes and difficulties in their grouping, that is, forming of similar shapes "clusters" made a computer comparison of histogram shapes a rather hard task [1].

Our paper presents a brief of Histogram Comparer (HC), a computer program replacing an expert essentially. Calculation of correlation coefficients of curves resulting deduction of an appropriate normal distribution from a smoothed histogram is taken as a basis for the algorithm. To compare such curves, the same as with expert comparison, maximal correlation coefficients are obtained after the correlations are shifted relatively each other and mirrored, if necessary. The idea of such a transformation of histograms has been used in N. V. Udaltsova's PhD theses [2].

Main effects revealed at visual expert comparison could be reproduced with the help of the HC program [4, 5].

The HC should be run together with E. V. Pozharsky Histogram Manager program (GM) as a whole complex [3]. In this complex GM performs operations of conversion of time series into histograms and construction of distribution of intervals between histograms marked in results of HC comparison as similar. A histogram massif obtained with GM is exported into HC, which performs their comparison. The result is reloaded into GM for construction of interval distributions.

2 Main stages of histograms comparison with the GM-HC program complex

Fig. 1 shows a GM conversion of a time series of results of successive measurements of ^{239}Pu alpha-activity into series of correspondent histograms, illustrating the work of GM program.

Further the histograms are exported into HC. After the histograms are loaded, preprocessing starts — a corresponding normal distribution is calculated for each histogram. Calculation is made according to equation

$$f(x) = \frac{1}{\sigma\sqrt{2\pi}} \exp\left(-\frac{(x-\mu)^2}{2\sigma^2}\right) \sum_{i=1}^{L} a_i \,. \qquad (1)$$

Conversion of histograms following deduction of appropriately picked normal distribution is shown at Fig. 2.

As one can see from Fig. 2, histogram structural features essential for our analysis in "replicas" remain unchanged and become more distinct. Comparison of "replicas" in a suggested program is realized in two versions: simple and detailed. A simple comparison implies relative shift and mirroring in a pair of "replicas".

Detailed comparison implies additionally compressing-stretching of one of the "replicas" — from 0.5 to 1.5 of an initial length in 10% increment. Consequently, a detailed comparison requires higher consumption of computing time.

Fig. 3 demonstrates process of replicas coinciding necessary for following determination of correlation coefficient maximal achievable for this pair.

2.1 Picking of correlation coefficients range

Results of comparison of each pair are entered into a table as values of maximal achievable correlation coefficient and curve areas ratio. A pair is regarded as similar when values of its correlation coefficient and curve areas ratio overshoot corresponding values of a threshold filter. Threshold values are set by a user. Criterion of threshold meanings is presence or absence of expressed intervals of reoccurrence of similar pairs in a result of comparison. Experience of using the program tells there are not more than 2 versions of combinations of threshold values allowing expressiveness of correspondingly 2 alternately expressed intervals, or expressed intervals are absent.

2.2 Analysis of comparison results and construction of similar pairs numbers distribution according to values of time intervals separating them in GM

A result of program comparison is entered into a binary file of a histograms similarity table in GM-supported GMA format

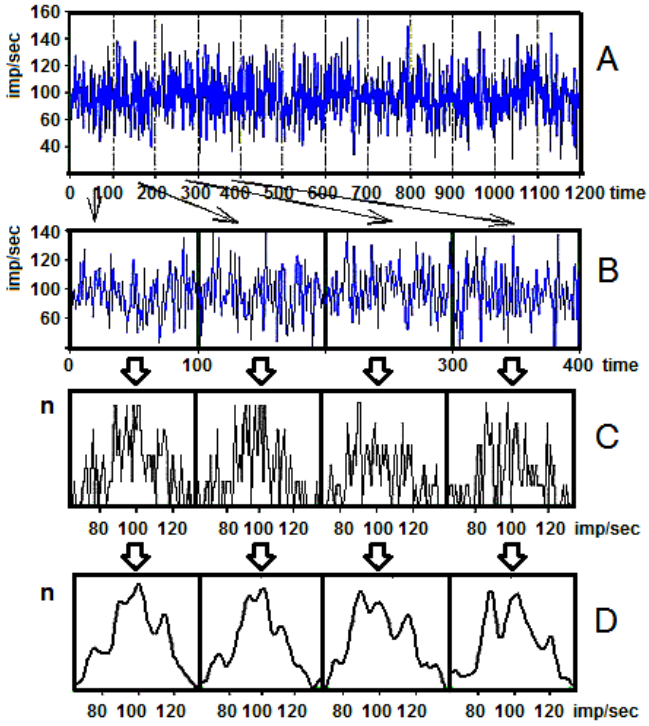

Fig. 1: Steps of histograming with GM program [1] exemplified by measurements of radioactivity a — a fragment of time series of measurement results. X-axis is time (sec.); Y-axis is numbers of alpha-decays per a second b — a time series is divided into non-overlapping sections, 100 successive numbers each c — each section is followed by a histogram (X-axis is value of activity (imp/sec); Y-axis is numbers of measurements corresponding to a value) d — the histograms from 1-c are seven-times smoothed with "moving summation" or with "a window" equal, for example, to 4; typical histogram shapes can be seen.

(description of GMA format ia a courtesy of the GM author, E. V. Pozharsky). GM calculates time interval separating each histogram pair marked as similar in the table and constructs a graphical display of intervals occurrence, i.e. histogram.

3 Examples of GM-HC complex use at determination of near-a-day periods of similar shape histograms reoccurrence and examination of "palindrome phenomenon"

3.1 Near-a-day periods

Fig. 4 presents an example of visual ("expert") comparison of histograms resulting measurements of 239Pu alpha-activity. Each histogram was constructed by 60 results of one-minute measurements. Comparison with total mixing (randomization) was made by T. A. Zenchenko. A whole series contained 143 one-hour histograms. 1,592 similar pairs were picked. The figure shows distribution of numbers of similar pairs according to values of time intervals separating them.

There are sharp extremes at the intervals equal to 1, 24 and 48 hours at the figure. These extremes correspond to a

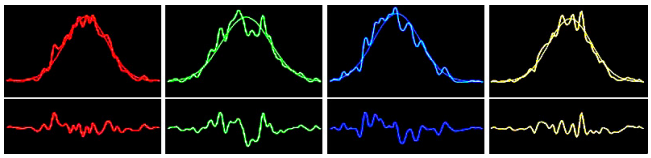

Fig. 2: The upper line is histograms with applied correspondent normal curves; the lower line is results of normal curves deduction from histograms; the resulting curves are, in fact, "replicas" of fine structures of fluctuation amplitudes spectrum.

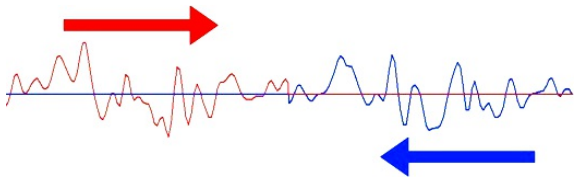

Fig. 3: Illustration of "simple" comparison. Direction of shift is pointed by arrows. Two these experiments were performed on April 8, 2011 (the left histogram arc) and April 9, 2011 (the right histogram arc).

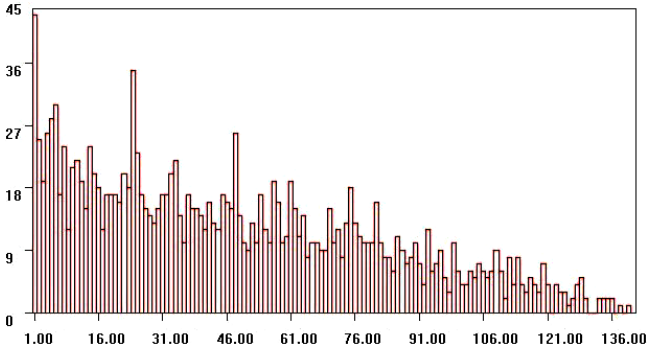

Fig. 4: Results of comparison of one-hour histograms constructed by results of ^{239}Pu alpha-activity measurements from July 7 to July 15, 2000, in Puschino. X-axis is intervals (hours); Y-axis is number of similar pairs corresponding to value of interval. (Taken from [1].)

"near zone effect" — maximal probability of realization of similar histograms in nearest, neighboring, intervals and their realization with near-a-day periods. Total mixing (randomization) of histogram series guaranties reliability of regularities revealed in expert comparison [1].

Fig. 5 presents result of automatic comparison, performed by HC computer program in the same task. It is clear that in reproduction of main effects the program is rather inferior to the expert in quality of histograms comparison.

3.2 "Palindrome effect" [1]

Figs. 7 and 8 show one of the main phenomena of "macroscopic fluctuations" — a palindrome effect — reproduced with HC program.

A "palindrome effect" is conditioned by dependence of a histogram shape from correlation of Earth motion directions: at its axial rotation and circumsolar movement. In a day-time axial rotation of Earth is antisircumsolar. In night-time the

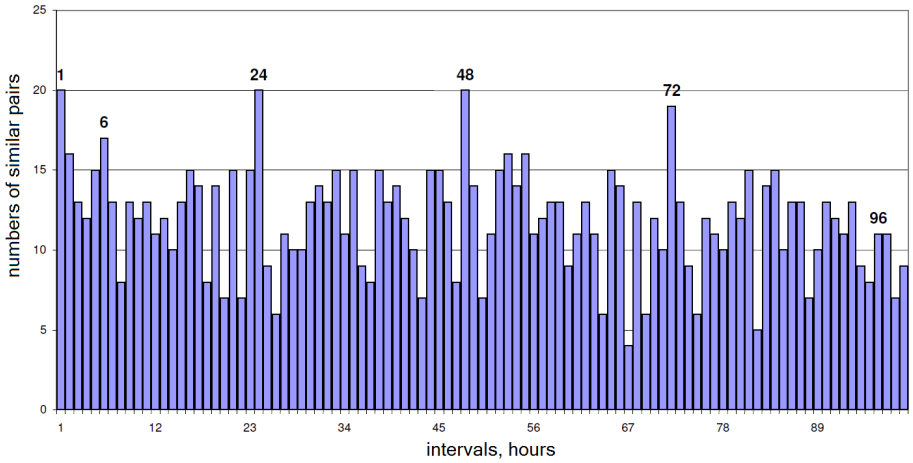

Fig. 5: Diurnal periods revealed at comparison of non-smoothed one-hour histograms by HC program. The histograms are computed by measurements of ^{239}Pu alpha-activity with a collimator-free counter since February 10 till March, 1, 2010.

both movements are co-directed. Succession of "day-time" histograms shapes was shown to repeat inversely in nights. In other words, one the same "text" is "read" forward and backward forming a palindrome. The moments of day-night transitions are 6 pm by local time and of night-day transitions are 6 am. Comparison of forward and backward sequences gives a valuable possibility to verify objectiveness of obtained distributions. The same histograms are compared. Result of comparison depends on direction of sequences only.

Figs. 6–8 present results of "palindrome effect" examination at measurements of fluctuations of intensities of light beam and ^{239}Pu alpha-decay in two ways: at expert (visual) estimation of histograms similarity (Fig. 6) and at HC comparison (Figs. 7 and 8). Fig. 6 is an expert comparison of histograms constructed by 60 one-second measurements (that is, during 1 minute). Figs. 7 and 8 show the results of comparison of 10-minute histograms with the HC program.

As one can see from Figs. 6–8, when histograms constructed by measurements of a light beam fluctuations [4] or fluctuations of ^{239}Pu alpha-decay intensities [1] are compared, a distinct palindrome effect can be observed. There is high probability of synchronous similarity of "day-time" histograms series with inverse series of night-time histograms. There is no similarity of synchronous histograms when a day-time series is compared with a direct (non-inverted) night-time series. Nevertheless comparison of histograms with HC programs gives "coarser" results, with 10 minutes interval, versus one-minute intervals at expert comparison.

The illustrations show principal availability of the HC program for examination of fine structure of histograms. But expert comparison determines similar histograms more specially, HC gives much higher "background" of stochastic shapes. Besides, these figures show similarity of palindrome effects at measurements of fluctuations of alpha-decay intensity, that is, independence of a macroscopic fluctuations phenomenon from nature of processes under examination [1].

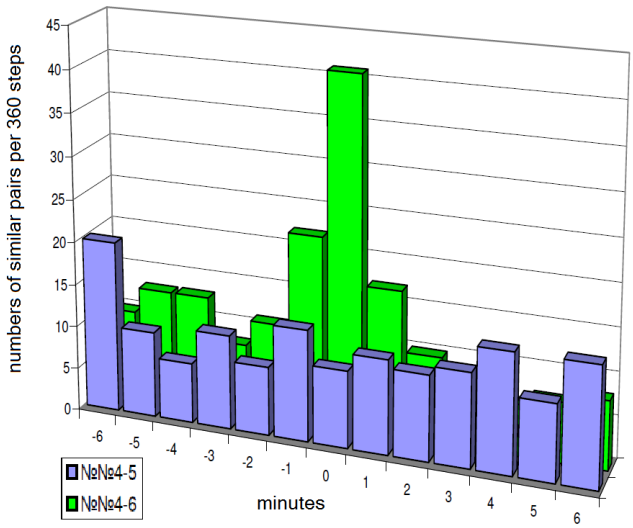

Fig. 6: Expert comparison. A palindrome effect in an experiment with measurements of fluctuations of light-diode light beam intensities. High similarity of synchronous one-minute histograms at comparison of "day-time" and "night-time" histograms when one series is inverted and absence of similarity at the absence of inversion. Measurements on April 6, 2011. X-axis is one-minute intervals; Y-axis is number of similar pairs corresponding to an interval.

4 Conclusions

1. Application of HC program allows reproduction of main effects of "macroscopic fluctuations" phenomenon.
2. Nevertheless, range of correlation coefficients values is to be picked up each time complicating the work.
3. The optimal way is combination of expert analysis with estimation of confidence of main conclusion with GM-HC combination.

You can get text and manual of the program from its author after e-mail request via: 2801218@gmail.com

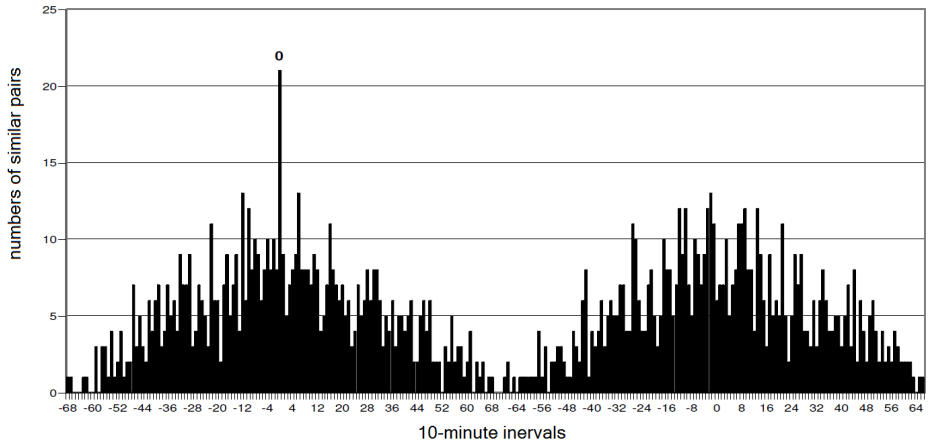

Fig. 7: Comparison of 10-minute histograms by the HC computer program. A palindrome effect in experiments with measurements of fluctuations of light-diode light beam intensities. Left is distribution of numbers of similar histogram pairs at comparison of "day-time" (since 6 am till 6 pm April 6, 2011) series histograms with inverse "night-time" (since 6 pm April, 27 till 6 am April 7, 2011). Right — the same at comparison of series without inversion.

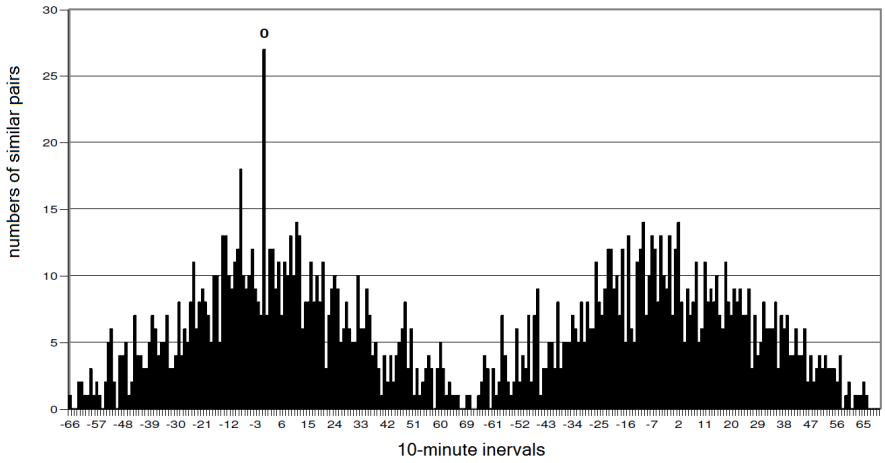

Fig. 8: Comparison of 10-minute histograms by computer HC program. Palindrome effect in experiments on measurements of ^{239}Pu alpha-activity with West-directed collimator. Left — distribution of numbers of similar histograms at comparison of histograms of "day-time" series (from 6 am to 6 pm May 27, 2005) with inverse "night-time" series of histograms (from 6 pm May 27 to 6 am May 28, 2005); right — the same at comparison of series without inversion.

Acknowledgements

Author is grateful to S. E. Shnoll for formulation of the problem, provided materials and essential discussion; V. A. Kolombet for essential discussion and his attention to the work; E. V. Pozharsky for consulting in work with GM interfaces and Professor V. I. Maslyankin ("Programming technology", Russian New University) for tutoring.

Submitted on March 11, 2012 / Accepted on March 16, 2012

References

1. Shnoll S. E. Cosmic Physical Factors in Random Processes. Svenska Fisikarkivet, Stockholm, 2009, (*in Russian*).
2. Udaltsova N. V., Possible cosmophysical casuality of parameters of biochemical and physic-chemical processes. *PhD theses Inst. Biophysics, USSR Acad. Ssi.*, 1990, (*in Russian*).
3. Shnoll S. E., Kolombet V. A., Pozharsky E. V., Zenchenko T. A., Zvereva I. M., Konradov A. A. Illustration of synchronism of changes of fine structure of measurement results distribution exemplified by radioactive decay of radium family isotopes. *Biofizika*, 1998, v. 43 (4), 732–735 (*in Russian*).
4. Rubinshtein I. A., Shnoll S. E., Kaminsky A. V., Kolombet V. A., Astashev M. A., Shapovalov S. N., Bokalenko B. I., Andreeva A. A., Kharakoz D. P. Dependence of changes of histogram shapes from time and space direction is the same when intensities of fluctuations of both of light-diode provided light flux and ^{239}Pu alpha-activity are measured. *Progress in Physics* , 2012, v. 3, 17–24 (this issue).
5. Shnoll S. E., Astashev M. A., Rubinshtein I. A., Kolombet V. A., Shapovalov S. N., Bokalenko B. I., Andreeva A. A., Kharakoz D. P., Melnikov I. A. Synchronous measurements of alpha-decay of ^{239}Pu carried out at North Pole, Antarctic, and in Puschino confirm that the shapes of the respective histograms depend on the diurnal rotation of the Earth and on the direction of the alpha-particle beam. *Progress in Physics*, 2012, v.3, 11–16 (this issue).

The Radial Electron Density in the Hydrogen Atom and the Model of Oscillations in a Chain System

Andreas Ries
Universidade Federal de Pernambuco, Centro de Tecnologia e Geociências, Laboratório de Dispositivos e Nanoestruturas,
Rua Acadêmico Hélio Ramos s/n, 50740-330 Recife – PE, Brazil
E-mail: andreasries@yahoo.com

The radial electron distribution in the Hydrogen atom was analyzed for the ground state and low-lying excited states by means of a fractal scaling model originally published by Müller in this journal. It is shown that Müller's standard model is not fully adequate to fit these data and an additional phase shift must be introduced into its mathematical apparatus. With this extension, the radial expectation values could be expressed on the logarithmic number line by very short continued fractions where all numerators are Euler's number. Within the rounding accuracy, no numerical differences between the expectation values (calculated from the wavefunctions)and the corresponding modeled values exist, so the model matches these quantum mechanical data exactly. Besides that, Müller's concept of proton resonance states can be transferred to electron resonances and the radial expectation values can be interpreted as both, proton resonance lengths and electron resonance lengths. The analyzed data point to the fact that Müller's model of oscillations in a chain system is compatible with quantum mechanics.

1 Introduction

The radial electron probability density in the Hydrogen atom was analyzed by a new fractal scaling model, originally published by Müller [1–3] in this journal. This model is basing on four principal facts:

1. The proton is interpreted as an oscillator.
2. Most matter in the universe is provided by protons, therfore the proton is *the dominant oscillation state* in all the universe.
3. Space is not considered as completely empty, consequently all proton oscillators are somehow coupled to each other. A quite simple form to consider such a coupling is the formation of a chain of proton harmonic oscillators.
4. Provided that items 1–3 are correct, every process or state in the universe which is abundantly realized or allowed to exist over very long time scales, is consequently coupled to the proton oscillations, and should retain some properties that can be explained from the mathematical structure of a chain of proton harmonic oscillators.

Müller has shown that a chain of similar harmonic oscillators generates a spectrum of eigenfrequencies, that can be expressed by a continued fraction equation [2]

$$f = f_p \exp S, \tag{1}$$

where f is any natural oscillation frequency of the chain system, f_p the oscillation frequency of one proton and S the continued fraction corresponding to f. S was suggested to be in the canonical form with all partial numerators equal 1 and the partial denominators are positive or negative integer values:

$$S = n_0 + \cfrac{1}{n_1 + \cfrac{1}{n_2 + \cfrac{1}{n_3 + \ldots}}}. \tag{2}$$

Besides the canonical form, Müller proposed fractions with all numerators equal 2 and all denominators are divisible by 3. Such fractions divide the logarithmic scale in allowed values and empty gaps, i.e. ranges of numbers which cannot be expressed with this type of continued fractions.

In three previous articles [4–6] it was shown that the model works quite well when all the numerators were substituted by Euler's number, so that

$$S = n_0 + \cfrac{e}{n_1 + \cfrac{e}{n_2 + \cfrac{e}{n_3 + \ldots}}}. \tag{3}$$

In this work, the attention has been focused to the spatial electron distribution in the Hydrogen atom, considering the ground state (n = 1) and the first low-lying excited electronic states (n = 2–6).

In the Hydrogen atom, the distance between the electron and the proton is always very small and quantum mechanics allows to calculate the exact spatial electron density distribution. If the proton is somehow oscillating and Müller's model applies, one can expect a characteristic signature in the set of radial expectation values.

Actually these values compose an extremely interesting data set to analyze, since the expectation values can be calculated by quantum mechanics from exact analytical wave-

functions and do not have any measurement error (errors in physical constants such as a_0 and $\hbar$ can be neglected).

Therefore, it can be requested that Müller's model must reproduce these expectation values *exactly*, which is indeed possible, but only when introducing a further modification to the model.

2 Data sources and computational details

When considering polar coordinates, the solutions of the non-relativistic Schrödinger equation $\hat{H}\Psi = E\Psi$ for a spherical potential can be written in the form

$$\Psi(r, \theta, \phi) = R(r)\Theta(\theta)\Phi(\phi),$$

where $R(r)$ is the so-called radial part of the wavefunction Ψ, and the functions $\Theta(\theta)$ and $\Phi(\phi)$ are the angular parts.

For every orbital or wavefunction, the probability to find the electron on a shell with inner radius r and outer radius $r + dr$ is proportional to r^2R^2dr (note that the functions as given in Table 1 are not normalized). Following the formalism of quantum mechanics, the average or expectation value $\langle r \rangle$ was calculated by numerical integration

$$\langle r \rangle = N \int_0^\infty r^3R^2dr, \tag{4}$$

where N is the normalization constant so that holds:

$$N \int_0^\infty r^2R^2dr = 1.$$

Table 1 displays the radial part $R(Z, r)$ for the orbitals 1s to 6h of hydrogen-like atoms together with the corresponding radial expectation values (for $Z = 1$, wavefunctions taken from reference [7]). The expectation values are given in Å and were rounded to three significant digits after decimal point.

In a second step, these numerical values were expressed on the logarithmic number line by continued fractions. Numerical values of continued fractions were always calculated using the the Lenz algorithm as indicated in reference [8].

3 Results and discussion

3.1 The standard model is insufficient

In order to interpret the expectation values $\langle r \rangle$ as proton resonance lengths, following strictly the formalism of previous articles, it must be written:

$$\ln \frac{\langle r \rangle}{\lambda_C} = p + S, \tag{5}$$

where S is the continued fraction as given in equation 3, $\lambda_C = \frac{h}{2\pi mc}$ is the reduced Compton wavelength of the proton with the numerical value $2.103089086 \times 10^{-16}$ m. In the following tables, $p + S$ is abbreviated as $[p; n_0 \mid n_1, n_2, n_3, \dots]$. The free link n_0 and the partial denominators n_i are integers divisible by 3. For convergence reason, one has to include $|e{+}1|$ as allowed partial denominator. This means the free link n_0 is allowed to be $0, \pm3, \pm6, \pm9 \dots$ and all partial denominators n_i can take the values $e{+}1, -e{-}1, \pm6, \pm9, \pm12 \dots$.

For consistency with previous publications, the following conventions hold: a data point is considered as an outlier (i.e. does not fit into Müller's model), when its continued fraction representation produces a numerical error higher than 1%. The numerical error is always understood as the absolute value of the difference between $\langle r \rangle$ from quantum mechanics (given in Table 1), and the value obtained from the evaluation of the corresponding continued fraction.

It was found that the complete set of radial expectation values can be interpreted as proton resonance lengths without any outliers according to equation 5 (results not shown). However, small numerical errors were still present. Having in mind that this is a data set without measurement errors, this result is not satisfying.

From the obvious fact that the wavefunction is an electron property, it arouse the idea to interpret the data set as electron resonance lengths. Then, a fully analogous equation can be set up:

$$\ln \frac{\langle r \rangle}{\lambda_{C_{electron}}} = p + S, \tag{6}$$

where $\lambda_{C_{electron}}$ is the reduced Compton wavelength of the electron with the numerical value $3.861592680 \times 10^{-13}$ m.

Again the expectation values could be interpreted as electron resonance lengths according to equation 6 without the presence of outliers, but some numerical errors remained (results not shown).

Since the aforementioned equations do not reproduce the dataset exactly as proton or electron resonance lengths, possible changes of the numerator were investigated.

Müller had already proposed continued fractions with all numerators equal 2 in one of his publications [9]. As a first numerical trial, the number of outliers was determined when modeling the data set with numerators from 2.0 to 3.0 (step-size 0.05). Figure 1 displays the results for both, proton and electron resonances. It turned out that number 2 must be excluded from the list of possible numerators, as outliers are present. Moreover, the results suggest that the whole range from 2.55 to 2.85 can be used as numerator in equations 5 and 6 without producing outliers, thus, another criterium must be applied to determine the correct numerator.

Considering only the range of numerators which did not produce outliers, the sum of squared residuals (or squared numerical errors) was calculated. It strongly depends on the numerator (see Figure 2). Again the results are not satisfying. As can be seen, considering electron resonances, the "best numerator" is 2.70, while for proton resonances it is 2.78, de-

Table 1: Radial wavefunctions $R(Z, r)$ of different orbitals for hydrogen-like atoms together with the corresponding radial expectation values according to equation 4 ($Z = 1$ assumed). $\rho = \frac{2Zr}{na_0}$, n = main quantum number, a_0 = Bohr radius, Z = atomic number.

Radial wavefunction $R(Z, r)$	$\langle r \rangle$ [Å]
$R_{1s} = (Z/a_0)^{\frac{3}{2}} 2e^{-\frac{\rho}{2}}$	0.794
$R_{2s} = \frac{(Z/a_0)^{\frac{3}{2}}}{2\sqrt{2}}(2-\rho)e^{-\frac{\rho}{2}}$	3.175
$R_{2p} = \frac{(Z/a_0)^{\frac{3}{2}}}{2\sqrt{6}}\rho e^{-\frac{\rho}{2}}$	2.646
$R_{3s} = \frac{(Z/a_0)^{\frac{3}{2}}}{9\sqrt{3}}\left(6-6\rho+\rho^2\right)e^{-\frac{\rho}{2}}$	7.144
$R_{3p} = \frac{(Z/a_0)^{\frac{3}{2}}}{9\sqrt{6}}(4-\rho)\rho e^{-\frac{\rho}{2}}$	6.615
$R_{3d} = \frac{(Z/a_0)^{\frac{3}{2}}}{9\sqrt{30}}\rho^2 e^{-\frac{\rho}{2}}$	5.556
$R_{4s} = \frac{(Z/a_0)^{\frac{3}{2}}}{96}\left(24-36\rho+12\rho^2-\rho^3\right)e^{-\frac{\rho}{2}}$	12.700
$R_{4p} = \frac{(Z/a_0)^{\frac{3}{2}}}{32\sqrt{15}}\left(20-10\rho+\rho^2\right)\rho e^{-\frac{\rho}{2}}$	12.171
$R_{4d} = \frac{(Z/a_0)^{\frac{3}{2}}}{96\sqrt{5}}(6-\rho)\rho^2 e^{-\frac{\rho}{2}}$	11.113
$R_{4f} = \frac{(Z/a_0)^{\frac{3}{2}}}{96\sqrt{35}}\rho^3 e^{-\frac{\rho}{2}}$	9.525
$R_{5s} = \frac{(Z/a_0)^{\frac{3}{2}}}{300\sqrt{5}}\left(120-240\rho+120\rho^2+20\rho^3+\rho^4\right)e^{-\frac{\rho}{2}}$	19.844
$R_{5p} = \frac{(Z/a_0)^{\frac{3}{2}}}{150\sqrt{30}}\left(120-90\rho+18\rho^2-\rho^3\right)\rho e^{-\frac{\rho}{2}}$	19.315
$R_{5d} = \frac{(Z/a_0)^{\frac{3}{2}}}{150\sqrt{70}}\left(42-14\rho+\rho^2\right)\rho^2 e^{-\frac{\rho}{2}}$	18.257
$R_{5f} = \frac{(Z/a_0)^{\frac{3}{2}}}{300\sqrt{70}}(8-\rho)\rho^3 e^{-\frac{\rho}{2}}$	16.669
$R_{5g} = \frac{(Z/a_0)^{\frac{3}{2}}}{900\sqrt{70}}\rho^4 e^{-\frac{\rho}{2}}$	14.552
$R_{6s} = \frac{(Z/a_0)^{\frac{3}{2}}}{2160\sqrt{6}}\left(720-1800\rho+1200\rho^2+300\rho^3+30\rho^4-\rho^5\right)e^{-\frac{\rho}{2}}$	28.576
$R_{6p} = \frac{(Z/a_0)^{\frac{3}{2}}}{432\sqrt{210}}\left(840-840\rho+252\rho^2-28\rho^3+\rho^4\right)\rho e^{-\frac{\rho}{2}}$	28.046
$R_{6d} = \frac{(Z/a_0)^{\frac{3}{2}}}{864\sqrt{105}}\left(336-168\rho+24\rho^2-\rho^3\right)\rho^2 e^{-\frac{\rho}{2}}$	26.988
$R_{6f} = \frac{(Z/a_0)^{\frac{3}{2}}}{2592\sqrt{35}}\left(72-18\rho+\rho^2\right)\rho^3 e^{-\frac{\rho}{2}}$	25.401
$R_{6g} = \frac{(Z/a_0)^{\frac{3}{2}}}{12960\sqrt{7}}(10-\rho)\rho^4 e^{-\frac{\rho}{2}}$	23.284
$R_{6h} = \frac{(Z/a_0)^{\frac{3}{2}}}{12960\sqrt{77}}\rho^5 e^{-\frac{\rho}{2}}$	20.638

spite presenting a local minimum at 2.70 too. However, numerators different from e are inconsistent with previous publications. The fact that these "best numerators" are numerically very close to Euler's number, suggests that the choice of e as numerator is probably correct and something else in the model must be changed for this particular dataset.

For any common experimental data set, the here found numerical inconsistencies could be explained with measurement errors. One could even think that Müller's model is just too simple to reproduce nature's full reality; then the numerical deviations could also be explained by the insufficiency of the model itself. Fortunately the high accuracy of the expec-

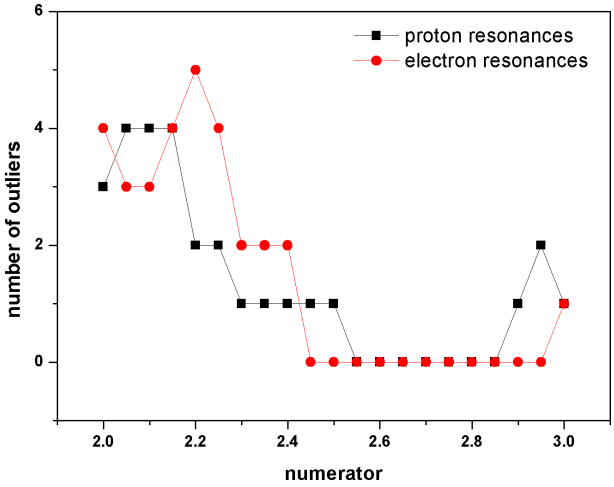

Fig. 1: Determination of the correct numerator for the dataset of expectation values (equations 5 and 6): the number of outliers as a function of the tested numerator.

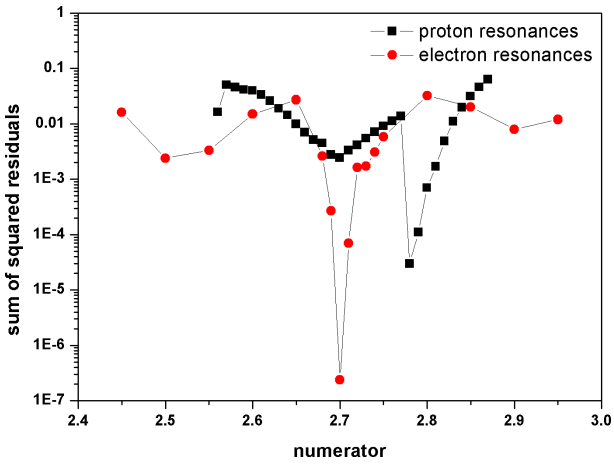

Fig. 2: Determination of the correct numerator for the dataset of expectation values (equations 5 and 6): the sum of squared residuals as a function of the tested numerator.

tation values creates the opportunity to test Müller's model very critically and to extend it.

3.2 Extending Müller's model

It is now shown that the following extension provides a solution, so that (i) Euler's number can be persist as numerator, and (ii) the whole dataset can be expressed by short continued fractions without any numerical errors, which means, this extended model reproduces the dataset *exactly*.

An additional phase shift δ was introduced in equations 5 and 6. For proton resonances, it can then be written:

$$\ln \frac{\langle r \rangle}{\lambda_C} = \delta + p + S. \qquad (7)$$

And analogously for electron resonances:

$$\ln \frac{\langle r \rangle}{\lambda_{C_{electron}}} = \delta + p + S. \qquad (8)$$

As shown in previous articles, the phase shift p varies among the dataset, so that some data points take $p = 0$ and others $p = 3/2$. Contrary to this, the phase shift δ must be equal for all data points in the set. This means the fractal spectrum of resonances is shifted on the logarithmic number line and the principal nodes are not more at $0, \pm 3, \pm 6, \pm 9 \ldots$, but now at $0 + \delta, \pm 3 + \delta, \pm 6 + \delta, \pm 9 + \delta \ldots$.

The underlying physical idea is that δ should be a small positive or negative number, characterizing a small deviation from Müller's standard model. To guarantee that the model does not become ambiguous, values of $|\delta|$ must always be smaller than 3/2.

For the here considered data set, the phase shift δ could be determined as a *very small number*, with the consequence that all numerical errors vanished (were smaller than 0.001 Å). The numerical values were $\delta = 0.017640$ when interpreting the data as proton resonances and $\delta = 0.002212$ in case of electron resonances. Tables 2 and 3 show the continued fraction representations when interpreting the expectation values as proton and electron resonances, respectively.

3.3 Interpretation

As can be seen, when accepting a *small* phase shift δ, the radial expectation values can be perfectly interpreted as both, proton and electron resonances. Besides that, the continued fraction representations are equal for proton and electron resonances, only the free link and the phase shift p differ. This is unavoidable due to the fact that different reference Compton wavelengths were used; so the logarithmic number line was calibrated differently.

The free link and the phase shift p are parameters which basically position the data point on the logarithmic number line, indicating the principal node. Then the first partial denominator determines whether the data point is located before or after this principal node. So the data point can be either in a compression or expansion zone, thus, now a specific property of its oscillation state is indicated. The equality of the set of partial denominators in the continued fraction representations is a necessary requirement for interpreting the expectation values as both, proton and electron resonances. Both oscillators must transmit at least qualitatively the same "oscillation property information" to the wavefunction.

However, when accepting the phase shift idea, it is always mathematically possible to interprete *any* set of proton resonances as a set of phase-shifted electron resonances. So what are the physical arguments for associating the expectation values to both oscillators?

- In an atom, electrons and the nucleus share a very small volume of space. The electron wavefunction is most

Table 2: Continued fraction representation of the radial expectation values of Hydrogen orbitals according to equation 7, considering proton resonances (δ = 0.017640).

Orbital	Continued fraction representation of $\langle \mathbf{r} \rangle$
1s	[0; 12 | e+1, -6, -6] [1.5; 12 | -e-1, -9]
2s	[0; 15 | -e-1, 9, e+1] [1.5; 12 | e+1, 24, 6]
2p	[0; 15 | -e-1, e+1, -e-1, 12, e+1] [1.5; 12 | 6, -e-1, 6, -e-1]
3s	[0; 15 | 132, -e-1]
3p	[0; 15 | -48, -6]
3d	[0; 15 | -12, 12, e+1]
4s	[0; 15 | e+1, e+1, -6, 6] [1.5; 15 | -e-1, e+1, 27, -e-1]
4p	[1.5; 15 | -e-1, e+1, -6, e+1, e+1, e+1]
4d	[0; 15 | 6, -21, -e-1, e+1]
4f	[0; 15 | 9, -15, 9]
5s	[1.5; 15 | -6, 45]
5p	[1.5; 15 | -6, 6, e+1, -e-1, 6]
5d	[0; 15 | e+1, -e-1, e+1, 6, -e-1, -12] [1.5; 15 | -6, e+1, -e-1, e+1, -9]
5f	[0; 15 | e+1, -e-1, -e-1, e+1, -33] [1.5; 15 | -e-1, -e-1, -e-1, e+1, -6]
5g	[0; 15 | e+1, -471] [1.5; 15 | -e-1, 15, 9, e+1]
6s	[1.5; 15 | -30, e+1, -18]
6p	[1.5; 15 | -24, -9, e+1, -e-1]
6d	[1.5; 15 | -18, -27]
6f	[1.5; 15 | -12, -e-1, e+1, 12]
6g	[1.5; 15 | -9, -21]
6h	[1.5; 15 | -6, -6, 6, -e-1, 6]

Table 3: Continued fraction representation of the radial expectation values of Hydrogen orbitals according to equation 8, considering electron resonances (δ = 0.002212).

Orbital	Continued fraction representation of $\langle \mathbf{r} \rangle$
1s	[0; 6 | -e-1, -9] [1.5; 3 | e+1, -6, -6]
2s	[0; 6 | e+1, 24, 6] [1.5; 6 | -e-1, 9, e+1]
2p	[0; 6 | 6, -e-1, 6, -e-1] [1.5; 6 | -e-1, e+1, -e-1, 12, e+1]
3s	[1.5; 6 | 132, -e-1]
3p	[1.5; 6 | -48, -6]
3d	[1.5; 6 | -12, 12, e+1]
4s	[0; 9 | -e-1, e+1, 27, -e-1] [1.5; 6 | e+1, e+1, -6, 6]
4p	[0; 9 | -e-1, e+1, -6, e+1, e+1, e+1]
4d	[1.5; 6 | 6, -21, -e-1, e+1]
4f	[1.5; 6 | 9, -15, 9]
5s	[0; 9 | -6, 45]
5p	[0; 9 | -6, 6, e+1, -e-1, 6]
5d	[0; 9 | -6, e+1, -e-1, e+1, -9] [1.5; 6 | e+1, -e-1, e+1, 6, -e-1, -12]
5f	[0; 9 | -e-1, -e-1, -e-1, e+1, -6] [1.5; 6 | e+1, -e-1, -e-1, e+1, -33]
5g	[0; 9 | -e-1, 15, 9, e+1] [1.5; 6 | e+1, -471]
6s	[0; 9 | -30, e+1, -18]
6p	[0; 9 | -24, -9, e+1, -e-1]
6d	[0; 9 | -18, -27]
6f	[0; 9 | -12, -e-1, e+1, 12]
6g	[0; 9 | -9, -21]
6h	[0; 9 | -6, -6, 6, -e-1, 6]

basically an electron property, always existing in close proximity to the nucleus (protons). From this it would not be a surprise that both oscillators contribute to the properties of the wavefunction. In general, one can now speculate that particularly physical parameters related to an atomic wavefunction are hot candidates to be interpretable as electron resonances.

- The phase shift was not invented to justify electron resonances, it is also required for an exact reproduction of the data set through proton resonances.
- When considering Müller's standard model (equations 5 and 6), the sum of squared residuals is much lower when interpreting the data as electron resonances. In this case the "best numerator" is also closer to Euler's number (see Fig. 2). Therefore, the wavefunction is principally governed by the electron oscillations. Certainly the proton oscillations influence the system too, they can be interpreted as a perturbation. The system tends to adjust to both oscillators and this seems to be the cause of the observed phase shifts. Hopefully, similar data will confirm this in near future.

4 Conclusions

Müller's model must be extended in two ways. First, it must be recognized that electron resonances exist in the universe as proton resonances do, and the same mathematical formalism for a chain of proton oscillators can be applied to a chain of electron oscillators. Second, an additional phase shift δ is

proposed to provide a reasonable mathematical extension of the model.

Of course, much more data must be analyzed and the future will show if this extended model can stand and give useful results when applying to other data sets. Particularly interesting for analyses would be quite accurate data from quantum mechanics.

Now one has to ask regarding previously published papers on this topic [4–6]: are there any results that must be reconsidered? The answer is definitively yes. In reference [4], masses of elementary particles were analyzed and only for 86% of the particles a continued fraction expression could be found. There is high probability that this exceptional high number of outliers (14%, nowhere else found) can be reduced considering a phase shift δ; or different phase shifts δ can put the elementary particles into different groups. In another paper [6], half-lifes of excited electronic states of atoms were found to be proton resonance periods, however, a possible interpretation as electron resonance periods has not been attempted yet. Possibly a small phase shift could here also reduce the number of outliers. This everything is now subject of future research.

Acknowledgments

The author greatly acknowledges the financial support from the Brazilian governmental funding agencies FACEPE and CNPq.

Submitted on May 2, 2012 / Accepted on May 06, 2012

References

1. Müller H. Fractal scaling Models of resonant oscillations in chain systems of harmonic oscillators. *Progress in Physics*, 2009, v. 2 72–76.
2. Müller H. Fractal scaling models of natural oscillations in chain systems and the mass distribution of the celestial bodies in the solar system. *Progress in Physics*, 2010, v. 1 62–66.
3. Müller H. Fractal scaling models of natural oscillations in chain systems and the mass distribution of particles. *Progress in Physics*, 2010, v. 3 61–66.
4. Ries A., Fook M.V.L. Fractal structure of nature's preferred masses: Application of the model of oscillations in a chain system. *Progress in Physics*, 2010, v. 4, 82–89.
5. Ries A., Fook M.V.L. Application of the Model of Oscillations in a Chain System to the Solar System. *Progress in Physics*, 2011, v. 1, 103–111.
6. Ries A., Fook M.V.L. Excited Electronic States of Atoms described by the Model of Oscillations in a Chain System. *Progress in Physics*, 2011, v. 4, 20–24.
7. Pauling L., Wilson E.B. Introduction to quantum mechanics. McGraw-Hill, New York, 1935.
8. Press W. H., Teukolsky S. A., Vetterling W. T., Flannery B. P. Numerical recipes in C. Cambridge University Press, Cambridge, 1992.
9. Otte R., Müller H.. German patent No. DE102004003753A1, date: 11.08.2005

Gravitational Acceleration and the Curvature Distortion of Spacetime

William C. Daywitt
National Institute for Standards and Technology (retired), Boulder, Colorado
E-mail: wcdaywitt@me.com

The Crothers solution to the Einstein vacuum field consists of a denumerable infinity of Schwarzschild-like metrics that are non-singular everywhere except at the point mass itself. When the point-mass distortion from the Planck vacuum (PV) theory is inserted into the Crothers calculations, the combination yields a composite model that is physically transparent. The resulting static gravitational field using the Crothers metrics is calculated and compared to the Newtonian gravitational field and the gravitational field associated with the black hole model.

1 Newtonian Introduction

When a test mass m' travels in the gravitational field of a point mass m situated at $r = 0$, the Newtonian theory of gravity predicts that the acceleration experienced by the test mass

$$\frac{d^2r}{dt^2} = -\frac{mG}{r^2} \tag{1}$$

is *independent of the mass* m'. In this theory the relative magnitudes of m' and m are arbitrary and lead to the following equation for the magnitude of the gravitational force between the two masses

$$\frac{m'mG}{r^2} = \frac{(m'c^2/r)(mc^2/r)}{c^4/G}$$
$$= \left(\frac{m'c^2/r}{c^4/G}\right)\left(\frac{mc^2/r}{c^4/G}\right)\frac{c^4}{G} \tag{2}$$

when expressed in terms of the ratio c^4/G.

In the PV theory [1] the force mc^2/r represents the curvature distortion the mass m exerts on the PV state (and hence on spacetime), and the ratio

$$\frac{c^4}{G} = \frac{m_*c^2}{r_*} \tag{3}$$

represents the maximum such curvature force, where m_* and r_* are the mass and Compton radius of the Planck particles constituting the PV. The corresponding relative curvature force is represented by the n-ratio

$$n_r \equiv \frac{mc^2/r}{c^4/G} = \frac{mc^2/r}{m_*c^2/r_*} \tag{4}$$

which is a direct measure of the curvature distortion exerted on spacetime and the PV by the point mass. Since the minimum distortion is 0 ($m = 0$ or $r \to \infty$) and the maximum is 1, the n-ratio is physically restricted to the range $0 \le n_r \le 1$ as are the equations of general relativity [2].

The important fiducial point at $n_{r_s} = 0.5$ is the Schwarzschild radius $r_s = 2mr_*/m_*$, where

$$rn_r = \frac{mc^2}{m_*c^2/r_*} = r_s n_{r_s} = 0.5r_s\,. \tag{5}$$

The acceleration (1) can now be expressed exclusively in terms of the relative curvature distortion n_r:

$$a(n_r) = -\frac{d^2r}{dt^2} = \frac{mc^4}{r^2c^4/G} = \frac{c^2}{r}\frac{mc^2/r}{m_*c^2/r_*}$$
$$= \frac{c^2}{r}n_r = \frac{c^2}{rn_r}n_r^2 = \frac{2c^2}{r_s}n_r^2 \tag{6}$$

whose normalized graph $a/(2c^2/r_s)$ is plotted in the first figure.

2 Affine Connection

The conundrum posed by equation (1), that the acceleration of the test particle is independent of its mass m', is the principle motivation behind the general theory of relativity [3, p. 4]; an important ramification of which is that, in a free-falling local reference frame, the acceleration vanishes as in equation (7). That result leads to the following development. Given the two coordinate systems $x^\mu = x^\mu(\xi^\nu)$ and $\xi^\mu = \xi^\mu(x^\nu)$ and the differential equation

$$\frac{d^2\xi^\mu}{d\tau^2} = 0 \tag{7}$$

Fig. 1: The graph plots the normalized Newtonian acceleration $a/(2c^2/r_s)$ as a function of n_r ($0 \le n_r \le 1$).

applying the chain law to the differentials gives

$$\frac{d^2\xi^\mu}{d\tau^2} = \frac{\partial\xi^\mu}{\partial x^\nu}\frac{d^2x^\nu}{d\tau^2} + \frac{\partial^2\xi^\mu}{\partial x^\alpha \partial x^\nu}\frac{dx^\alpha}{d\tau}\frac{dx^\nu}{d\tau} = 0\,. \tag{8}$$

Then using

$$x^\alpha(\xi^\mu(x^\beta)) = x^\alpha \qquad \Longrightarrow \qquad \frac{\partial x^\beta}{\partial\xi^\mu}\frac{\partial\xi^\mu}{\partial x^\nu} = \delta^\beta_\nu \tag{9}$$

to eliminate the coefficient of $d^2x^\nu/d\tau^2$ in (8) leads to

$$\frac{d^2x^\beta}{d\tau^2} + \frac{\partial x^\beta}{\partial\xi^\mu}\frac{\partial^2\xi^\mu}{\partial x^\alpha\partial x^\nu}\frac{dx^\alpha}{d\tau}\frac{dx^\nu}{d\tau} = 0\,. \tag{10}$$

Rearranging indices in (10) finally yields

$$\frac{d^2x^\mu}{d\tau^2} + \Gamma^\mu_{\nu\rho}\frac{dx^\nu}{d\tau}\frac{dx^\rho}{d\tau} = \frac{du^\mu}{d\tau} + \Gamma^\mu_{\nu\rho}u^\nu u^\rho = 0 \tag{11}$$

where $u^\mu = dx^\mu/d\tau$ is a typical component of the test-mass 4-velocity and

$$\Gamma^\mu_{\nu\rho} \equiv \frac{\partial x^\mu}{\partial\xi^\alpha}\frac{\partial^2\xi^\alpha}{\partial x^\nu\partial x^\rho} \tag{12}$$

is the *affine connection*. The affine connection vanishes when there is no gravitational distortion; so for the point mass m, it should be solely a function of the curvature distortion n_r given by (4).

The affine connection can be related to the the metric coefficients $g_{\alpha\beta}$ via [3, p. 7]

$$\Gamma^\mu_{\nu\rho} = \frac{g^{\mu\alpha}}{2}\left[\frac{\partial g_{\rho\alpha}}{\partial x^\nu} + \frac{\partial g_{\nu\alpha}}{\partial x^\rho} - \frac{\partial g_{\nu\rho}}{\partial x^\alpha}\right] \tag{13}$$

which, for a metric with no cross terms ($g^{\alpha\beta} = 0$ for $\alpha \neq \beta$), reduces to

$$\frac{2\Gamma^1_{\nu\rho}}{g^{11}} = \frac{\partial g_{\rho 1}}{\partial x^\nu} + \frac{\partial g_{\nu 1}}{\partial x^\rho} - \frac{\partial g_{\nu\rho}}{\partial x^1} \tag{14}$$

with $\mu = 1$ for example.

Since only radial effects are of interest in the present paper, only the x^0 and x^1 components of the spherical polar coordinate system $(x^\mu) = (x^0, x^1, x^2, x^3) = (ct, r, \theta, \phi)$ are required. Then the affine connection in (11) for the $\mu = 1$ component reduces to

$$\frac{du^1}{d\tau} = -\Gamma^1_{\nu\rho}u^\nu u^\rho$$

$$= -\left[\Gamma^1_{00}(u^0)^2 + 2\Gamma^1_{01}u^0u^1 + \Gamma^1_{11}(u^1)^2\right] \tag{15}$$

which under static conditions ($u^1 = dr/d\tau = 0$ for the test mass) produces

$$\frac{du^1}{d\tau} = -\Gamma^1_{00}(u^0)^2\,. \tag{16}$$

In the spherical system with $d\theta = d\phi = 0$, the metric becomes

$$ds^2 = c^2d\tau^2 = g_{00}\,c^2dt^2 + g_{11}\,dr^2 \tag{17}$$

where g_{00} and g_{11} are functions of the coordinate radius $x^1 = r$. Under these conditions the only non-zero affine connections from (14) are:

$$\Gamma^0_{10} = \Gamma^0_{01} = \frac{g^{00}}{2}\frac{\partial g_{00}}{\partial x^1} \tag{18}$$

$$\Gamma^1_{00} = \frac{-g^{11}}{2}\frac{\partial g_{00}}{\partial x^1} \qquad \text{and} \qquad \Gamma^1_{11} = \frac{g^{11}}{2}\frac{\partial g_{11}}{\partial x^1}\,. \tag{19}$$

Using (17), the velocity u^0 can be calculated from

$$cd\tau = g_{00}^{1/2}dx^0\left[1 + \left(\frac{g_{11}}{g_{00}}\right)\left(\frac{dr/dt}{c}\right)^2\right]^{1/2} \tag{20}$$

which for static conditions ($dr/dt = 0$) leads to

$$u^0 = \frac{dx^0}{d\tau} = \frac{c}{g_{00}^{1/2}}\,. \tag{21}$$

Inserting (21) into (16) gives

$$\frac{du^1}{d\tau} = -\frac{c^2\Gamma^1_{00}}{g_{00}} = \frac{c^2}{g_{00}}\left(\frac{g^{11}}{2}\frac{\partial g_{00}}{\partial r}\right) \tag{22}$$

along with its covariant twin

$$\frac{du_1}{d\tau} = g_{11}\frac{du^1}{d\tau}$$

$$= \frac{g_{11}c^2}{g_{00}}\left(\frac{g^{11}}{2}\frac{\partial g_{00}}{\partial r}\right) = \frac{c^2}{g_{00}}\left(\frac{\partial g_{00}}{2\partial r}\right). \tag{23}$$

Then combining (22) and (23) leads to the static acceleration

$$\left|\frac{du^1}{d\tau}\frac{du_1}{d\tau}\right|^{1/2} = \left(-g^{11}\right)^{1/2}\left(\frac{c^2}{g_{00}}\right)\left(\frac{\partial g_{00}}{2\partial r}\right). \tag{24}$$

3 Static Acceleration

The metric coefficients g_{00} and g^{11} for a point mass m at $r = 0$ are given by (A6) and (A7) in the Appendix. After some straightforward manipulations, (24) leads to the (normalized) static gravitational acceleration ($0 \le n_r \le 1$)

$$\frac{a_n(n_r)}{2c^2/r_s} = \left|\frac{(du^1/d\tau)(du_1/d\tau)}{(2c^2/r_s)^2}\right|^{1/2}$$

$$= \frac{n_r^2}{(1 - r_s/R_n)^{1/2}(1 + 2^n n_r^n)^{2/n}} \tag{25}$$

$$= \frac{n_r^2}{[(1 + 2^n n_r^n)^{1/n} - 2n_r]^{1/2}(1 + 2^n n_r^n)^{3/2n}} \tag{26}$$

$$= \frac{n_r^2}{[(1 + 1/2^n n_r^n)^{1/n} - 1]^{1/2}(2n_r)^{1/2}(1 + 2^n n_r^n)^{3/2n}} \tag{27}$$

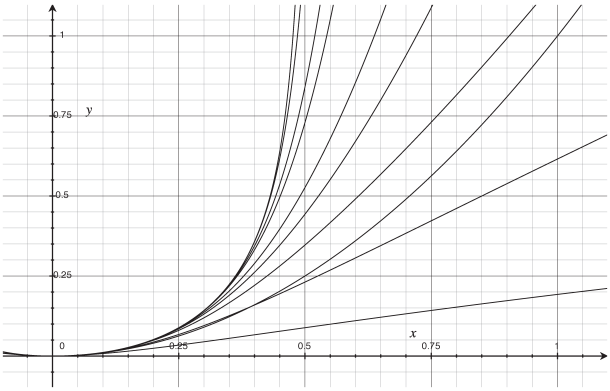

Fig. 2: The graph plots $a_n/(2c^2/r_s)$ as a function of n_r for the indices $n = 1, 2, 3, 4, 5, 8, 10, 20, 40$ from bottom-to-top of the graph. The curve that intersects (1,1) is the normalized Newtonian acceleration from (6). The $n = 3$ curve is the original Schwarzschild result [5] ($0 \le n_r \le 1$).

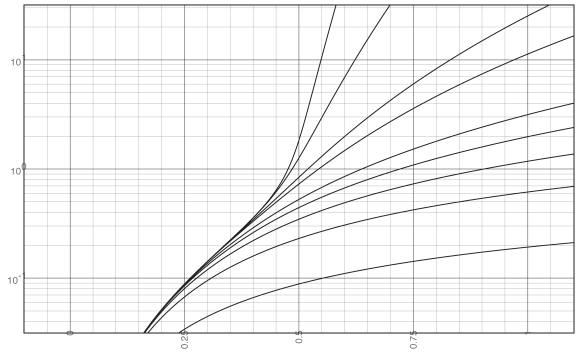

Fig. 3: The graph is a lin-log plot of $a_n/(2c^2/r_s)$ as a function of n_r for the indices $n = 1, 2, 3, 4, 5, 8, 10, 20, 40$ from bottom-to-top of the graph ($0 \le n_r \le 1$).

in terms of the relative curvature force n_r, all of which vanish for $n_r = 0$. Formally, the acceleration in the denominator on the left of (25)

$$\frac{\Delta v}{\Delta t} = \frac{c}{(r_s - r_s/2)/c} = \frac{2c^2}{r_s} \tag{28}$$

is the acceleration of a test mass starting from rest at $r = r_s$ ($n_r = 0.5$) and accelerating to the speed of light c in its fall to $r_s/2$ ($n_r = 1$) in the time interval $(r_s - r_s/2)/c$.

The limits of (26) and (27) as $n \to \infty$ are easily seen to be

$$\frac{a_\infty(n_r)}{2c^2/r_s} = \begin{cases} n_r^2/(1-2n_r)^{1/2} & , 0 \le n_r \le 0.5 \\ \infty & , 0.5 \le n_r \le 1 \end{cases} \tag{29}$$

where $n_r < 0.5$ and $n_r > 0.5$ are used in (26) and (27) respectively. Equations (26) and (27) are plotted in Figures 2 and 3 for various indices n, all plots of which are continuous in the entire range $0 \le n_r \le 1$. The curve that runs through the point (1,1) in Figure 2 is the Newtonian result from (6). It is clear from Figure 3 that the acceleration diverges in the range $0.5 \le n_r \le 1$ for the limit $n \to \infty$. In the range $0 \le n_r \le 0.5$ the acceleration is given by the upper equation in (29) — this result is identical with the static black-hole acceleration [3, p. 43].

4 Summary and Comments

The nature of the vacuum state provides a force constraint ($n_r \le 1$) on any theory of gravity, whether it's the Newtonian theory or the general theory of relativity [2]. This effect manifests itself rather markedly in the equation for the Kerr-Newman black-hole area A for a charged spinning mass [4]:

$$A = \frac{4\pi G}{c^4} \times \left[2m^2G - Q^2 + 2(m^4G^2 - c^2J^2 - m^2Q^2G)^{1/2}\right] \tag{30}$$

where Q and J are the charge and angular momentum of the mass m. Using the relation in (3) and $G = e_*^2/m_*^2$ [1], it is straightforward to transform (30) into the following equation

$$\begin{aligned} \frac{A}{4\pi r_*^2} = \; & 2\left(\frac{m}{m_*}\right)^2 - \left(\frac{Q}{e_*}\right)^2 + \\ & +2\left[\left(\frac{m}{m_*}\right)^4 - \left(\frac{J}{r_* m_* c}\right)^2 - \left(\frac{m}{m_*}\right)^2\left(\frac{Q}{e_*}\right)^2\right]^{1/2} \end{aligned} \tag{31}$$

where all of the parameters (e_*, m_*, r_*, except c of course) in the denominators of the terms are PV parameters; and all of the terms are properly normalized to the PV state, the area A by the area $4\pi r_*^2$, the angular momentum J by the angular momentum $r_* m_* c$, and so forth.

The "dogleg" in Figure (4) at the Schwarzschild radius r_s ($n_r = 0.5$) and the pseudo-singularity in the black-hole metric at r_s are features of the Einstein differential geometry approach to relativistic gravity — how realistic these features are remains to be seen. At this point in time, though, astrophysical measurements have not yet reached the $n_r = 0.5$ point (see below) where the dogleg and the black-hole results can be experimentally checked, but that point appears to be rapidly approaching. Whatever future measurements might show, however, the present calculations indicate that the point-mass-PV interaction that leads to n_r may point to the physical mechanism that underlies gravity phenomenology.

The evidence for black holes with all m/r ratios appears to be growing [3, Ch. 6]; so it is important to see if the present calculations can explain the experimental black-hole picture that is prevalent in today's astrophysics. The salient feature of a black hole is the event horizon [3, pp. 2, 152], that pseudo-surface at $r = r_s$ at which strange things are supposed to happen. A white dwarf of mass 9×10^{32}gm and radius 3×10^8cm exerts a curvature force on the PV equal to 2.7×10^{45}dyne, while a neutron star of mass 3×10^{33}gm and radius 1×10^6cm exerts a force of 2.7×10^{48}dyne [2]. Dividing these forces

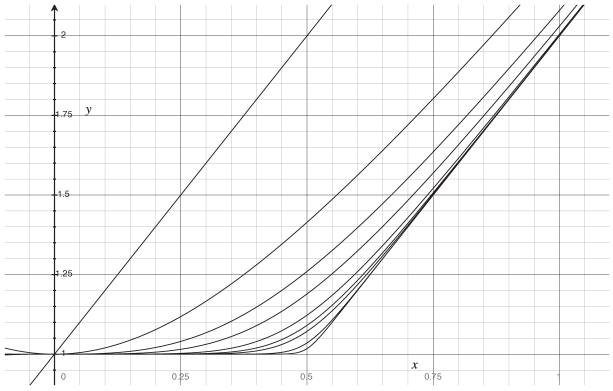

Fig. 4: The graph plots R_n/r as a function of n_r for the indices $n = 1, 2, 3, 4, 6, 8, 10, 20, 40$. The straight line is the $n = 1$ curve ($0 \leq n_r \leq 1$).

by the 1.21×10^{49}dyne force in the denominator of (4) leads to the n-ratios $n_r = 0.0002$ and $n_r = 0.2$ at the surface of the white dwarf and neutron star respectively. The surfaces of these two objects are real physical surfaces — thus they cannot be black holes.

On the other hand, SgrA* [3, p. 156] is thought to be a supermassive black-hole with a mass of about 4.2×10^6 solar masses and a radius confined to $r < 22 \times 10^{11}$ [cm], leading to the SgrA* n-ratio $n_r > 0.28$. For an n-ratio of 0.28, however, the plots in Figures 2–4 show that the behavior of spacetime and the PV is smooth. To reach the $n_r = 0.5$ value and the dogleg, the SgrA* radius would have to be about 12×10^{11} [cm], a result not significantly out of line with the measurements.

Finally, it should be noted that the black-hole formalism is the result of substituting $R_n = r$ in the metric (A1) of the Appendix. Unfortunately, since $R_n/r > 1$ signifies a response of the vacuum to the perturbation n_r at the coordinate radius r, the effect of this substitution is to eliminate that response. This is tantamount to setting $n_r = 0$ in the second-to-last expression of (A3).

Appendix: Crothers Vacuum Metrics

The general solution to the Einstein vacuum field [5] [6] for a point mass m at $r = 0$ consists of the infinite collection ($n = 1, 2, 3, \cdots$) of Schwarzschild-like metrics that are *non-singular* for all $r > 0$:

$$ds^2 = (1 - r_s/R_n)\, c^2 dt^2 - \frac{(r/R_n)^{2n-2}\, dr^2}{1 - r_s/R_n} - \\ -R_n^2(d\theta^2 + \sin^2\theta d\phi^2) \qquad \text{(A1)}$$

where

$$r_s = 2\,\frac{mG}{c^2} = 2\,\frac{mc^2}{m_* c^2/r_*} = 2rn_r \qquad \text{(A2)}$$

$$R_n = (r^n + r_s^n)^{1/n} = r(1 + 2^n n_r^n)^{1/n} = r_s \frac{(1 + 2^n n_r^n)^{1/n}}{2n_r} \qquad \text{(A3)}$$

and where r is the coordinate radius from the point mass to the field point of interest and r_s is the Schwarzschild radius. The ratio R_n/r as a function of n_r is plotted in Figure 4 for various indices n. The n-ratios 0, 0.5, and 1 correspond to the r values $r \to \infty$, r_s, and $r_s/2$ respectively.

All the metrics in (A1) for $n \geq 2$ reduce to

$$ds^2 = (1 - 2n_r)\, c^2 dt^2 - \frac{dr^2}{1 - 2n_r} - r^2(d\theta^2 + \sin^2\theta d\phi^2) \qquad \text{(A4)}$$

for $n_r \ll 1$.

It is clear from the expressions in (A3) that the requirement of asymptotic flatness [3, p.55] is fulfilled for all finite n. On the other hand, the proper radius $\mathcal{R}_n$ from the point mass at $r = 0$ to the coordinate radius r is not entirely calculable:

$$\mathcal{R}_n(r) = \int_0^r (-g_{11})^{1/2} dr$$

$$= \int_0^{r_s/2} (?)dr + \int_{r_s/2}^r (-g_{11})^{1/2} dr \qquad \text{(A5)}$$

due to the failure of the general theory in the region $0 < r < r_s/2$ [2].

The metric coefficients of interest in the text for $d\theta = d\phi = 0$ are

$$g_{00} = (1 - r_s/R_n) \qquad \text{(A6)}$$

$$g_{11} = -\frac{(r/R_n)^{2n-2}}{1 - r_s/R_n} = \frac{1}{g^{11}}\,. \qquad \text{(A7)}$$

From (A3)

$$\frac{\partial R_n}{\partial r} = \frac{1}{(1 + 2^n n_r^n)^{(1-1/n)}} \qquad \text{(A8)}$$

and from (A8)

$$\frac{\partial g_{00}}{\partial r} = \frac{r_s}{R_n^2}\frac{\partial R_n}{\partial r}\,. \qquad \text{(A9)}$$

Submitted on May 3, 2012 / Accepted on May 11, 2012

References

1. Daywitt W.C. The Planck vacuum. *Progress in Physics*, 2009, v. 1, 20–26.
2. Daywitt W.C. Limits to the validity of the Einstein field equations and general relativity from the viewpoint of the negative-energy Planck vacuum state. *Progress in Physics*, 2009, v. 3, 27–29.
3. Raine D., Thomas E. *Black Holes: An Introduction*. Second Edition, Imperial College Press, London, 2010. The reader should note that m is used in the present paper to denote physical mass — it is not the geometric mass $m\,(\equiv MG/c^2)$ as used in this reference.
4. http://www.phy.olemiss.edu/~luca/Topics/bh/laws.html
5. Crothers S.J. On the general solution to Einstein's vacuum field and its implications for relativistic degeneracy. *Progress in Physics*, 2005, v. 1, 68–73.
6. Daywitt W.C. The Planck vacuum and the Schwarzschild metrics. *Progress in Physics*, 2009, v. 3, 30–31.

Cumulative-Phase-Alteration of Galactic-Light Passing Through the Cosmic-Microwave-Background: A New Mechanism for Some Observed Spectral-Shifts

Hasmukh K. Tank

Indian Space Research Organization, 22/693, Krishna Dham-2, Vejalpur, Ahmedabad-380015, India
E-mail: tank.hasmukh@rediffmail.com, hasmukh.tank1@gmail.com

Currently, whole of the measured "cosmological-red-shift" is interpreted as due to the "metric-expansion-of-space"; so for the required "closer-density" of the universe, we need twenty times more mass-energy than the visible baryonic-matter contained in the universe. This paper proposes a new mechanism, which can account for good percentage of the red-shift in the extra-galactic-light, greatly reducing the requirement of dark matter-energy. Also, this mechanism can cause a new kind of blue-shift reported here, and their observational evidences. These spectral-shifts are proposed to result due to cumulative phase-alteration of extra-galactic-light because of vector-addition of: (i) electric-field of extra-galactic-light and (ii) that of the cosmic-microwave-background (CMB). Since the center-frequency of CMB is much lower than extra-galactic-light, the cumulative-phase-alteration results in *red*-shift, observed as an additional contributor to the measured "cosmological red-shift"; and since the center-frequency of CMB is higher than the radio-frequency-signals used to measure velocity of space-probes like: Pioneer-10, Pioneer-11, Galileo and Ulysses, the cumulative-phase-alteration resulted in blue-shift, leading to the interpretation of deceleration of these space-probes. While the galactic-light experiences the red-shift, and the ranging-signals of the space-probes experience *blue*-shift, they are comparable in magnitude, providing a supportive-evidence for the new mechanism proposed here. More confirmative-experiments for this new mechanism are also proposed.

1 Introduction

Currently, whole of the "cosmological red-shift" is interpreted in terms of "metric-expansion-of-space", so for the required "closer-density" of the universe, we need twenty times more mass-energy than the visible baryonic-matter contained in the universe. This paper proposes a new mechanism, which can account for good percentage of the red-shift in the extra-galactic-light, greatly reducing the requirement of dark matter-energy. Prior to this, many scientists had proposed alternative-interpretations of "the cosmological red-shift", but the alternatives proposed so far were rather speculative; for example, speculating about possible presence of iron-particles in the inter-galactic-space, or presence of atoms of gas, or electrons, or virtual-particles... etc. How can we say for sure that such particles are indeed there in the inter-galactic-space? Even if they are there, is the "cross-section" of their interactions sufficient? Whereas a mechanism proposed here is based on experimentally established facts, namely the presence of "cosmic-microwave-background" (CMB), we are sure that CMB is indeed present in the inter-galactic-space. And we know for sure that electric-field-vectors of light and CMB are sure to get added.

This mechanism predicts both kids of spectral-shifts, *red*-shift as well as *blue*-shift. The solar-system-astrometric-anomalies [1, 2] are indicated here to arise due to the *blue*-shift caused by the cumulative-phase-alteration-mechanism proposed here. These anomalies are actually providing supportive-evidences for the new mechanism proposed here.

Brief reminder of the "solar system astrometric anomalies" will be in order here: (a) Anomalous secular increase of the eccentricity of the orbit of the moon [3–7] (b) the fly-by-anomaly [8–10] (c) precession of Saturn [11–12], (d) secular variation of the gravitational-parameter GM (i.e. G times mass M of the Sun) [13–16] (e) secular variation of the Astronomical-Unit [17–23] and (f) the Pioneer anomaly. For description of Pioneers see: [24] for general review of Pioneer-anomaly see: [25]. Of course, the traditional constant part of the anomalous-acceleration does not show up in the motion of major bodies of the solar system [26–44]. For the attempts of finding explanations for the Pioneer-anomaly in terms of conventional physics see: [45–52].

In this new mechanism for the spectral-shift, proposed here, there is no loss of energy; energy lost by cosmic-photons get transferred to CMB; so, it is in agreement with the law of conservation of energy. More verification-experiments for this new mechanism are also proposed here, so it is a testable proposal.

Moreover, this proposal is not in conflict with the existing theories, because it does not claim that whole of the measured "cosmological red-shift" is due to this "cumulative-phase-alteration-mechanism"; some 5% of the red-shift must be really due to "metric-expansion-of-space", reducing requirement of total-mass-of-the-universe to the observable

baryonic matter, making it sufficient for the required "closer-density". Thus this new mechanism is likely to resolve many of the problems of the current Standard Model of Cosmology.

2 Cumulative phase-alteration of the Extra-Galactic-Light passing through the Cosmic-Microwave-Background (CMB)

Let us imagine a horizontal arrow of three centimeter length representing instantaneous magnitude and direction of electric-field of the "extra-galactic-light". Then add a small arrow of just five mm length at an angle minus thirty degrees, representing instantaneous magnitude and direction of the "cosmic-microwave-background". We can see that the resultant vector has increased in magnitude, but lagged behind by a small angle theta. As the wave of extra-galactic-light travels in space, a new arrow representing CMB keeps on getting added to the previous resultant-vector. This kind of phase and amplitude-alterations continue for billions of years in the case of "extra-galactic-light"; producing a cumulative-effect. Since the speed of rotation of the vector representing CMB is much slower than that of light, the CMB-vector pulls-back the Light-vector resulting in reduction of cyclic-rotations. This process can be mathematically expressed as follows:

Electric field of pure light-wave can be expressed as:

$$\Psi(X,t) = A\exp i(\omega t - kX)$$

where ω represents the angular-frequency of light, and k the wave-number. Taking into consideration only the time-varying-part, at a point p :

$$\Psi(t) = A\left[\cos\omega t + i\sin\omega t\right] \tag{1}$$

When electric-fields of CMB get added to light, the resultant-sum can be expressed as:

$$\Psi(t) = A\left[N(t)\cos\omega t + i\hat{N}(t)\sin\omega t\right] \tag{2}$$

Where: $N(t)$ represents instantaneous magnitude of alteration caused by CMB, and $\hat{N}(t)$ represents its Hilbert-transform. When all the spectral-components of $N(t)$ are phase-shifted by +90 degrees, we get its Hilbert-transform $\hat{N}(t)$.

As a communications-engineer we use band-pass-filter to remove out-of-band noise. This author has also developed a noise-cancelling-technique, to reduce the effect of even in-band-noise by up-to 10 dB. But in the extra-galactic-space there are no band-pass-filters, so the phase-alterations caused by CMB keep on getting accumulated. After billions of years, when this light reaches our planet earth there is a cumulative-phase-alteration in the extra-galactic-light, observed as a part of "the cosmological red-shift". Since the center-frequency of CMB is much lower than extra-galactic-light, the cumulative-phase-alteration results in red-shift; and since the center-frequency of CMB is higher than the radio-frequency-signals (2110 MHz for the uplink from Earth and 2292 MHz for the downlink to Earth) used to measure velocity of Pioneer-10, Pioneer-11, Galileo and Ulysses space-probes, the cumulative-phase-alteration resulted in blue-shift, leading to the interpretation of deceleration of these space-probes. C. Johan Masreliez [53] has presented a "cosmological explanation for the Pioneer-anomaly", in terms of expansion of space, whereas here it is proposed that the expansion-of-space appears mostly due to the "cumulative-phase-alteration" of light due to CMB. This shows that there is a co-relation between the magnitudes of anomalous-accelerations of the Pioneer-10-11 space-probes and the "cosmological red-shift". Although, one of the shifts is red-shift, and the other is *blue*-shift, their magnitudes, in terms of decelerations, are strikingly the same; as described in detail in the next paragraph:

We can express the cosmological red-shift z_c in terms of de-acceleration experienced by the photon, as follows [54–55]: For z_c smaller than one:

$$z_c = \frac{f_0 - f}{f} = \frac{H_0 D}{c}$$

i.e.

$$\frac{h\Delta f}{hf} = \frac{H_0 D}{c}$$

i.e.

$$h\Delta f = \frac{hf}{c^2}(H_0 c)D \tag{3}$$

That is, the loss in energy of the photon is equal to its mass (hf/c^2) times the acceleration $a = H_0 c$, times the distance D travelled by it. Where: H_0 is Hubble-parameter. And the value of constant acceleration a is:

$$a = H_0 c, \quad a = 6.87\times10^{-10}\ \ m/s^2.$$

And now, we will see that the accelerations experienced by the Pioneer-10, Pioneer-11, Galileo and Ulysses space-probes do match strikingly with the expression (3):

Carefully observed values of de-accelerations [27]:
For Pioneer-10:
$a = (8.09\pm0.2)\times10^{-10}\ \ m/s^2 = H_0 c \pm$ local-effect.
For Pioneer-11:
$a = (8.56\pm0.15)\times10^{-10}\ \ m/s^2 = H_0 c \pm$ local-effect.
For Ulysses:
$a = (12\pm3)\times10^{-10}\ \ m/s^2 = H_0 c \pm$ local-effect.
For Galileo:
$a = (8\pm3)\times10^{-10}\ \ m/s^2 = H_0 c \pm$ local-effect.
And: as we already derived earlier, for the "cosmologically-red-shifted-photon", $a = 6.87\times10^{-10}\ \ m/s^2 = H_0 c$.
The "critical acceleration" of modified Newtonian dynamics MOND: $a_0 = H_0 c$. The rate of "accelerated-expansion" of the universe: $a_{exp} = H_0 c$.

Perfect matching of values of decelerations of all the four space-probes is itself an interesting observation; and its matching with the deceleration of cosmologically-red-

shifting-photons can not be ignored by a scientific mind as a coincidence.

There is one more interesting thing about the value of this deceleration as first noticed by Milgrom, that: with this value of deceleration, an object moving with the speed of light would come to rest exactly after the time T_0 which is the age of the universe.

The attempt proposed by this author refers only to the constant part of the PA. It should be acknowledged that also a time-varying part has been discovered as well.

3 Possible verification-experiments

Vector-addition of light and CMB can be simulated using computers. The vector to be added to light-vector can be derived from the actual CMB received. Every time new and new CMB-vector can be added to the resultant vector of previous addition.

Secondly, we know that there is certain amount of unisotropy in the CMB. Microwaves coming from some directions are more powerful than others. So, we can look for any co-relation between the strength of CMB from a given direction and value of cosmological-red-shift.

Thirdly, we can establish a reverberating-satellite-link, in which we can first transmit a highly-stable frequency to geo-synchronous-satellite; receive the signal back; re-transmit the CMB-noise-corrupted-signal back to satellite, and continue such repetitions for an year or longer and compare the frequency of the signal with the original source.

4 Conclusion

After getting the results of verification-experiments, the new mechanism proposed here namely: "Cumulative Phase-Alteration of the Extra-Galactic-Light passing through Cosmic-Microwave-Background (CMB)" it seems possible to explain: not only the large percentage of "cosmological red-shift", but also the Pioneer-anomaly. Quantitative analysis may leave 5% of the measured value of the "cosmological red-shift" for the standard explanation in terms of "metric-expansion-of-space", reducing the requirement of total-mass of the universe to the already-observable baryonic matter; thus it is likely to resolve many of the problems of current standard-model-cosmology. This author also proposes to investigate if this new mechanism of spectral-shifts will be able to accommodate some of the solar-system-astrometric-anomalies.

Submitted on: June 14, 2012 / Accepted on: June 15, 2012

References

1. Lämmerzahl C., Preuss O., and Dittus H. "Is the physics within the solar system really understood?" in Lasers, Clocks and Drag Free Control: Exploration of Relativistic Gravity in Space, Dittus H., Lämmerzahl C., and Turyshev S.G., Eds., pp.75–104, Springer, Berlin, Germany, 2008.
2. Anderson J.D., Nieto M.M., 2010, in Klioner S.A., Seidelmann P.K., Soffel M.H., eds, Proc. IAU Symp. 261, Relativity in Fundamental Astronomy: Dynamics, Reference Frames, and Data Analysis. Cambridge Univ. Press, Cambridge, p. 189.
3. Williams J.G., Boggs D.H., Yoder C.F., Ratcliff J.T., Dickey J.O. Lunar rotational dissipation in solid body and molten core. *Journal of Geophysical Research – Planets*, 2001, v. 106, 27933–27968.
4. Williams J.G., Dickey J.O., 2003, in Noomen R., Klosko S., Noll C., Pearlman M., eds, Proc. 13th Int. Workshop Laser Ranging, NASA/CP-2003-212248, Lunar Geophysics, Geodesy, and Dynamics, p.75. `http://cddis.nasa.gov/lw13/docs/papers/sci_williams_1m.pdf`
5. Williams J.G., Boggs D.H., 2009, in Schilliak S., ed., Proc. 16th Int. Workshop Laser Ranging, Lunar Core Mantle. What Does LLR See? p. 101. `http://cddis.gsfc.nasa.gov/lw16/docs/papers/sci_1` (read p. 115–116 where it is written: "While the mean motion and semimajor axis rates are compatible with our understanding of dissipation in Earth and Moon, LLR solutions consistently find an anomalous eccentricity rate").
6. Iorio L. On the anomalous secular increase of the eccentricity of the orbit of the Moon. *Monthly Notices of the Royal Astronomical Society*, 211, v. 415, 1266–1275.
7. Iorio L. An empirical explanation of the anomalous increase in the astronomical unit and the lunar eccentricity. *Astronomical Journal*, 2011, v. 142, 68–70.
8. Anderson J.D., Campbell J.K., and Nieto M.M. The energy transfer process in planetary flybys. *New Astronomy*, 2007, v. 12, no. 5, 383–397.
9. Anderson J.D., Campbell J.K., Ekelund J.E., Ellis J., and Jordan J.F. Anomalous orbital-energy changes observed during spacecraft flybys of earth. *Physical Review Letters*, 2008, v. 100, no. 9, 091102.
10. Iorio L. The Effect of General Relativity on Hyperbolic Orbits and Its Application to the Flyby Anomaly. *Scholarly Research Exchange*, 2009, Article ID: 807695.
11. Pitjeva, E.V.: EPM ephemerides and relativity. In: Klioner, S.A., Seidelmann, P.K., Soffel, M.H., (Eds.) IAU Symposium, Vol. 261 of IAU Symposium, pp. 170–178, (2010).
12. Fienga A., Laskar J., Kuchynka P., Manche H., Desvignes G., Gastineau M., Cognard I., Theureau G. The INPOP10 a planetary ephemeris and its applications in fundamental physics. *Celestial Mechanics and Dynamical Astronomy*, 2011, v. 111, no. 3, 363–385.
13. Pitjeva E.V., Pitjev N.P. Estimations of changes of the Sun's mass and the gravitation constant from the modern observations of planets and spacecraft. *Solar System Research*, 2012, v. 46(1), 78–87.
14. Iorio L. Classical and Relativistic OrbitalMotions around a Mass-Varying Body. *Scholarly Research Exchange Physics*, 2010, Article ID: 261249.
15. Iorio L. Orbital effects of Suns mass loss and the Earths fate. *Natural Science*, 2010, v. 2(4), 329–337.
16. Iorio L. Effect of sun and planet-bound dark matter on planet and satellite dynamics in the solar system. *Journal of Cosmology and Astroparticle Physics*, 2010, v. 05, 018.
17. Krasinsky G.A., Brumberg V.A. Secular increase of astronomical unit from analysis of the major planet motions, and its interpretation. *Celestial Mechanics and Dynamical Astronomy* 2004, v. 90, 267–288.
18. Standish E.M. The Astronomical Unit Now, in Transit of Venus: new views of the solar system and galaxy, IAU Coll. 196, Kurtz D.W., Cambridge: Cambridge University Press, 2005, pp. 163–179.
19. Iorio L. Secular increase of the astronomical unit and perihelion precessions as tests of the Dvali Gabadadze Porrati multidimensional braneworld scenario. *Journal of Cosmology and Astroparticle Physics*, 2011, v. 09, 006.

20. Arakida H. Application of time transfer function to McVittie spacetime: gravitational time delay and secular increase in astronomical unit. *General Relativity and Gravitation*, 2011, v. 43(8), 2127–2139.
21. Arakida H. Time delay in Robertson McVittie space-time and its application to increase of astronomical unit. *New Astronomy*, 2009, v. 14(3), 264–268.
22. Ito Y. *Publications of the Astronomical Society of Japan*, 2009, v. 61, 1373.
23. Miura T., Arakida H., Kasai M., and Kuramata S. *Publications of the Astronomical Society of Japan*, 2009, v. 61, 1247.
24. W. J. Dixon, Pioneer spacecraft reliability and performance. *Acta Astronautica*, 1975, v. 2(9–10), pp. 801–817.
25. Turyshev S.G., Toth V.T. The Pioneer Anomaly. *Living Reviews in Relativity*, 2010, v. 13, Article ID: 4.
26. Anderson J.D., Laing P.A., Lau E.L., Liu A.S., Nieto M.M., and Turyshev, S.G. Indication, from Pioneer 10, 11, Galileo, and Ulysses Data, of an Apparent Anomalous, Weak, Long-Range Acceleration. *Physical Review Letters*, 1998, v. 81, 2858–2861 [(Comment by Katz J.I.: Phys. Rev. Lett. Vol. 83, 1892 (1999); Reply: Phys. Rev. Lett. 83, 1893 (1999)].
27. Turyshev S.G., Toth V.T., Ellis J., Markwardt C.B. Support for Temporally Varying Behavior of the Pioneer Anomaly from the Extended Pioneer 10 and 11 Doppler Data Sets, *Physical Review Letters*, 2011, v. 107, no. 8, 081103.
28. Standish E.M. "Planetary and Lunar Ephemerides: testing alternate gravitational theories", in Recent Developments in Gravitation and Cosmology, A. Macias, C. Lämmerzahl, and A. Camacho, Eds., v. 977 of AIP Conference Proceedings, pp. 254–263, American Institute of Physics, Melville, NJ, USA, 2008.
29. Standish E.M. "Testing alternate gravitational theories", in Fundamental Astronomy: Dynamics, Reference Frames, and Data Analysis, Proceedings of the International Astronomical Union, S. A.
30. Klioner P., Seidelmann K., and Soffel M.H., Eds., v. 261 of IAU Symposium, pp. 179–182, 2010.
31. Iorio L. and Giudice G. What do the orbital motions of the outer planets of the Solar System tell us about the Pioneer anomaly? *New Astronomy*, 2006, v. 11, no. 8, 600–607.
32. Page G.L., Dixon D.S., and Wallin J.F. Can minor planets be used to assess gravity in the outer solar system? *Astrophysical Journal*, 2006, v. 642, no. 1, 606–614.
33. Tangen K. Could the Pioneer anomaly have a gravitational origin? *Physical Review D*, 2007, v. 76, no. 4, 042005.
34. Iorio L. Can the pioneer anomaly be of gravitational origin? A phenomenological answer. *Foundations of Physics*, 2007, v. 37, no. 6, 897–918.
35. Iorio L. Jupiter, Saturn and the Pioneer anomaly: a planetary-based independent test. *Journal of Gravitational Physics*, 2007, v. 1, no. 1, 5–8.
36. Wallin J.F., Dixon D.S., and Page G.L. Testing gravity in the outer solar system: results from trans-neptunian objects. *Astrophysical Journal*, 2007, v. 666, no. 2, 1296–1302.
37. Iorio L. "The Lense-Thirring effect and the Pioneer anomaly: solar system tests", in Proceedings of the the 11th Marcel Grossmann Meeting on Recent Developments in Theoretical and Experimental General Relativity, Gravitation and Relativistic Field Theorie, H. Kleinert, R.T. Jantzen, and R. Ruffini, Eds., pp. 2558–2560, World Scientific, 2008.
38. Fienga A., Laskar J., Kuchynka P., Leponcin-Lafitte C., Manche1 H., and Gastineau M., "Gravity tests with INPOP planetary ephemerides", in Relativity in Fundamental Astronomy, S.A. Klioner, P.K. Seidelman, and M.H. Soffel, Eds., Proceedings IAU Symposium no. 261, pp. 159–169, 2010.
39. Page G.L., Wallin J.F., and Dixon D.S. How well do we know the orbits of the outer planets? *Astrophysical Journal*, 2009, v. 697, no. 2, 1226–1241.
40. Iorio L. Does the Neptunian system of satellites challenge a gravitational origin for the Pioneer anomaly. *Monthly Notices of the Royal Astronomical Society*, 2010, v. 405, no. 4, 2615–2622.
41. Page G.L., Wallin J.F., and Dixon D.S. How well do we know the orbits of the outer planets? *Astrophysical Journal*, 2009, v. 697, no. 2, 1226–1241.
42. Iorio L. Does the Neptunian system of satellites challenge a gravitational origin for the Pioneer anomaly? *Monthly Notices of the Royal Astronomical Society*, 2010, v. 405, no. 4, 2615–2622.
43. Page G.L. Exploring the weak limit of gravity at solar system scales. *Publications of the Astronomical Society of the Pacific*, 2010, v. 122, no. 888, 259–260.
44. Iorio L. Orbital effects of the time-dependent component of the Pioneer anomaly. *Modern Physics Letters A*, 2012, v. 27, no. 12, 1250071.
45. Bertolami O., Francisco F., Gil P.J.S., and Paramos J. Thermal analysis of the Pioneer anomaly: a method to estimate radiative momentum transfer. *Physical Review D*, 2008, v. 78, no. 10, 103001.
46. Rievers B., Lämmerzahl C., List M., Bremer S., and Dittus H. New powerful thermal modelling for high-precision gravity missions with application to Pioneer 10/11. *New Journal of Physics*, 2009, v. 11, 113032.
47. Bertolami O., Francisco F., Gil P.J.S., and Paramos J. Estimating radiative momentum transfer through a thermal analysis of the pioneer anomaly. *Space Science Reviews*, 2010, v. 151, no. 1–3, 75–91.
48. Rievers B., Bremer S., List M., Lämmerzahl C., and Dittus H. Thermal dissipation force modeling with preliminary results for Pioneer 10/11. *Acta Astronautica*, 2010, v. 66, no. 3–4, 467–476.
49. Rievers B., Lämmerzahl C., and Dittus H. Modeling of thermal perturbations using raytracing method with preliminary results for a test case model of the pioneer 10/11 radioisotopic thermal generators. *Space Science Reviews*, 2010, v. 151, no. 1–3, 123–133.
50. Rievers B., Lämmerzahl C. High precision thermal modeling of complex systems with application to the flyby and Pioneer anomaly. *Annalen der Physik*, 2011, v. 523, no. 6, 439–449.
51. Francisco F., Bertolami O., Gil P.J.S., and Paramos J. Modelling the reflective thermal contribution to the acceleration of the Pioneer spacecraft. *Physics Letters B*, at press, 2012, `http://arxiv.org/abs/1103.5222`.
52. Turyshev S.G., Toth V.T., Kinsella G.L., Siu-Chun L., Shing M., Ellis J. Support for the thermal origin of the Pioneer anomaly. *Physical Review Letters*, 2012, at press, `http://arxiv.org/abs/1204.2507`.
53. Masreliez C.J. A Cosmological Explanation to the Pioneer Anomaly. *Astrophysics and Space Science*, 2005, v. 299, no. 1, 83–108.
54. Tank H.K. A new law emerging from the recurrences of the "critical-acceleration" of MOND, suggesting a clue to unification of fundamental forces. *Astrophysics and Space Science*, 2010, v. 330, 203–205.
55. Tank H.K. Some clues to understand MOND and the accelerated expansion of the universe. *Astrophysics and Space Science*, 2011, v. 336, no. 2, 341–343.

One-Way Speed of Light Measurements Without Clock Synchronisation

Reginald T. Cahill
School of Chemical and Physical Sciences, Flinders University, Adelaide 5001, Australia
E-mail: Reg.Cahill@flinders.edu.au

The 1991 DeWitte double one-way 1st order in v/c experiment successfully measured the anisotropy of the speed of light using clocks at each end of the RF coaxial cables. However Spavieri *et al.*, Physics Letters A (2012), have reported that (i) clock effects caused by clock transport should be included, and (ii) that this additional effect cancels the one-way light speed timing effect, implying that one-way light speed experiments "do not actually lead to the measurement of the one-way speed of light or determination of the absolute velocity of the preferred frame". Here we explain that the Spavieri *et al.* derivation makes an assumption that is not always valid: that the propagation is subject to the usual Fresnel drag effect, which is not the case for RF coaxial cables. As well DeWitte did take account of the clock transport effect. The Spavieri *et al.* paper has prompted a clarification of these issues.

1 Introduction

The enormously significant 1991 DeWitte [1] double one-way 1st order in v/c experiment successfully measured the anisotropy of the speed of light using clocks at each end of the RF coaxial cables. The technique uses rotation of the light path to permit extraction of the light speed anisotropy, despite the clocks not being synchronised. Data from this 1st order in v/c experiment agrees with the speed and direction of the anisotropy results from 2nd order in v/c Michelson gas-mode interferometer experiments by Michelson and Morley and by Miller, see data in [2], and with NASA spacecraft earth-flyby Doppler shift data [3], and also with more recent 1st order in v/c experiments using a new single clock technique [2], Sect. 5. However Spavieri *et al.* [4] reported that (i) clock effects caused by clock transport should be included, and (ii) that this additional effect cancels the one-way light speed timing effect, implying that one-way light speed experiments "do not actually lead to the measurement of the one-way speed of light or determination of the absolute velocity of the preferred frame". Here we explain that the Spavieri *et al.* derivation makes an assumption that is not always valid: that the propagation is subject to the usual Fresnel drag effect, which is not the case for RF coaxial cables. The Spavieri *et al.* paper has prompted a clarification of these issues. In particular DeWitte took account of both the clock transport effect, and also that the RF coaxial cables did not exhibit a Fresnel drag, though these aspects were not discussed in [1].

2 First Order in v/c Speed of EMR Experiments

Fig. 1 shows the arrangement for measuring the one-way speed of light, either in vacuum, a dielectric, or RF coaxial cable. It is usually argued that one-way speed of light measurements are not possible because the clocks C_1 and C_2 cannot be synchronised. However this is false, although an important previously neglected effect that needs to be included is the clock offset effect caused by transport when the apparatus is rotated [4], but most significantly the Fresnel drag effect is not present in RF coaxial cables. In Fig. 1 the actual travel time $t_{AB} = t_B - t_A$ from A to B, as distinct from the clock indicated travel time $T_{AB} = T_B - T_A$, is determined by

$$V(v\cos(\theta))t_{AB} = L + v\cos(\theta)t_{AB} \qquad (1)$$

where the 2nd term comes from the end B moving an additional distance $v\cos(\theta)t_{AB}$ during time interval t_{AB}. With Fresnel drag $V(v) = \frac{c}{n} + v\left(1 - \frac{1}{n^2}\right)$, when V and v are parallel, and where n is the dielectric refractive index. Then

$$t_{AB} = \frac{L}{V(v\cos(\theta)) - v\cos(\theta)} = \frac{nL}{c} + \frac{v\cos(\theta)L}{c^2} + .. \qquad (2)$$

However if there is no Fresnel drag effect, $V = c/n$, as is the case in RF coaxial cables, then we obtain

$$t_{AB} = \frac{L}{V(v\cos(\theta)) - v\cos(\theta)} = \frac{nL}{c} + \frac{v\cos(\theta)Ln^2}{c^2} + .. \qquad (3)$$

It would appear that the two terms in (2) or (3) can be separated by rotating the apparatus, giving the magnitude and direction of $\mathbf{v}$. However it is $T_{AB} = T_B - T_A$ that is measured, and not t_{AB}, because of an unknown fixed clock offset τ, as the clocks are not *a priori* synchronised, and as well an angle dependent clock transport offset $\Delta\tau$, at least until we can establish clock synchronisation, as explained below. Then the clock readings are $T_A = t_A$ and $T_B = t_B + \tau$, and $T'_B = t'_B + \tau + \Delta\tau$, where $\Delta\tau$ is a clock offset that arises from the slowing of clock C_2 as it is transported during the rotation through angle $\Delta\theta$, see Fig. 1.

3 Clock Transport Effect

The clock transport offset $\Delta\tau$ follows from the clock motion effect

$$\Delta\tau = dt\sqrt{1 - \frac{(\mathbf{v}+\mathbf{u})^2}{c^2}} - dt\sqrt{1 - \frac{\mathbf{v}^2}{c^2}} = -dt\frac{\mathbf{v}\cdot\mathbf{u}}{c^2} + ..., \qquad (4)$$

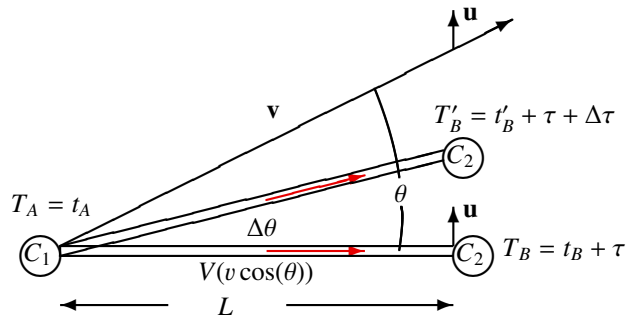

Fig. 1: Schematic layout for measuring the one-way speed of light in either free-space, optical fibres or RF coaxial cables, without requiring the synchronisation of the clocks C_1 and C_2. Here τ is the, initially unknown, offset time between the clocks. Times t_A and t_B are true times, without clock offset and clock transport effects, while $T_A = t_A$, $T_B = t_A + \tau$ and $T'_B = t'_B + \tau + \Delta\tau$ are clock readings. $V(v\cos(\theta))$ is the speed of EM radiation wrt the apparatus before rotation, and $V(v\cos(\theta - \Delta\theta))$ after rotation, $\mathbf{v}$ is the velocity of the apparatus through space in direction θ relative to the apparatus before rotation, $\mathbf{u}$ is the velocity of transport for clock C_2, and $\Delta\tau < 0$ is the net slowing of clock C_2 from clock transport, when apparatus is rotated through angle $\Delta\theta > 0$. Note that $\mathbf{v} \cdot \mathbf{u} > 0$.

when clock C_2 is transported at velocity $\mathbf{u}$ over time interval dt, compared to C_1. Now $\mathbf{v} \cdot \mathbf{u} = vu\sin(\theta)$ and $dt = L\Delta\theta/u$. Then the change in T_{AB} from this small rotation is, using (3) for the case of no Fresnel drag,

$$\Delta T_{AB} = \frac{v\sin(\theta)Ln^2\Delta\theta}{c^2} - \frac{v\sin(\theta)L\Delta\theta}{c^2} + ... \qquad (5)$$

as the clock transport effect appears to make the clock-determined travel time smaller (2nd term). Integrating we get

$$T_B - T_A = \frac{nL}{c} + \frac{v\cos(\theta)L(n^2-1)}{c^2} + \tau, \qquad (6)$$

where τ is now the constant offset time. The $v\cos(\theta)$ term may be separated by means of the angle dependence. Then the value of τ may be determined, and the clocks synchronised. However if the propagation medium is vacuum, liquid, or dielectrics such as glass and optical fibres, the Fresnel drag effect is present, and we then use (2), and not (3). Then in (6) we need make the replacement $n \to 1$, and then the 1st order in v/c term vanishes, as reported by Spavieri *et al.*. However, in principle, separated clocks may be synchronised by using RF coaxial cables.

4 DeWitte 1st Order in v/c Detector

The DeWitte $L = 1.5$ km 5 MHz RF coaxial cable experiment, Brussels 1991, was a double 1st order in v/c detector, using the scheme in Fig. 1, but employing a 2nd RF coaxial cable for the opposite direction, giving clock difference $T_D - T_C$, to cancel temperature effects, and also used 3 Caesium atomic clocks at each end. The orientation was NS and

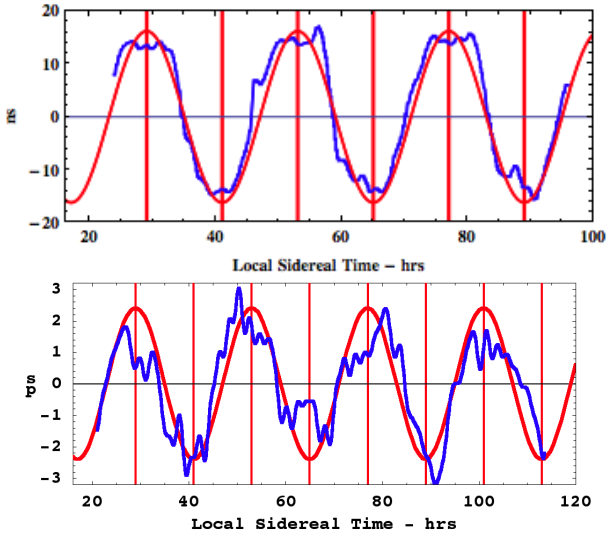

Fig. 2: Top: Data from the 1991 DeWitte NS RF coaxial cable experiment, $L = 1.5$ km, using the arrangement shown in Fig. 1, with a 2nd RF coaxial cable carrying a signal in the reverse direction. The vertical red lines are at RA=5^h and 17^h. DeWitte gathered data for 178 days, and showed that the crossing time tracked sidereal time, and not local solar time, see Fig. 3. DeWitte reported that $v \approx 500$ km/s. If a Fresnel drag effect is included no effect would have been seen. Bottom: Dual coaxial cable detector data from May 2009 using the technique in Fig. 4 with $L = 20$ m. NASA Spacecraft Doppler shift data predicts Dec= $-77°$, $v = 480$ km/s, giving a sidereal dynamic range of 5.06 ps, very close to that observed. The vertical red lines are at RA=5^h and 17^h. In both data sets we see the earth sidereal rotation effect together with significant wave/turbulence effects.

rotation was achieved by that of the earth [1]. Then

$$T_{AB} - T_{CD} = \frac{2v\cos(\theta)L(n^2-1)}{c^2} + 2\tau \qquad (7)$$

For a horizontal detector the dynamic range of $\cos(\theta)$ is $2\sin(\lambda)\cos(\delta)$, caused by the earth rotation, where λ is the latitude of the detector location and δ is the declination of $\mathbf{v}$. The value of τ may be determined and the clocks synchronised. Some of DeWitte's data and results are in Figs. 2 and 3. DeWitte noted that his detector produced no effect at RF frequency of 1GHz, suggesting that the absence of Fresnel drag in RF coaxial cables may be a low frequency effect. This means that we should write the Fresnel drag expression as $V(v) = \frac{c}{n} + v\left(1 - \frac{1}{m(f)^2}\right)$, where $m(f)$ is RF frequency f dependent, with $m(f) \to n$ at high f.

5 Dual RF Coaxial Cable Detector

The single clock Dual RF Coaxial Cable Detector exploits the absence of the Fresnel drag effect in RF coaxial cables [2]. Then from (3) the round trip travel time for one circuit is, see Fig. 4,

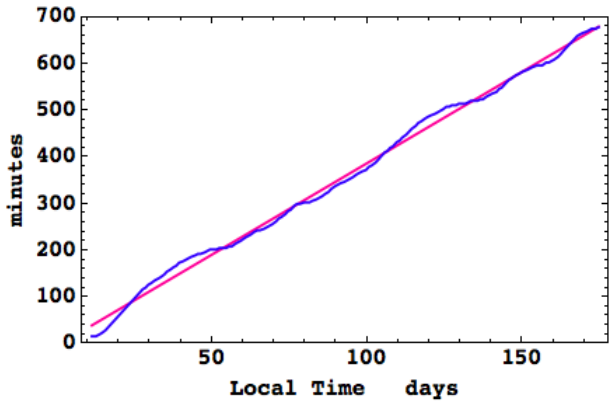

Fig. 3: DeWitte collected data over 178 days and demonstrated that the zero crossing time, see Fig. 2, tracked sidereal time and not local solar time. The plot shows the negative of the drift in the crossing time vs local solar time, and has a slope, determined by the best-fit straight line, of -3.918 minutes per day, compared to the actual average value of -3.932 minutes per day. Again we see fluctuations from day to day.

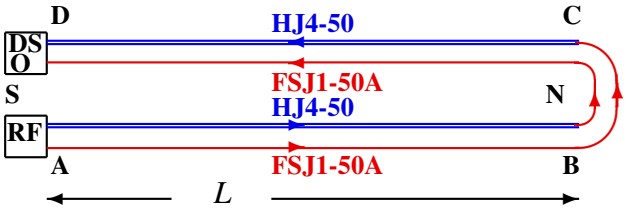

Fig. 4: Because Fresnel drag is absent in RF coaxial cables this dual cable setup, using one clock (10 MHz RF source) and Digital Storage Oscilloscope (DSO) to measure and store timing difference between the two circuits, as in (9)), is capable of detecting the absolute motion of the detector wrt to space, revealing the sidereal rotation effect as well as wave/turbulence effects. Results from such an experiment are shown in Fig. 2. Andrews phase-stablised coaxial cables are used. More recent results are reported in [2].

$$t_{AB} + t_{CD} = \frac{(n_1 + n_2)L}{c} + \frac{v\cos(\theta)L(n_1^2 - n_2^2)}{c^2} + .. \qquad (8)$$

where n_1 and n_2 are the effective refractive indices for the two different RF coaxial cables. There is no clock transport effect as the detector is rotated. Dual circuits reduce temperature effects. The travel time difference of the two circuits at the DSO is then

$$\Delta t = \frac{2v\cos(\theta)L(n_1^2 - n_2^2)}{c^2} + .. \qquad (9)$$

A sample of data is shown in Fig. 2, using RF=10 MHz, and is in excellent agreement with the DeWitte data, the NASA flyby Doppler shift data, and the Michelson-Morley and Miller results.

6 Conclusions

The absence of the Fresnel drag in RF coaxial cables enables 1st order in v/c measurements of the anisotropy of the speed of light. DeWitte pioneered this using the multiple clock technique, and took account of the clock transport effect, while the new dual RF coaxial cable detector uses only one clock. This provides a very simple and robust technique to detect motion wrt the dynamical space. Experiments by Michelson and Morley 1887, Miller 1925/26, DeWitte 1991, Cahill 2006, 2009, 2012, and NASA earth-flyby Doppler shift data now all agree, giving the solar system a speed of $\sim$ 486 km/s in the direction RA=4.3^h, Dec= -75.0°. These experiments have detected the fractal textured dynamical structure of space - the privileged local frame [2]. This report is from the Gravitational Wave Detector Project at Flinders University.

Submitted on July 2, 2012 / Accepted on July 12, 2012

References

1. Cahill R.T. The Roland De Witte 1991 Experiment. *Progress in Physics*, 2006, v. 3, 60–65.
2. Cahill R.T. Characterisation of Low Frequency Gravitational Waves from Dual RF Coaxial-Cable Detector: Fractal Textured Dynamical 3-Space. *Progress in Physics*, 2012, v. 3, 3–10.
3. Cahill R.T. Combining NASA/JPL One-Way Optical-fibre Light-Speed Data with Spacecraft Earth-Flyby Doppler-Shift Data to Characterise 3-Space Flow. *Progress in Physics*, 2009, v. 4, 50–64.
4. Spavieri G., Quintero J., Unnikrishnan S., Gillies G.T., Cavalleri G., Tonni E. and Bosi L. Can the One-Way Speed of Light be used for Detection of Violations of the Relativity Principle? *Physics Letters A*, 2012, v. 376, 795–797.

Additional Proofs to the Necessity of Element No.155, in the Periodic Table of Elements

Albert Khazan

E-mail: albkhazan@gmail.com

Additional versions of the location of the isotopes and element No.155 are suggested to the Periodic Table of Elements.

As was pointed out recently [1], the Periodic Table of Elements ends with element No.155 which manifests the upper limit of the Table after whom no other elements exist. In this connexion the number of the isotopes contained in each single cell of the Nuclear Periodic Table could be interested. (The Nuclear Periodic Table is constructed alike the Periodic Table of Elements, including Periods, Groups, Lanthanides, and Actinides.) Therefore, it is absolutely lawful to compare these two tables targeting the location of element No.155 [2].

Fig. 1 shows an S-shaped arc of the isotopes, whose form changes being dependent on the number of Period, and the number of the isotopes according to the summation of them. As seen, the arc is smooth up to element No.118, where the number of the isotopes of the cell equals to 4468. This is the known last point, after whom the arc transforms into the horizontal straight. In the region of the numbers 114–118, the rate of change of the isotopes in the arc decreases very rapid (4312–4468), upto element No.118 whose cell contains just one isotope. Hence we conclude that only the single isotope is allowed for the number higher than No.118. This was verified for the points No.118, No.138 and No.155, who are thus located along the strict horizontally straight. The common arc can be described by the equation, whose truth of approximation is $R^2 = 1$.

The next version of the graph is constructed by logarithmic coordinates, where the x-coordinate is $\ln X$ and the y-coordinate is $\ln Y$ (see Fig. 2). The original data are: the number Z of each single element (the axis X), and the summary number of the isotopes (the axis Y). Once the graph created, we see a straight line ending by a curve. As seen, the last numbers form a horizontally located straight consisting of the 10 last points. The obtained equation demonstrates the high degree of precision ($R^2 = 0.997$).

The most interesting are the structures, where the two arcs (No.55–No.118) coincide completely with each other. The left side of the parabolas in the tops forms two horizontal areas of 10 points. The two dotted lines at the right side are obtained by the calculations for elements being to 0.5 unit forward. The both equations posses the coefficient $R^2 = 0.992$.

All three presented versions of the distribution of the isotopes in the cell No.155 show clearly that this number should exist as well as element No.155.

Submitted on July 16, 2012 / Accepted on July 20, 2012

References

1. Khazan A. Upper Limit in Mendeleev's Periodic Table — Element No.155. American Research Press, Rehoboth (NM), 2012.
2. The Nuclear Periodic Table, — http://www.radiochemistry.org/periodictable/images/NuclearPeriodicTable-300doi.jpg

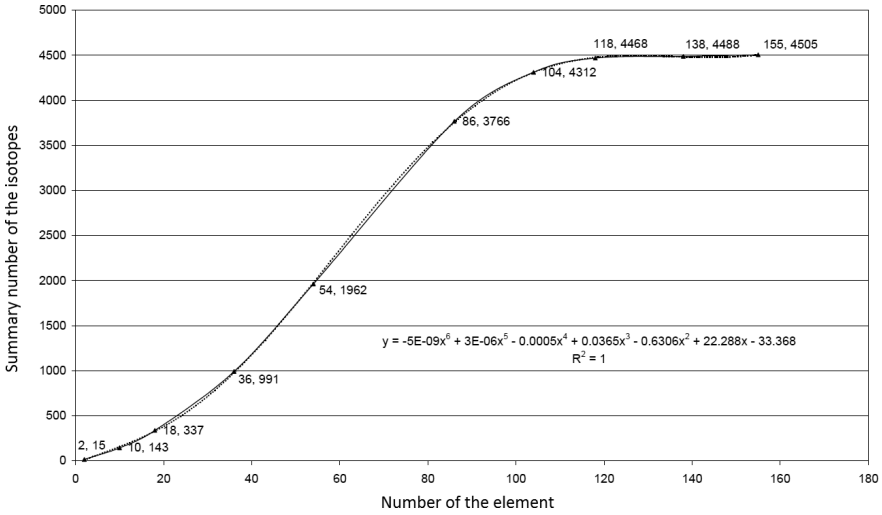

Fig. 1: Dependency of the summary number of the isotopes on the number of the element.

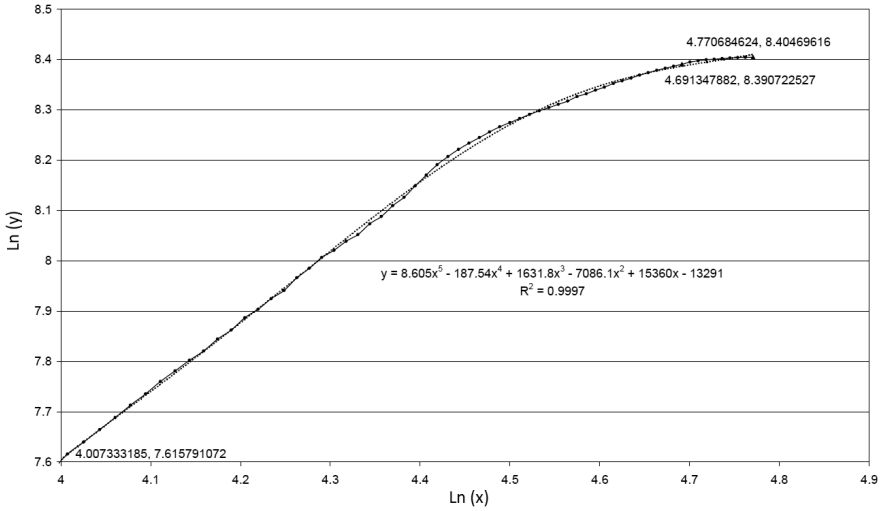

Fig. 2: Dependency of Ln (y) on Ln (x).

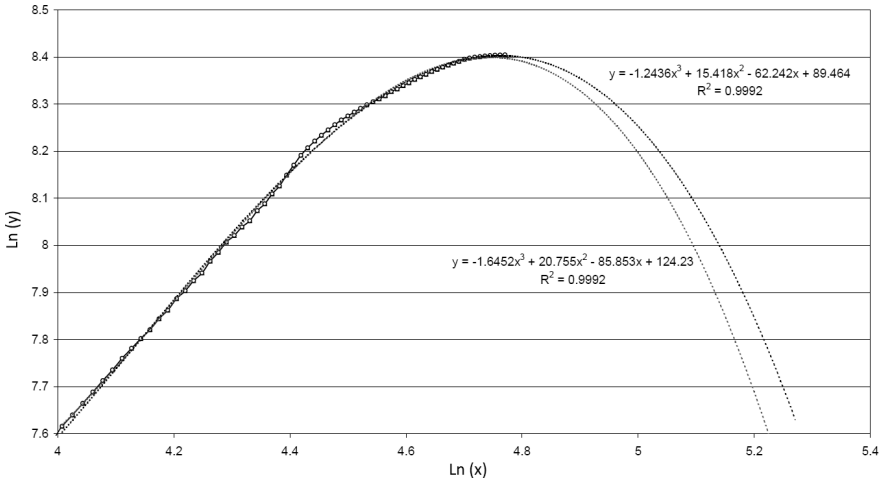

Fig. 3: Dependency of Ln (y) on Ln (x).

Quasar Formation and Energy Emission in Black Hole Universe

Tianxi Zhang

Department of Physics, Alabama A & M University, Normal, Alabama. E-mail: tianxi.zhang@aamu.edu

Formation and energy emission of quasars are investigated in accord with the black hole universe, a new cosmological model recently developed by Zhang. According to this new cosmological model, the universe originated from a star-like black hole and grew through a supermassive black hole to the present universe by accreting ambient matter and merging with other black holes. The origin, structure, evolution, expansion, and cosmic microwave background radiation of the black hole universe have been fully explained in Paper I and II. This study as Paper III explains how a quasar forms, ignites and releases energy as an amount of that emitted by dozens of galaxies. A main sequence star, after its fuel supply runs out, will, in terms of its mass, form a dwarf, a neutron star, or a black hole. A normal galaxy, after its most stars have run out of their fuels and formed dwarfs, neutron stars, and black holes, will eventually shrink its size and collapse towards the center by gravity to form a supermassive black hole with billions of solar masses. This collapse leads to that extremely hot stellar black holes merge each other and further into the massive black hole at the center and meantime release a huge amount of radiation energy that can be as great as that of a quasar. Therefore, when the stellar black holes of a galaxy collapse and merge into a supermassive black hole, the galaxy is activated and a quasar is born. In the black hole universe, the observed distant quasars powered by supermassive black holes can be understood as donuts from the mother universe. They were actually formed in the mother universe and then swallowed into our universe. The nearby galaxies are still very young and thus quiet at the present time. They will be activated and further evolve into quasars after billions of years. At that time, they will enter the universe formed by the currently observed distant quasars as similar to the distant quasars entered our universe. The entire space evolves iteratively. When one universe expands out, a new similar universe is formed from its inside star-like or supermassive black holes.

1 Introduction

Quasars are quasi-stellar objects, from which light is extremely shifted toward the red [1-5]. If their large redshifts are cosmological, quasars should be extremely distant and thus very luminous such that a single quasar with the scale of the solar system can emit the amount of energy comparable to that emitted by dozens of normal galaxies [6-7]. A highly charged quasar may also have significant electric redshift [8].

Quasars are generally believed to be extremely luminous galactic centers powered by supermassive black holes with masses up to billions of solar masses [9-13]. It is usually suggested that the material (e.g., gas and dust) falling into a supermassive black hole is subjected to enormous pressure and thus heated up to millions of degrees, where a huge amount of thermal radiation including waves, light, and X-rays give off [14-16]. However, the density of the falling material, if it is less dense than the supermassive black hole, is only about that of water. In other words, the pressure of the falling gas and dust may not go such high required for a quasar to emit energy as amount of that emitted by hundred billions of the Sun.

According to the Einsteinian general theory of relativity [17] and its Schwarzschild solution [18], the gravitational field (or acceleration) at the surface of a black hole is inversely proportional to its mass or radius. For a supermassive black hole with one billion solar masses, the gravitational field at the surface is only about 1.5×10^4 m/s^2. Although this value is greater than that of the Sun ($\sim$ 270 m/s^2), it is about two-order smaller than that of a white dwarf with 0.8 solar masses and 0.01 solar radii ($\sim 2.2 \times 10^6$ m/s^2), eight-order smaller than that of a neutron star with 1.5 solar masses and 10 km in radius ($\sim 2.0 \times 10^{12}$ m/s^2), and eight-order smaller than that of a star-like black hole with 3 solar masses ($\sim 5 \times 10^{12}$ m/s^2). Table 1 shows the gravitational field at the surface of these typical objects. A black hole becomes less violent and thus less power to the ambient matter and gases as it grows. Therefore, a supermassive black hole may not be able to extremely compress and heat the falling matter by such relative weak gravitational field. It is still unclear about how a quasar is powered by a supermassive black hole.

The Chandra X-ray observations of quasars 4C37.43 and 3C249.1 have provided the evidence of quasar ignition with an enormous amount of gas to be driven outward at high speed or a galactic superwind [19]. The observation of quasar Q0957+561 has shown the existence of an intrinsic magnetic moment, which presents an evidence that the quasar may not have a closed event horizon [20]. In addition, the observations

Object	M (M_{Sun})	R (m)	g_R (m/s^2)
Sun	1	7×10^8	270
White Dwarfs	0.8	7×10^6	2×10^4
Nneutron Stars	1.5	1×10^4	2×10^{12}
Black Holes (BH)	3	3×10^3	5×10^{12}
Spermassive BH	10^9	3×10^{12}	1.5×10^4

Table 1: Mass, radius, and gravitational field at the surface of the Sun, white dwarf, neutron star, star-like black hole (BH), and supermassive black hole.

of the distant quasars have shown that some supermassive black holes were formed when the universe was merely 1-2 billion years after the big bang had taken place [5, 21]. How the supermassive black holes with billions of solar masses were formed so rapidly during the early universe is a great mystery raised by astronomers recently [22]. Theoretically, such infant universe should only contain hydrogen and helium, but observationally scientists have found a lot of heavy elements such as carbon, oxygen, and iron around these distant quasars, especially the large fraction of iron was observed in quasar APM 08279+5255 [23], which has redshift $Z = 3.91$. If the heavy ions, as currently believed, are produced during supernova explosions when stars runs out of their fuel supplies and start to end their lives, then quasars with heavy elements should be much elder than the main sequence stars and normal galaxies.

Recently, in the 211$^{\text{th}}$ AAS meeting, Zhang proposed a new cosmological model called black hole universe [24]. In Paper I [25], Zhang has fully addressed the origin, structure, evolution, and expansion of black hole universe (see also [26]). In Paper II [27], Zhang has quantitatively explained the cosmic microwave background radiation of black hole universe (see [28]), an ideal black body. Zhang [29] summarized the observational evidences of black hole universe. According to this new cosmological model, the universe originated from a hot star-like black hole with several solar masses, and gradually grew through a supermassive black hole with billions of solar masses to the present state with hundred billion-trillions of solar masses by accreting ambient material and merging with other black holes. The entire space is hierarchically structured with infinite layers. The innermost three layers are the universe in which we live, the outside space called mother universe, and the inside star-like and supermassive black holes called child universes. The outermost layer is infinite in radius and limits to zero for both the mass density and absolute temperature, which corresponds to an asymptotically flat spacetime without an edge and outside space and material. The relationship among all layers or universes can be connected by the universe family tree. Mathematically, the entire space can be represented as a set of all black hole universes. A black hole universe is a subset of the entire space or a subspace and the child universes are null sets or empty spaces. All layers or universes are governed by the same physics, the Einsteinian general theory of relativity with the Robertson-Walker metric of spacetime, and expand physically in one way (outward). The growth or expansion of a black hole universe decreases its density and temperature but does not alter the laws of physics.

In the black hole universe model, the observed distant quasars are suggested to be donuts from the mother universe. They were formed in the mother universe from star-like black holes rather than formed inside our universe. In other words, the observed distant quasars actually were child universes of the mother universe, i.e., little sister universes of our universe. After they were swallowed, quasars became child universes of our universe. In general, once a star-like black hole is formed in a normal galaxy, the black hole will eventually inhale, including merge with other black holes, most matter of the galaxy and grow gradually to form a supermassive black hole. Therefore, quasars are supposed to be much elder than the normal stars and galaxies, and thus significantly enriched in heavy elements as measured. Some smaller redshift quasars might be formed in our universe from the aged galaxies that came from the mother universe before the distant quasars entered. Nearby galaxies will form quasars after billions of years and enter the new universe formed from the observed distant quasars as donuts. The entire space evolves iteratively. When one universe expands out, a new similar universe is formed from its inside star-like or supermassive black holes. This study as Paper III develops the energy mechanism for quasars to emit a huge amount of energy according to the black hole universe model.

2 Energy Mechanism for Quasars

As a consequence of the Einsteinian general theory of relativity, a main sequence star, at the end of its evolution, will become, in terms of its mass, one of the follows: a dwarf, a neutron star, or a stellar black hole. A massive star ends its life with supernova explosion and forms a neutron star or a black hole. Recently, Zhang [30] proposed a new mechanism called gravitational field shielding for supernova explosion. For the evolution of the entire galaxy, many details have been uncovered by astronomers, but how a galaxy ends its life is still not completely understood. In the black hole universe, all galaxies are suggested to eventually evolve to be supermassive black holes. Galaxies with different sizes form supermassive black holes with different masses. Quasars are formed from normal galaxies through active galaxies as shown in Figure 1.

Once many stars of a galaxy have run out of their fuels and formed dwarfs, neutral stars, and black holes, the galaxy shrinks its size and collapses toward the center, where a massive black hole with millions of solar masses may have already existed, by the gravity. During the collapse, the dwarfs,

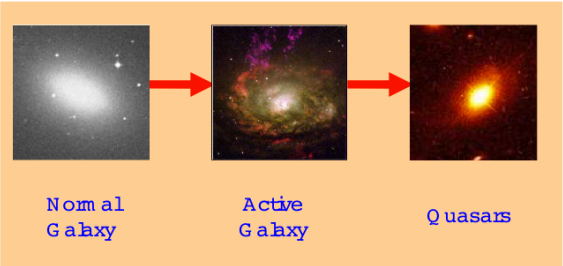

Fig. 1: Formation of quasars. A normal galaxy evolves into an active one and ends by a quasar (Images of Hubble Space Telescope).

neutron stars, and stellar black holes are merging each other and gradually falling into the massive black hole at the center to form a supermassive black hole with billions of solar masses. When stellar black holes merge and collapse into a supermassive black hole, a huge amount of energies are released. In this situation, the galaxy is activated and a quasar is born.

In a normal galaxy, such as our Milky Way, most stars are still active and bright because they have not yet run out of their fuels to form dwarfs, neutron stars, and black holes. In the disk of a normal galaxy, there should be not much of such hardly observed matter as shown by the measurements [31-32]. In the center of a normal galaxy, a quiet massive black hole with millions of solar masses may exist. Once many stars have run out of their fuels and evolved into dwarfs, neutron stars, and black holes, the disk of the galaxy becomes dim, though intensive X-rays can emit near the neutron stars and black holes, and starts to shrink and collapse. As the galaxy collapses, the black holes fall towards (or decrease of orbital radius) the center and merge with the massive black hole at the center, where huge amounts of energies leak out of the black holes through the connection region, where the event horizons are broken. The galaxy first activates with a luminous nucleus and then becomes a quasar in a short period at the evolution end.

The inside space of a black hole is a mystery and can never be observed by an observer in the external world. It is usually suggested that when a star forms a Schwarzschild black hole its matter will be collapsed to the singularity point with infinite density. Material falling into the black hole will be crunched also to the singularity point. Other regions under the event horizon of the black hole with radius $R = 2GM/c^2$ are empty. The inside space of the black hole was also considered to be an individual spacetime with matter and field distributions that obeys the Einsteinian general theory of relativity. Gonzalez-Diaz [33] derived a spacetime metric for the region of nonempty space within the event horizon from the Einsteinian field equation.

In the black hole universe model, we have considered the inside space of the Schwarzschild black hole as an individual spacetime, which is also governed by the Friedmann equation

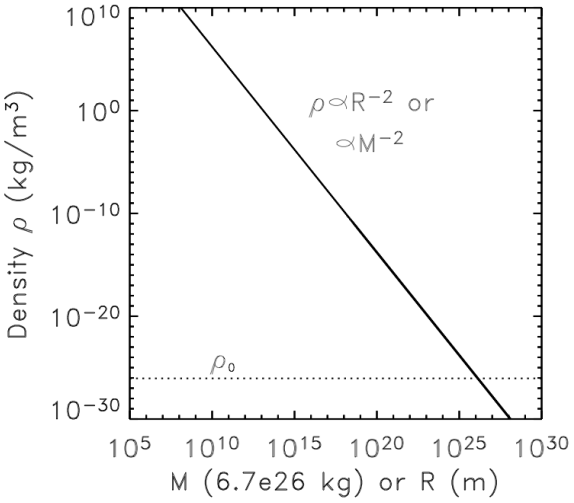

Fig. 2: The density of a black hole versus its mass or radius (solid line). The dotted line refers to $\rho = \rho_0$ the density of the present universe, so that the intersection of the two lines represents the density, radius, and mass of the present universe.

with the Robertson-Walker metric of spacetime and where matter is uniformly distributed rather than crunched into a single point. Highly curved spacetime sustains the highly dense matter and strong gravity. A black hole governed by the Einsteinian general theory of relativity with the Robertson-Walker metric of spacetime is usually static with a constant mass-radius ratio called M-R relation or a constant density when it does not eat or accrete matter from its outside space [25]. The density of the matter is given by

$$\rho = \frac{M}{V} = \frac{3c^2}{8\pi GR^2} = \frac{3c^6}{32\pi G^3 M^2}, \qquad (1)$$

where $V = 4\pi R^3/3$ is the volume. Figure 2 shows the density of black hole as a function of its radius or mass. It is seen that the density of the black hole universe is inversely proportional to the square of radius or mass. At the present time, the mass and radius of the universe are 9×10^{51} kg and 1.3×10^{26} m, respectively, if the density of the universe is chosen to be $\rho_0 = 9 \times 10^{-27}$ kg/m^3.

The total radiation energy inside a black hole, an ideal black body, is given by

$$U = \frac{4}{3}\pi\beta R^3 T^4 = \mu R^3 T^4, \qquad (2)$$

where T is the temperature and β is a constant [27]. The constant μ is given by

$$\mu = \frac{4}{3}\pi\beta = \frac{32\pi^6 k_B^4}{45h^3c^3}, \qquad (3)$$

where k_B is the Boltzmann constant, h is the Planck constant, and c is the light speed. Using the Robertson-Walker metric

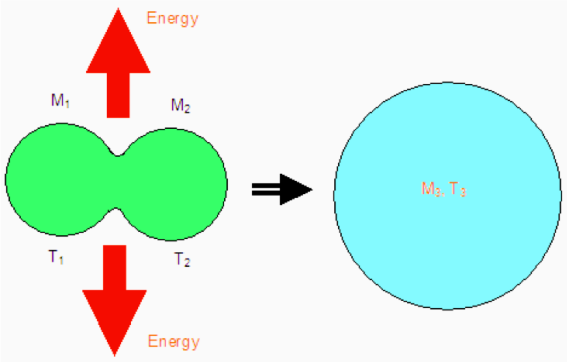

Fig. 3: A sketch for two star-like black holes to merge into a larger one and release energy from the reconnection region where the event horizons break.

with the curvature parameter $k = 1$ to describe the black hole spacetime, we have obtained in Paper I, from the Einsteinian field equation, that the black hole is stable $dR/dt = 0$ if no material and radiation enter, otherwise the black hole enlarges or expands its size at a rate $dR/dt = RH$ and thus decrease its density and temperature. Here H is the Hubble parameter.

When two black holes merge, their event horizons first break and then reconnect to form a single enveloping horizon and therefore a larger black hole. Brandt et al. [34] simulated the merge and collision of black holes. During the period of the reconnection of the event horizons, a huge amount of radiation energy leak/emit out from the black holes through the connection region, where the formed event horizon is still concave and has negative curvature. As many star-like black holes merge, a supermassive black hole or a quasar forms.

To illustrate the energy emission of a quasar, we first consider two black holes with mass M_1, M_2 (or radius R_1, R_2) and temperature T_1, T_2 to merge into a larger black hole with mass $M_3 = M_1 + M_2$ (or radius $R_3 = R_1 + R_2$ because of the M-R relation) and temperature T_3. Figure 3 show a schematic sketch for the merging of two black holes and the energy emission from them. This is somewhat similar to the energy release by fusion of two light nuclei. The total energy radiated from the collision region can be estimated as

$$E = \mu R_1^3 T_1^4 + \mu R_2^3 T_2^4 - \mu R_3^3 T_3^4. \tag{4}$$

It can be positive if the merged black hole is colder than the merging black holes (i.e., $E > 0$, if $T_3 < T_1, T_2$).

For N star-like black holes and one massive black hole to merge into a supermassive black hole, the total radiation energy that is emitted out can be written as

$$E_{\text{total}} = \mu \sum_{j=0}^{N} R_j^3 T_j^4 - \mu R_Q^3 T_Q^4, \tag{5}$$

where R_j and T_j are the radius and temperature of the j^{th} stellar black hole ($j = 0$ for the massive black hole existed at the center), R_Q and T_Q are the radius and temperature of the supermassive black hole formed at the end, and N is the number of the star-like black holes formed in the galaxy. The radius of the supermassive black hole can be estimated as

$$R_Q = \sum_{j=0}^{N} R_j. \tag{6}$$

Considering all the star-like black holes to have the same size and temperature (for simplicity or in an average radius and temperature), we have

$$E_{\text{total}} = \mu R_0^3 T_0^4 + \mu N R_j^3 T_j^4 - \mu N^3 R_j^3 T_Q^4. \tag{7}$$

Here we have also considered that $R_Q >> R_0$ and

$$R_Q = R_0 + N R_j \simeq N R_j. \tag{8}$$

Paper II has shown that the temperature of a black hole including our black hole universe depends on its size or radius. For a child universe (i.e., star-like or supermassive black hole), the relation is approximately power law,

$$T \propto \frac{1}{R^\delta}, \tag{9}$$

where δ is a power law index less than about 3/4. Applying this temperature-radius relation into Eqs. (8) and (7), we have,

$$T_Q = T_j N^{-\delta}, \tag{10}$$

and

$$E_{\text{total}} = \mu R_j^3 T_j^4 N (1 - N^{2-4\delta}). \tag{11}$$

The average luminosity of a collapsing galaxy (or quasar) can be written as

$$L \equiv E_{\text{total}}/\tau \tag{12}$$

where τ is the time for all star-like black holes in a galaxy to merge into a single supermassive black hole.

It is seen that the luminosity of a quasar increases with δ, N, R_j, and T_j, but decreases with τ. As an example, choosing $R_j = 9$ km (or $M_j \simeq 3M_s$), $T_j = 10^{12}$ K, $N = 10^9$, and $\tau = 10^9$ years, we obtain $L \simeq 7.3 \times 10^{37}$ W, which is $\sim 2 \times 10^{11}$ times that of the Sun and therefore about the order of a quasar's luminosity [35]. The formed supermassive black hole will be three billion solar masses. Here δ is chosen to be greater enough (e.g., 0.55). For a hotter T_j, a shorter τ, or a larger N, the luminosity is greater. Therefore, if quasars are collapsed galaxies at their centers that star-like black holes are merging into supermassive black holes, then the huge luminosities of quasars can be understood. The extremely emitting of energy may induce extensive shocks and produce jet flows of matter outward along the strong magnetic field lines.

To see how the luminosity of a quasar depends on the parameters N, δ, T_j, and τ, we plot the luminosity of a collapsing galaxy (merging black holes or an ignited quasar) in

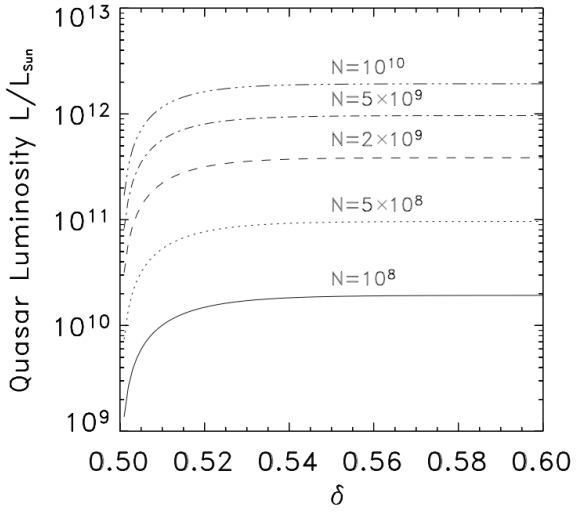

Fig. 4: Quasar luminosity vs. δ with $N = 10^8, 5\times10^5, 2\times10^9, 5\times10^9, 10^{10}$. δ should be greater than 0.5 for a quasar to emit energy. The luminosity saturates when $\delta \gtrsim 0.52$.

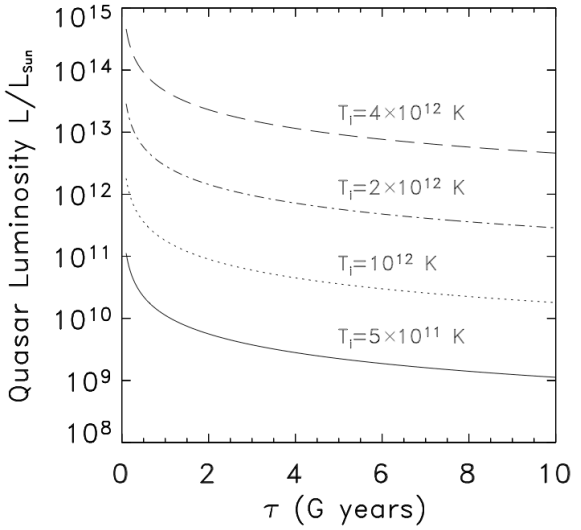

Fig. 5: Quasar luminosity vs. τ with $N = 10^8, 5\times10^5, 2\times10^9, 5\times10^9, 10^{10}$. It increases with the temperature of star-like black holes but decreases with the time for them to merge.

Figure 4 as a function of δ and in Figure 5 as a function of τ with different N. In Figure 4, we let δ vary from 0.5 to 0.6 as the x-axis and N be equal to 10^8, 2×10^8, 5×10^8, and 10^9, where other parameters are fixed at $R_j = 9$ km, $T_j = 10^{12}$ K, and $\tau = 10^9$ years. In Figure 5, we let τ vary from 10^8 years to 10^{10} years as the x-axis and T_j equal to 5×10^{11}, 10^{12}, 2×10^{12}, and 4×10^{12} K, where other parameters are fixed at $R_j = 9$ km, $N = 10^9$, and $\delta = 0.55$.

It is seen from Figure 4 that the luminosity of a quasar increases with δ and N, and saturates when $\delta \gtrsim 0.52$. For a supermassive black hole to emit energy, δ must be greater than about 0.5. Paper II has shown $\delta \lesssim 3/4 = 0.75$. From Figure 5, we can see that the luminosity decreases with the collapsing time τ and increases with T_j.

Corresponding to the possible thermal history given by Paper II, δ varies as the black hole universe grows. Figure 6 plots the parameters γ defined in Paper II and δ as functions of the radius R. It is seen that when a supermassive black hole grows up to $R \gtrsim 10^{14}$ km (or $M \gtrsim 3\times10^5$ billion solar masses) it does not emit energy when it merges with other black holes because $\delta < 0.5$. In the observed distant voids, it is possible to have this kind of objects called mini-black-hole universes. The observed distant quasars may have grown up to this size or mass now and so that quite at present. A cluster, when most of its galaxies become supermassive black holes or quasars, will merge into a mini-black-hole universe.

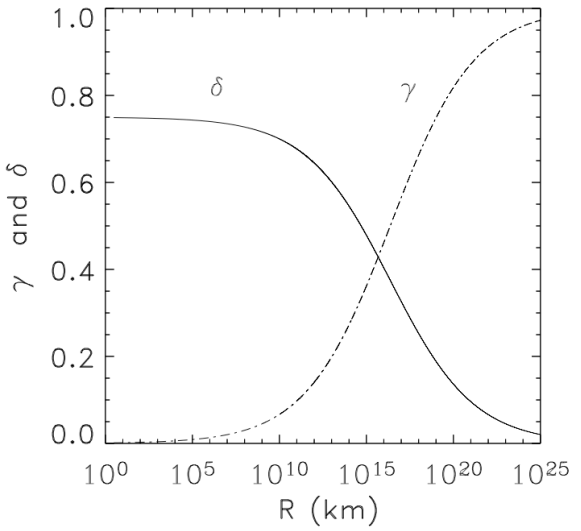

Fig. 6: Parameters γ and δ versus radius R. When a supermassive black hole grows to $R \gtrsim 3\times10^{14}$ km or $M \gtrsim 10^{14}$ solar masses, it does not emit energy because $\delta < 0.5$.

3 Discussions and Conclusions

If there does not pre-exist a massive black hole at the center of a galaxy, a supermassive black hole can also be formed from the galaxy. As the galaxy shrinks it size, a hot star-like black hole enlarges its size when it swallows dwarfs or neutron stars, which may also collapse to form black holes [36] or merges with other black holes and forms a supermassive black hole at the end.

As a summary, we proposed a possible explanation for quasars to ignite and release a huge amount of energy in accord with the black hole universe model. General relativity tells us that a main sequence star will, in terms of its mass, form a dwarf, a neutron star, or a black hole. After many stars in a normal galaxy have run out of their fuels and formed dwarfs, neutron stars, and black holes, the gravity cause the galaxy to eventually collapse and form a supermassive black

hole with billions of solar masses. It has been shown that this collapse can lead to the extremely hot stellar black holes to merge each other and further into the massive black hole at the center and release intense thermal radiation energy as great as a quasar emits. When the stellar black holes of a galaxy collapse and merge into a supermassive black hole, the galaxy is activated and a quasar is born. The observed distant quasars were donuts from the mother universe. They were actually formed in the mother universe as little sisters of our universe. After the quasars entered our universe, they became our universe's child universes. The results from this quasar model are consistent with observations.

Acknowledgements

This work was supported by the NASA EPSCoR grant (NNX-07AL52A), NSF CISM and MRI grants, AAMU Title III program, and National Natural Science Foundation of China (G40890161).

Submitted on July 17, 2012 / Accepted on July 22, 2012

References

1. Burbidge E.M. Quasi-stellar objects. *Annual Review of Astronomy and Astrophysics*, 1967, v. 5, 399–452.
2. Burbidge G. Redshifts and distances. *Nature*, 1979, v. 282, 451–455.
3. Hazard C., McMahon R. New quasars with Z = 3.4 and 3.7 and the surface density of very high redshift quasars. *Nature*, 1985, v. 314, 238–240.
4. Bechtold J. et al. Chandra survey of radio-quiet, high-redshift quasars. *The Astrophysical Journal*, 2003, v. 588, 119–127.
5. Fan X.H. et al. A survey of z>5.7 quasars in the Sloan Digital Sky Survey: II. Discovery of three additional quasars at z>6. *The Astronomical Journal*, 2003, v. 125, 1649–1659.
6. Hartwick F.D.A., Schade D. The space distribution of quasars. *Annual Review of Astronomy and Astrophysics*, 1990, v. 28, 437–489.
7. Boyle B.J. et al. The 2dF QSO redshift survey - I. The optical luminosity function of quasi-stellar objects. *Monthly Notices of the Royal Astronomical Society*, 2000, v. 317, 1014–1022.
8. Zhang T.X. Electric redshift and quasars. *Astrophysical Journal Letters*, 2006, v. 636, L61–L64.
9. Lynden-Bell D. Galactic nuclei as collapsed old quasars. *Nature*, 1969, v. 223, 690–694.
10. Rees M.J. Black hole models for active galactic nuclei. *Annual Review of Astronomy and Astrophysics*, 1984, v. 22, 471–506.
11. Bahcall J.N., Kirhakos S., Saxe D.H., Schneider D.P. Hubble Space Telescope Images of a sample of 20 nearby luminous quasars. *The Astrophysical Journal*, 1997, v. 479, 642–658.
12. Lobanov A.P., Roland J. A supermassive binary black hole in the quasar 3C 345. *Astronomy and Astrophysics*, 2005, v. 431, 831–846.
13. Begelman M.C., King A.R., Pringle J.E. The nature of SS433 and the ultraluminous X-ray sources. *Monthly Notices of the Royal Astronomical Society*, 2006, v. 370, 399–404.
14. Shapiro S.L., Teukolsky S.A. The collapse of dense star clusters to supermassive black holes - The origin of quasars and AGNs. *The Astrophysical Journal Letters*, 1985, v. 292, L41–L44.
15. Wyithe J., Stuart B., Loeb A. Self-regulated growth of supermassive black holes in galaxies as the origin of the optical and X-ray luminosity functions of quasars. *The Astrophysical Journal*, 2003, v. 595, 614–623.
16. Reeves J.N., Pounds K., Uttley P., Kraemer S., Mushotzky R., Yaqoob T., George I.M., Turner T.J. Evidence for gravitational infall of matter onto the supermassive black hole in the quasar PG 1211+143? *The Astrophysical Journal Letters*, 2005, v. 633, L81–L84.
17. Einstein A. Die Grundlage der allgemeinen Relativitätstheorie, *Annalen der Physik*, 1916, v. 354, 769–822.
18. Schwarzschild K. On the gravitational field of a mass point according to Einstein's theory. *Sitzungsberichte der Königlich Preussischen Akademie der Wissenschaften zu Berlin, Phys.-Math.*, 1916, 189–196.
19. Stockton A., Fu H., Henry J.P., Canalizo G. Extended X-ray emission from QSOs. *The Astrophysical Journal*, 2006, v. 638, 635–641.
20. Schild R.E., Leiter D.J., Robertson, S.L. Observations supporting the existence of an intrinsic magnetic moment inside the central compact object within the quasar Q0957+561. *The Astronomical Journal*, 2006, v. 132, 420–432.
21. Fan X.F. et al. A survey of $z > 5.8$ quasars in the Sloan Digital Sky Survey. I. Discovery of three new quasars and the spatial density of luminous quasars at $z \sim 6$. *Astron. J.*, 2001, v. 122, 2833–2849.
22. Hamann F., Ferland G. Elemental abundances in quasistellar objects: Star formation and galactic nuclear evolution at high redshifts. *Annual Review of Astronomy and Astrophysics*, 1999, v. 37, 487–531.
23. Hasinger G., Schartel N., Komossa S. Discovery of an ionized Fe K edge in the z=3.91 broad absorption line quasar APM 08279+5255 with XMM-Newton. *The Astrophysical Journal Letters*, 2002, v. 573, L77–L80.
24. Zhang T.X. A new cosmological model: Black hole universe, *Bulletin of the American Astronomical Society*, 2007, v. 39, 1004–1004.
25. Zhang T.X. A new cosmological model: Black hole universe, *Progress in Physics*, 2009a, v. 3, 3–11 (Paper I).
26. Zhang T.X. Anisotropic expansion of the black hole universe. *Bulletin of the American Astronomical Society*, 2009b, v. 41, 499–499.
27. Zhang T.X. Cosmic microwave background radiation of black hole universe. *Astrophysics and Space Science*, 2010a, v. 330, 157–165 (Paper II).
28. Zhang T.X. Cosmic microwave background radiation of black hole universe, *Bulletin of the American Astronomical Society*, 2009c, v. 41, 754–754.
29. Zhang T.X. Observational evidences of black hole universe. *Bulletin of the American Astronomical Society*, 2010b, v. 42, 314–314.
30. Zhang T.X. Gravitational field shielding and supernova explosions. *The Astrophysical Journal Letters*, 2010c, v. 725, L117–L120.
31. Hellemans A. ASTRONOMY: Galactic disk contains no dark matter *Science*, 1997, v. 278, 1230–1230.
32. Creze M., Chereul E., Bienaymo O., Pichon C. The distribution of nearby stars in phase space mapped by Hipparcos. I. The potential well and local dynamical mass. *Astronomy and Astrophysics*, 1998, v. 329, 920–936.
33. Gonzalez-Diaz P.E. The spacetime metric inside a black hole. *Nuovo Cimento Letters*, 1981, v. 2, L161–L163.
34. Brandt S., Font J.A., Ibanez J.M., Masso J., Seidel E. Numerical evolution of matter in dynamical axisymmetric black hole spacetimes I. Methods and tests. *Computer Physics Commmunications*, 2000, v. 124, 169–196.
35. Sparke L.S., Gallaher J.S. Galaxies in the Universe: an Introduction, Cambridge University Press, 2000.
36. Dermer C.D., Atoyan A. Collapse of neutron stars to black holes in binary systems: A model for short gamma-ray bursts. *The Astrophysical Journal Letters*, 2006, v. 643, L13–L16.

Generalizations of the Distance and Dependent Function in Extenics to $2D$, $3D$, and $n-D$

Florentin Smarandache
University of New Mexico, Mathematics and Science Department, 705 Gurley Ave., Gallup, NM 87301, USA
E-mail: smarand@unm.edu

Dr. Cai Wen defined in his 1983 paper: — the distance formula between a point x_0 and a one-dimensional (1D) interval $<a,b>$; — and the dependence function which gives the degree of dependence of a point with respect to a pair of included $1D$-intervals. His paper inspired us to generalize the Extension Set to two-dimensions, i.e. in plane of real numbers R^2 where one has a rectangle (instead of a segment of line), determined by two arbitrary points $A(a_1,a_2)$ and $B(b_1,b_2)$. And similarly in R^3, where one has a prism determined by two arbitrary points $A(a_1,a_2,a_3)$ and $B(b_1,b_2,b_3)$. We geometrically define the linear and non-linear distance between a point and the $2D$ and $3D$-extension set and the dependent function for a nest of two included $2D$ and $3D$-extension sets. Linearly and non-linearly attraction point principles towards the optimal point are presented as well. The same procedure can be then used considering, instead of a rectangle, any bounded $2D$-surface and similarly any bounded $3D$-solid, and any bounded $(n-D)$-body in R^n. These generalizations are very important since the Extension Set is generalized from one-dimension to 2, 3 and even n-dimensions, therefore more classes of applications will result in consequence.

1 Introduction

Extension Theory (or Extenics) was developed by Professor Cai Wen in 1983 by publishing a paper called Extension Set and Non-Compatible Problems. Its goal is to solve contradictory problems and also nonconventional, nontraditional ideas in many fields. Extenics is at the confluence of three disciplines: philosophy, mathematics, and engineering. A contradictory problem is converted by a transformation function into a non-contradictory one. The functions of transformation are: extension, decomposition, combination, etc. Extenics has many practical applications in Management, Decision-Making, Strategic Planning, Methodology, Data Mining, Artificial Intelligence, Information Systems, Control Theory, etc. Extenics is based on matter-element, affair-element, and relation-element.

2 Extension Distance in $1D$-space

Let's use the notation $<a,b>$ for any kind of closed, open, or half-closed interval $[a,b]$, (a,b), $(a,b]$, $[a,b)$. Prof. Cai Wen has defined the extension distance between a point x_0 and a real interval $X=<a,b>$, by

$$\rho(x_0,X)=\left|x_0-\frac{a+b}{2}\right|-\frac{b-a}{2}, \tag{1}$$

where in general:

$$\rho:(R,R^2)\to(-\infty,+\infty). \tag{2}$$

Algebraically studying this extension distance, we find that actually the range of it is:

$$\rho(x_0,X)\in\left[-\frac{b-a}{2},+\infty\right] \tag{3}$$

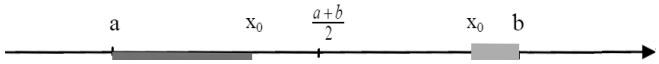

Fig. 1:

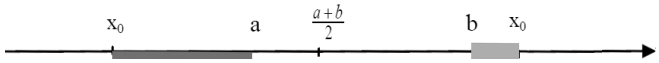

Fig. 2:

or its minimum range value $-\left(\frac{b-a}{2}\right)$ depends on the interval X extremities a and b, and it occurs when the point x_0 coincides with the midpoint of the interval X, i.e. $x_0=\frac{a+b}{2}$. The closer is the *interior point* x_0 to the midpoint of the interval $<a,b>$, the negatively larger is $\rho(x_0,X)$.

In Fig. 1, for interior point x_0 between a and $\frac{a+b}{2}$, the extension distance $\rho(x_0,X)=a-x_0$ is the *negative length of the brown line segment* [left side]. Whereas for interior point x_0 between $\frac{a+b}{2}$ and b, the extension distance $\rho(x_0,X)=x_0-b$ is the *negative length of the blue line segment* [right side]. Similarly, the further is *exterior point* x_0 with respect to the closest extremity of the interval $<a,b>$ to it (i.e. to either a or b), the positively larger is $\rho(x_0,X)$.

In Fig. 2, for exterior point $x_0<a$, the extension distance $\rho(x_0,X)=a-x_0$ is the positive length of the brown line segment [left side]. Whereas for exterior point $x_0>b$, the extension distance $\rho(x_0,X)=x_0-b$ is the *positive length of the blue line segment* [right side].

3 Principle of the Extension $1D$-Distance

Geometrically studying this extension distance, we find the following principle that Prof. Cai Wen has used in 1983

defining it:

> $\rho(x_0, X)$ is *the geometric distance between the point* x_0 *and the closest extremity point of the interval* $<a, b>$ *to it (going in the direction that connects* x_0 *with the optimal point), distance taken as negative if* $x_0 \in <a, b>$, *and as positive if* $x_0 \subset <a, b>$.

This principle is very important in order to generalize the extension distance from 1D to 2D (two-dimensional real space), 3D (three-dimensional real space), and $n-D$ (n-dimensional real space).

The extremity points of interval $< a, b>$ are the point a and b, which are also the boundary (frontier) of the interval $< a, b>$.

4 Dependent Function in 1D-Space

Prof. Cai Wen defined in 1983 in 1D the Dependent Function $K(y)$. If one considers two intervals X_0 and X, that have no common end point, and $X_0 \subset X$, then:

$$K(y) = \frac{\rho(y, X)}{\rho(y, X) - \rho(y, X_0)}. \qquad (4)$$

Since $K(y)$ was constructed in 1D in terms of the extension distance $\rho(.,.)$, we simply generalize it to higher dimensions by replacing $\rho(.,.)$ with the generalized in a higher dimension.

5 Extension Distance in 2D-Space

Instead of considering a segment of line AB representing the interval $<a, b>$ in 1R, we consider a rectangle $AMBN$ representing all points of its surface in 2D. Similarly as for 1D-space, the rectangle in 2D-space may be closed (i.e. all points lying on its frontier belong to it), open (i.e. no point lying on its frontier belong to it), or partially closed (i.e. some points lying on its frontier belong to it, while other points lying on its frontier do not belong to it).

Let's consider two arbitrary points $A(a_1, a_2)$ and $B(b_1, b_2)$. Through the points A and B one draws parallels to the axes of the Cartesian system XY and one thus one forms a rectangle $AMBN$ whose one of the diagonals is just AB.

Let's note by O the midpoint of the diagonal AB, but O is also the center of symmetry (intersection of the diagonals) of the rectangle $AMBN$. Then one computes the distance between a point $P(x_0, y_0)$ and the rectangle $AMBN$. One can do that following the same principle as Dr. Cai Wen did:

— compute the distance in 2D (two dimensions) between the point P and the center O of the rectangle (intersection of rectangle's diagonals);

— next compute the distance between the point P and the closest point (let's note it by P') to it on the frontier (the rectangle's four edges) of the rectangle $AMBN$.

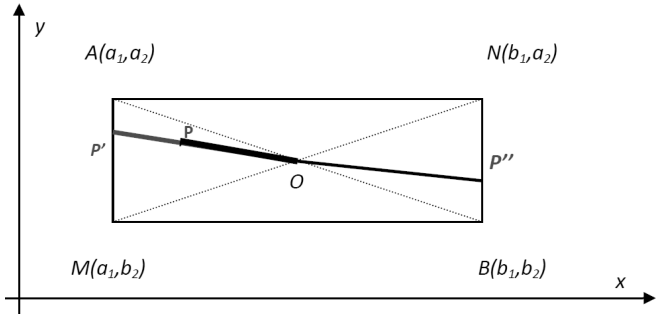

Fig. 3: P is an interior point to the rectangle $AMBN$ and the optimal point O is in the center of symmetry of the rectangle.

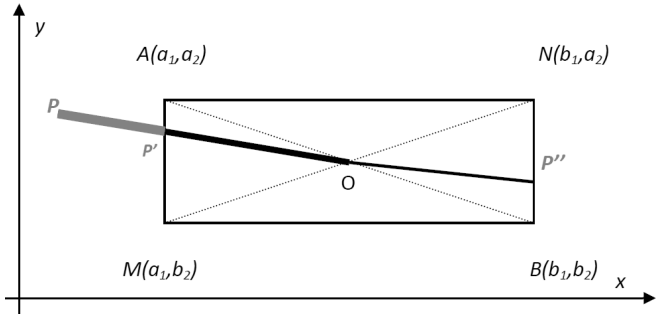

Fig. 4: P is an exterior point to the rectangle $AMBN$ and the optimal point O is in the center of symmetry of the rectangle.

This step can be done in the following way: considering P' as the intersection point between the line PO and the frontier of the rectangle, and taken among the intersection points that point P' which is the closest to P; this case is entirely consistent with Dr. Cai's approach in the sense that when reducing from a 2D-space problem to two 1D-space problems, one exactly gets his result.

The Extension 2D-Distance, for $P \neq O$, will be:

$$\rho((x_0, y_0), AMBN) = d(\text{point } P, \text{ rectangle } AMBN) =$$
$$= |PO| - |P'O| = \pm|PP'|, \qquad (5)$$

i) which is equal to the negative length of the red segment $|PP'|$ in Fig. 3, when P is interior to the rectangle $AMBN$;

ii) or equal to zero, when P lies on the frontier of the rectangle $AMBN$ (i.e. on edges AM, MB, BN, or NA) since P coincides with P';

iii) or equal to the positive length of the blue segment $|PP'|$ in Fig. 4, when P is exterior to the rectangle $AMBN$, where $|PO|$ means the classical 2D-distance between the point P and O, and similarly for $|P'O|$ and $|PP'|$.

The Extension 2D-Distance, for the optimal point, i.e. $P = O$, will be

$$\rho(O, AMBN) = d(\text{point } O, \text{ rectangle } AMBN) =$$
$$= -\max d(\text{point } O, \text{ point } M \text{ on the frontier of } AMBN). \qquad (6)$$

The last step is to devise the Dependent Function in $2D$-space similarly as Dr. Cai's defined the dependent function in $1D$. The midpoint (or center of symmetry) O has the coordinates

$$O\left(\frac{a_1+b_1}{2}, \frac{a_2+b_2}{2}\right). \tag{7}$$

Let's compute the

$$|PO| - |P'O|. \tag{8}$$

In this case, we extend the line OP to intersect the frontier of the rectangle $AMBN$. P' is closer to P than P'', therefore we consider P'. The equation of the line PO, that of course passes through the points $P(x_0, y_0)$ and $O\left(\frac{a_1+b_1}{2}, \frac{a_2+b_2}{2}\right)$, is:

$$y - y_0 = \frac{\frac{a_2+b_2}{2} - y_0}{\frac{a_1+b_1}{2} - x_0}(x - x_0). \tag{9}$$

Since the x-coordinate of point P' is a_1 because P' lies on the rectangle's edge AM, one gets the y-coordinate of point P' by a simple substitution of $x_{P'} = a_1$ into the above equality:

$$y_{P'} = y_0 + \frac{a_2+b_2-2y_0}{a_1+b_1-2x_0}(a_1 - x_0). \tag{10}$$

Therefore P' has the coordinates

$$P'\left[x_{P'} = a_1,\ y_{P'} = y_0 + \frac{a_2+b_2-2y_0}{a_1+b_1-2x_0}(a_1 - x_0)\right]. \tag{11}$$

The distance

$$d(PQ) = |PQ| = \sqrt{\left(x_0 - \frac{a_1+b_1}{2}\right)^2 + \left(y_0 - \frac{a_2+b_2}{2}\right)^2}, \tag{12}$$

while the distance

$$\begin{aligned} d(P', Q) &= |P'Q| = \\ &= \sqrt{\left(a_1 - \frac{a_1+b_1}{2}\right)^2 + \left(y_{P'} - \frac{a_2+b_2}{2}\right)^2} = \\ &= \sqrt{\left(\frac{a_1-b_1}{2}\right)^2 + \left(y_{P'} - \frac{a_2+b_2}{2}\right)^2}. \end{aligned} \tag{13}$$

Also, the distance

$$d(PP') = |PP'| = \sqrt{(a_1 - x_0)^2 + (y_{P'} - y_0)^2}. \tag{14}$$

Whence the Extension $2D$-distance formula

$$\rho[(x_0, y_0),\ AMBN] =$$

$$= d[P(x_0, y_0),\ A(a_1, a_2)\, MB(b_1, b_2)\, N] =$$

$$= |PQ| - |P'Q| \tag{15}$$

$$= \sqrt{\left(x_0 - \frac{a_1+b_1}{2}\right)^2 + \left(y_0 - \frac{a_2+b_2}{2}\right)^2} - \sqrt{\left(\frac{a_1-b_1}{2}\right)^2 + \left(y_{P'} - \frac{a_2+b_2}{2}\right)^2} \tag{16}$$

$$= \pm|PP'| \tag{17}$$

$$= \pm\sqrt{(a_1 - x_0)^2 + (y_{P'} - y_0)^2}, \tag{18}$$

where

$$y_{P'} = y_0 + \frac{a_2+b_2-2y_0}{a_1+b_1-2x_0}(a_1 - x_0). \tag{19}$$

6 Properties

As for $1D$-distance, the following properties hold in $2D$:

6.1 Property 1

a) $(x, y) \in \mathrm{Int}(AMBN)$ if $\rho[(x, y), AMBN] < 0$, where $\mathrm{Int}(AMBN)$ means interior of $AMBN$;

b) $(x, y) \in \mathrm{Fr}(AMBN)$ if $\rho[(x, y), AMBN] = 0$, where $\mathrm{Fr}(AMBN)$ means frontier of $AMBN$;

c) $(x, y) \notin AMBN$ if $\rho[(x, y), AMBN] > 0$.

6.2 Property 2

Let $A_0M_0B_0N_0$ and $AMBN$ be two rectangles whose sides are parallel to the axes of the Cartesian system of coordinates, such that they have no common end points, and $A_0M_0B_0N_0 \subset AMBN$. We assume they have the same optimal points $O_1 \equiv O_2 \equiv O$ located in the center of symmetry of the two rectangles. Then for any point $(x, y) \subset R^2$ one has $\rho[(x, y), A_0M_0B_0N_0] \geqslant \rho[(x, y), AMBN]$. See Fig. 5.

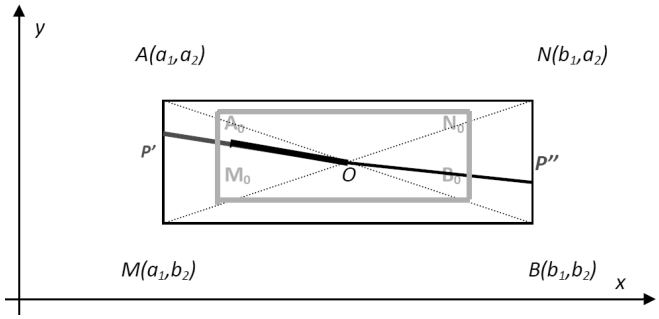

Fig. 5: Two included rectangles with the same optimal points $O_1 \equiv O_2 \equiv O$ located in their common center of symmetry.

7 Dependent $2D$-Function

Let $A_0M_0B_0N_0$ and $AMBN$ be two rectangles whose sides are parallel to the axes of the Cartesian system of coordinates, such that they have no common end points, and $A_0M_0B_0N_0 \subset AMBN$.

The Dependent $2D$-Function formula is:

$$K_{2D(x,y)} = \frac{\rho[(x, y), AMBN]}{\rho[(x, y), AMBN,] - \rho[(x, y), A_0M_0B_0N_0]}. \tag{20}$$

7.1 Property 3

Again, similarly to the Dependent Function in $1D$-space, one has:

a) If $(x, y) \in \mathrm{Int}(A_0M_0B_0N_0)$, then $K_{2D(x,y)} > 1$;

b) If $(x, y) \in \mathrm{Fr}(A0M0B0N0)$, then $K_{2D(x,y)} = 1$;

c) If $(x, y) \in \mathrm{Int}\,(AMBN - A_0M_0B_0N_0)$, then $0 < K_{2D(x,y)} < 1$;

d) If $(x, y) \in \mathrm{Fr}\,(AMBN)$, then $K_{2D(x,y)} = 0$;

e) If $(x, y) \notin AMBN$, then $K2D(x, y) < 0$.

8 General Case in 2D-Space

One can replace the rectangles by any finite surfaces, bounded by closed curves in 2D-space, and one can consider any optimal point O (not necessarily the symmetry center). Again, we assume the optimal points are the same for this nest of two surfaces. See Fig. 6.

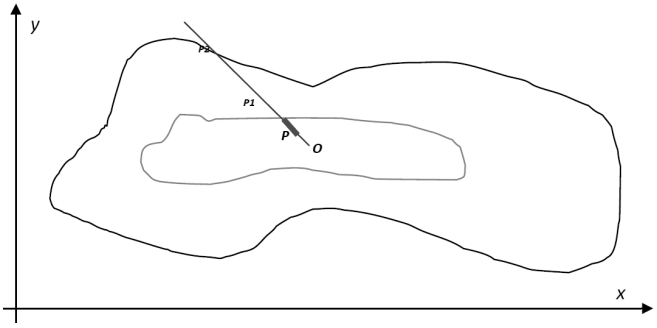

Fig. 6: Two included arbitrary bounded surfaces with the same optimal points situated in their common center of symmetry.

9 Linear Attraction Point Principle

We introduce the Attraction Point Principle, which is the following:

Let S be a given set in the universe of discourse U, and the optimal point $O \subset S$. Then each point $P\,(x_1, x_2, \ldots, x_n)$ from the universe of discourse tends towards, or is attracted by, the optimal point O, because the optimal point O is an ideal of each point. That's why one computes the extension $(n-D)$-distance between the point P and the set S as $\rho\,[(x_1, x_2, \ldots, x_n), S\,]$ on the direction determined by the point P and the optimal point O, or on the line PO, i.e.:

a) $\rho\,[(x_1, x_2, \ldots, x_n), S\,]$ is the negative distance between P and the set frontier, if P is inside the set S;

b) $\rho\,[(x_1, x_2, \ldots, x_n), S\,] = 0$, if P lies on the frontier of the set S;

c) $\rho\,[(x_1, x_2, \ldots, x_n), S\,]$ is the positive distance between P and the set frontier, if P is outside the set.

It is a king of convergence/attraction of each point towards the optimal point. There are classes of examples where such attraction point principle works. If this principle is good in all cases, then there is no need to take into consideration the center of symmetry of the set S, since for example if we have a 2D piece which has heterogeneous material density, then its center of weight (barycenter) is different from the center of symmetry. Let's see below such example in the 2D-space: Fig. 7.

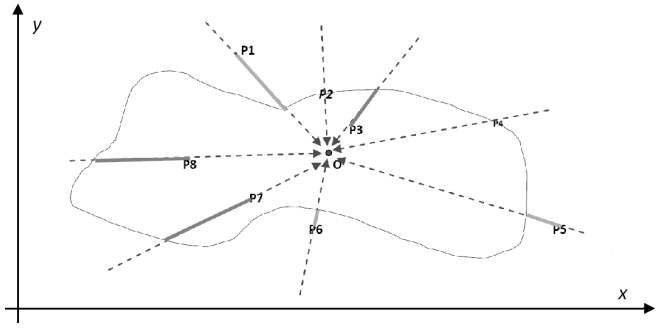

Fig. 7: The optimal point O as an attraction point for all other points $P_1, P_2, \ldots, P_8$ in the universe of discourse R^2.

10 Remark 1

Another possible way, for computing the distance between the point P and the closest point P' to it on the frontier (the rectangle's four edges) of the rectangle $AMBN$, would be by drawing a perpendicular (or a geodesic) from P onto the closest rectangle's edge, and denoting by P' the intersection between the perpendicular (geodesic) and the rectangle's edge. And similarly if one has an arbitrary set S in the 2Dspace, bounded by a closed urve. One computes

$$d(P, S) = \inf_{Q \in S} |PQ| \tag{21}$$

as in the classical mathematics.

11 Extension Distance in 3D-Space

We further generalize to 3D-space the Extension Set and the Dependent Function. Assume we have two points (a_1, a_2, a_3) and (b_1, b_2, b_3) in D. Drawing through A end B parallel planes to the planes' axes (XY, XZ, YZ) in the Cartesian system XYZ we get a prism $AM_1M_2M_3BN_1N_2N_3$ (with eight vertices) whose one of the transversal diagonals is just the line segment AB. Let's note by O the midpoint of the transverse diagonal AB, but O is also the center of symmetry of the prism.

Therefore, from the line segment AB in 1D-space, to a rectangle $AMBN$ in 2D-space, and now to a prism $AM_1M_2M_3BN_1N_2N_3$ in 3D-space. Similarly to 1D- and 2D-space, the prism may be closed (i.e. all points lying on its frontier belong to it), open (i.e. no point lying on its frontier belong to it), or partially closed (i.e. some points lying on its frontier belong to it, while other points lying on its frontier do not belong to it).

Then one computes the distance between a point $P\,(x_0, y_0, z_0)$ and the prism $AM_1M_2M_3BN_1N_2N_3$. One can do that following the same principle as Dr. Cai's:

— compute the distance in 3D (two dimensions) between the point P and the center O of the prism (intersection of prism's transverse diagonals);

— next compute the distance between the point P and the closest point (let's note it by P') to it on the frontier of

the prism $AM_1M_2M_3BN_1N_2N_3$ (the prism's lateral surface); considering P' as the intersection point between the line OP and the frontier of the prism, and taken among the intersection points that point P' which is the closest to P; this case is entirely consistent with Dr. Cai's approach in the sense that when reducing from $3D$-space to $1D$-space one gets exactly Dr. Cai's result;

— the Extension $3D$-Distance $d(P, AM_1M_2M_3BN_1N_2N_3)$ is $d(P, AM_1M_2M_3BN_1N_2N_3) = |PO| - |P'O| = \pm|PP'|$, where $|PO|$ means the classical distance in $3D$-space between the point P and O, and similarly for $|P'O|$ and $|PP'|$. See Fig. 8.

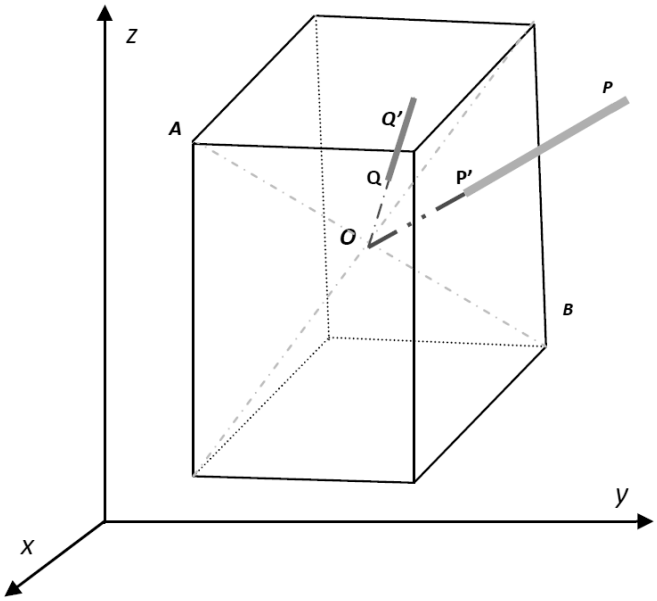

Fig. 8: Extension $3D$-Distance between a point and a prism, where O is the optimal point coinciding with the center of symmetry.

12 Property 4

a) $(x, y, z) \in \text{Int}\,(AM_1M_2M_3BN_1N_2N_3)$ if $\rho\,[(x, y, z), AM_1M_2M_3BN_1N_2N_3] < 0$, where $\text{Int}\,(AM_1M_2M_3BN_1N_2N_3)$ means interior of $AM_1M_2M_3BN_1N_2N_3$;

b) $(x, y, z) \in \text{Fr}\,(AM_1M_2M_3BN_1N_2N_3)$ if $\rho\,[(x, y, z), AM_1M_2M_3BN_1N_2N_3] = 0$ means frontier of $AM_1M_2M_3BN_1N_2N_3$;

c) $(x, y, z) \notin AM_1M_2M_3BN_1N_2N_3$ if $\rho\,[(x, y, z), AM_1M_2M_3BN_1N_2N_3] > 0$.

13 Property 5

Let $A_0M_{01}M_{02}M_{03}B_0N_{01}N_{02}N_{03}$ and $AM_1M_2M_3BN_1N_2N_3$ be two prisms whose sides are parallel to the axes of the Cartesian system of coordinates, such that they have no common end points, and $A_0M_{01}M_{02}M_{03}B_0N_{01}N_{02}N_{03} \subset AM_1M_2M_3BN_1N_2N_3$. We assume they have the same optimal points $O_1 \equiv O_2 \equiv O$ located in the center of symmetry of the two prisms.

Then for any point $(x, y, z) \in R^3$ one has

$$\rho\,[(x, y, z), A_0M_{01}M_{02}M_{03}B_0N_{01}N_{02}N]_{03} \geqslant \rho\,[(x, y, z)AM_1M_2M_3BN_1N_2N_3]\,.$$

14 The Dependent $3D$-Function

The last step is to devise the Dependent Function in $3D$-space similarly to Dr. Cai's definition of the dependent function in $1D$-space. Let the prisms $A_0M_{01}M_{02}M_{03}B_0N_{01}N_{02}N_{03}$ and $AM_1M_2M_3BN_1N_2N_3$ be two prisms whose faces are parallel to the axes of the Cartesian system of coordinates XYZ, such that they have no common end points in such a way that $A_0M_{01}M_{02}M_{03}B_0N_{01}N_{02}N_{03} \subset AM_1M_2M3BN_1N_2N_3$. We assume they have the same optimal points $O_1 \equiv O_2 \equiv O$ located in the center of symmetry of these two prisms.

The Dependent 3D-Function formula is:

$$K_{3D(x,y,z)} = \Big(\rho\,[(x, y, z), AM_1M_2M_3BN_1N_2N_3]\Big) \times \times \Big(\rho\,[(x, y, z), AM_1M_2M_3BN_1N_2N_3,] - - \rho\,[(x, y, z), A_0M_{01}M_{02}M_{03}BN_{01}N_{02}N_{03}]\Big)^{-1}. \quad (22)$$

15 Property 6

Again, similarly to the Dependent Function in $1D$- and $2D$-spaces, one has:

a) If $(x, y, z) \in \text{Int}\,(A_0M_{01}M_{02}M_{03}B_0N_{01}N_{02}N_{03})$, then $K_{3D}(x, y, z) > 1$;

b) If $(x, y, z) \in \text{Fr}\,(A_0M_{01}M_{02}M_{03}B_0N_{01}N_{02}N_{03})$, then $K_{3D}(x, y, z) = 1$;

c) If $(x, y, z) \in \text{Int}\,(AM_1M_2M_3BN_1N_2N_3 - -A_0M_{01}M_{02}M_{03}B_0N_{01}N_{02}N_{03})$, then $0 < K_{3D}(x, y, z) < 1$;

d) If $(x, y, z) \in \text{Fr}\,(AM_1M_2M_3BN_1N_2N_3)$, then $K_{3D}(x, y, z) = 0$;

e) If $(x, y, z) \notin AM_1M_2M_3BN_1N_2N_3$, then $K_{3D}(x, y, z) < 0$.

16 General Case in $3D$-Space

One can replace the prisms by any finite $3D$-bodies, bounded by closed surfaces, and one considers any optimal point O (not necessarily the centers of surfaces' symmetry). Again, we assume the optimal points are the same for this nest of two $3D$-bodies.

17 Remark 2

Another possible way, for computing the distance between the point P and the closest point P' to it on the frontier (lateral

surface) of the prism $AM_1M_2M_3BN_1N_2N_3$ is by drawing a perpendicular (or a geodesic) from P onto the closest prism's face, and denoting by P' the intersection between the perpendicular (geodesic) and the prism's face.

And similarly if one has an arbitrary finite body B in the $3D$-space, bounded by surfaces. One computes as in classical mathematics:

$$d(P, B) = \inf_{Q \in B} |PB|. \tag{23}$$

18 Linear Attraction Point Principle in $3D$-Space

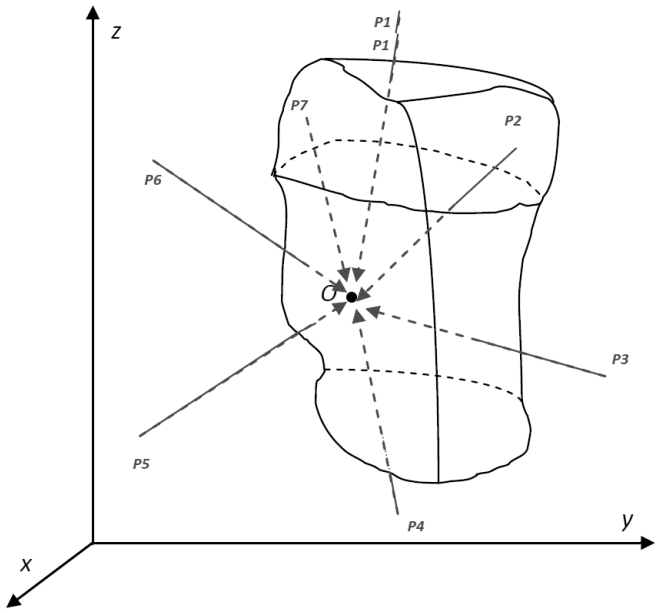

Fig. 9: Linear Attraction Point Principle for any bounded $3D$-body.

19 Non-Linear Attraction Point Principle in $3D$-Space, and in $(n-D)$-Space

There might be spaces where the attraction phenomena undergo not linearly by upon some specific non-linear curves. Let's see below such example for points P_i whose trajectories of attraction towards the optimal point follow some non-linear $3D$-curves.

20 $(n-D)$-Space

In general, in a universe of discourse U, let's have an $(n-D)$-set S and a point P. Then the Extension Linear $(n-D)$-Distance between point P and set S, is:

$$\rho(P, S) = \begin{cases} -d(P, P'), & P \neq 0,\ P \in |OP'| \\ \underset{P' \in \mathrm{Fr}(S)}{} \\ d(P, P'), & P \neq 0,\ P' \in |OP| \\ \underset{P' \in \mathrm{Fr}(S)}{} \\ -\max d(P, M), & P = 0 \\ \underset{P' \in \mathrm{Fr}(S)}{} \end{cases} \tag{24}$$

where O is the optimal point (or linearly attraction point); $d(P, P')$ means the classical linearly $(n-D)$-distance between two points P and P'; $\mathrm{Fr}(S)$ means the frontier of set S; and $|OP'|$ means the line segment between the points O and P' (the extremity points O and P' included), therefore $P \in |OP'|$ means that P lies on the line OP', in between the points O and P'.

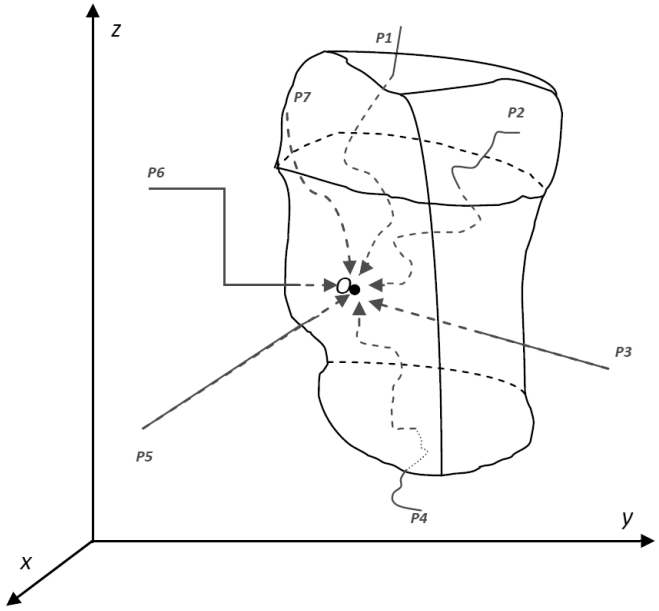

Fig. 10: Non-Linear Attraction Point Principle for any bounded $3D$-body.

For P coinciding with O, one defined the distance between the optimal point O and the set S as the negatively maximum distance (to be in concordance with the $1D$-definition).

And the Extension Non-Linear $(n-D)$-Distance between point P and set S, is:

$$\rho_c(P, S) = \begin{cases} -d_c(P, P'), & P \neq 0,\ P \in c(OP') \\ \underset{P' \in \mathrm{Fr}(S)}{} \\ d_c(P, P'), & P \neq 0,\ P' \in c(OP) \\ \underset{P' \in \mathrm{Fr}(S)}{} \\ -\max d_c(P, M), & P = 0 \\ \underset{P' \in \mathrm{Fr}(S),\ M \in c(O)}{} \end{cases} \tag{25}$$

where means the extension distance as measured along the curve c; O is the optimal point (or non-linearly attraction point); the points are attracting by the optimal point on trajectories described by an injective curve c; $dc(P, P')$ means the non-linearly $(n-D)$-distance between two points P and P', or the arc length of the curve c between the points P and P'; $\mathrm{Fr}(S)$ means the frontier of set S; and $c(OP')$ means the curve segment between the points O and P' (the extremity points O and P' included), therefore $P \in (OP')$ means that P lies on the curve c in between the points O and P'.

For P coinciding with O, one defined the distance between the optimal point O and the set S as the negatively maximum curvilinear distance (to be in concordance with the $1D$-definition).

In general, in a universe of discourse U, let's have a nest of two $(n-D)$-sets, $S_1 \subset S_2$, with no common end points, and a point P. Then the Extension Linear Dependent $(n-D)$-Function referring to the point $P(x_1, x_2, \ldots, x_n)$ is:

$$K_{nD}(P) = \frac{\rho(P, S_2)}{\rho(P, S_2) - \rho(P, S_1)}, \quad (26)$$

where is the previous extension linear $(n-D)$-distance between the point P and the $(n-D)$-set S_2.

And the Extension Non-Linear Dependent $(n-D)$-Function referring to point $P(x_1, x_2, \ldots, x_n)$ along the curve c is:

$$K_{nD}(P) = \frac{\rho_c(P, S_2)}{\rho_c(P, S_2) - \rho_c(P, S_1)}, \quad (27)$$

where is the previous extension non-linear $(n-D)$-distance between the point P and the $(n-D)$-set S_2 along the curve c.

21 Remark 3

Particular cases of curves c could be interesting to studying, for example if c are parabolas, or have elliptic forms, or arcs of circle, etc. Especially considering the geodesics would be for many practical applications. Tremendous number of applications of Extenics could follow in all domains where attraction points would exist; these attraction points could be in physics (for example, the earth center is an attraction point), economics (attraction towards a specific product), sociology (for example attraction towards a specific life style), etc.

22 Conclusion

In this paper we introduced the *Linear and Non-Linear Attraction Point Principle*, which is the following:

Let S be an arbitrary set in the universe of discourse U of any dimension, and the optimal point $O \in S$. Then each point $P(x_1, x_2, \ldots, x_n)$, $n \geqslant 1$, from the universe of discourse (linearly or non-linearly) tends towards, or is attracted by, the optimal point O, because the optimal point O is an ideal of each point.

It is a king of convergence/attraction of each point towards the optimal point. There are classes of examples and applications where such attraction point principle may apply.

If this principle is good in all cases, then there is no need to take into consideration the center of symmetry of the set S, since for example if we have a $2D$ factory piece which has heterogeneous material density, then its center of weight (barycenter) is different from the center of symmetry.

Then we generalized in the track of Cai Wen's idea to extend $1D$-set to an extension $(n-D)$-set, and thus defined the *Linear* (or *Non-Linear*) *Extension* $(n-D)$*-Distance* between a point $P(x_1, x_2, \ldots, x_n)$ and the $(n-D)$-set S as $\rho[(x_1, x_2, \ldots, x_n), S]$ on the linear (or non-linear) direction determined by the point P and the optimal point O (the line PO, or respectively the curvilinear PO) in the following way:

1) $\rho[(x_1, x_2, \ldots, x_n), S]$ is the negative distance between P and the set frontier, if P is inside the set S;
2) $\rho[(x_1, x_2, \ldots, x_n), S] = 0$, if P lies on the frontier of the set S;
3) $\rho[(x_1, x_2, \ldots, x_n), S]$ is the positive distance between P and the set frontier, if P is outside the set.

We got the following properties:

4) It is obvious from the above definition of the extension $(n-D)$-distance between a point P in the universe of discourse and the extension $(n-D)$-set S that:
   i) Point $P(x_1, x_2, \ldots, x_n) \in \mathrm{Int}(S)$ if $\rho[(x_1, x_2, \ldots x_n), S] < 0$;
   ii) Point $P(x_1, x_2, \ldots, x_n) \in \mathrm{Fr}(S)$ if $\rho[(x_1, x_2, \ldots x_n), S] = 0$;
   iii) Point $P(x1, x2, \ldots, x_n) \notin S$ if $\rho[(x_1, x_2, \ldots x_n), S] > 0$.
5) Let S_1 and S_2 be two extension sets, in the universe of discourse U, such that they have no common end points, and $S_1 \subset S_2$. We assume they have the same optimal points $O1 \equiv O2 \equiv O$ located in their center of symmetry. Then for any point $P(x_1, x_2, \ldots, x_n) \in U$ one has:

$$\rho[(x_1, x_2, \ldots x_n), S_2] \geqslant \rho[(x_1, x_2, \ldots x_n), S_1]. \quad (28)$$

Then we proceed to the generalization of the dependent function from $1D$-space to Linear (or Non-Linear) $(n-D)$-space Dependent Function, using the previous notations.

The *Linear* (or *Non-Linear*) *Dependent* $(n-D)$*-Function* of point $P(x_1, x_2, \ldots, x_n)$ along the curve c, is:

$$K_{nD}(x_1, x_2, \ldots, x_n) = \Big(\rho_c[(x_1, x_2, \ldots x_n), S_2]\Big) \times$$
$$\times \Big(\rho_c[(x_1, x_2, \ldots x_n), S_2] - \rho_c[(x_1, x_2, \ldots x_n), S_1]\Big)^{-1} \quad (29)$$

(where c may be a curve or even a line) which has the following property:

6) If point $P(x_1, x_2, \ldots, x_n) \in \mathrm{Int}(S1)$, then $K_{nD}(x_1, x_2, \ldots, x_n) > 1$;
7) If point $P(x_1, x_2, \ldots, x_n) \in \mathrm{Fr}(S1)$, then $K_{nD}(x_1, x_2, \ldots, x_n) = 1$;
8) If point $P(x_1, x_2, \ldots, x_n) \in \mathrm{Int}(S2 - S1)$, then $K_{nD}(x_1, x_2, \ldots, x_n) \in (0, 1)$;
9) If point $P(x_1, x_2, \ldots, x_n) \in \mathrm{Int}(S2)$, then $K_{nD}(x_1, x_2, \ldots, x_n) = 0$;
10) If point $P(x_1, x_2, \ldots, x_n) \notin \mathrm{Int}(S2)$, then $K_{nD}(x_1, x_2, \ldots, x_n) < 0$.

Submitted on July 15, 2012 / Accepted on July 18, 2012

References

1. Cai Wen. Extension Set and Non-Compatible Problems. *Journal of Scientific Exploration*, 1983, no. 1, 83–97; Cai Wen. Extension Set and Non-Compatible Problems. In: *Advances in Applied Mathematics and Mechanics in China*. International Academic Publishers, Beijing, 1990, 1–21.
2. Cai Wen. Extension theory and its application. *Chinese Science Bulletin*, 1999, v. 44, no. 7, 673–682. Cai Wen. Extension theory and its application. *Chinese Science Bulletin*, 1999, v. 44, no. 17, 1538–1548.
3. Yang Chunyan and Cai Wen. Extension Engineering. Public Library of Science, Beijing, 2007.
4. Wu Wenjun et al. Research on Extension Theory and Its Application. Expert Opinion. 2004, http://web.gdut.edu.cn/ĕxtenics/jianding.htm
5. Xiangshan Science Conferences Office. Scientific Significance and Future Development of Extenics — No. 271 Academic Discussion of Xiangshan Science Conferences, Brief Report of Xiangshan Science Conferences, Period 260, 2006, 1.

LETTERS TO PROGRESS IN PHYSICS

LETTERS TO PROGRESS IN PHYSICS

Routes of Quantum Mechanics Theories

Spiridon Dumitru
Department of Physics (retired), Transilvania University, B-dul Eroilor 29, 500036, Brašov, Romania
E-mail: s.dumitru42@yahoo.com

The conclusive view of quantum mechanics theory depends on its routes in respect with CIUR (Conventional Interpretation of Uncertainty Relations). As the CIUR is obligatorily assumed or interdicted the mentioned view leads to ambiguous, deficient and unnatural visions respectively to a potentially simple, mended and natural conception. The alluded dependence is illustrated in the attached poster.

Specification

The announced poster is a collage where some scientific ideas, suggested and argued in our papers [1,2], together with the known traffic signs, are figuratively pasted on the Popescu Gopo's cartoon "*Calea proprie*" ("*Proper route*") [3].

Submitted on February 24, 2012 / Accepted on March 03, 2012

References

1. Dumitru S. Reconsideration of the Uncertainty Relations and quantum measurements. *Progress in Physics*, 2008, v. 2, 50–68.
2. Dumitru S. Do the Uncertainty Relations really have crucial significances for Physics? *Progress in Physics*, 2010, v. 4, 25–29.
3. Popescu Gopo I. Filme, Filme, Filme… (Cartoons, Cartoons, Cartoons…) A booklet of cartoons, Ed. Meridiane, Bucharest 1963 (*in Rumanian*).

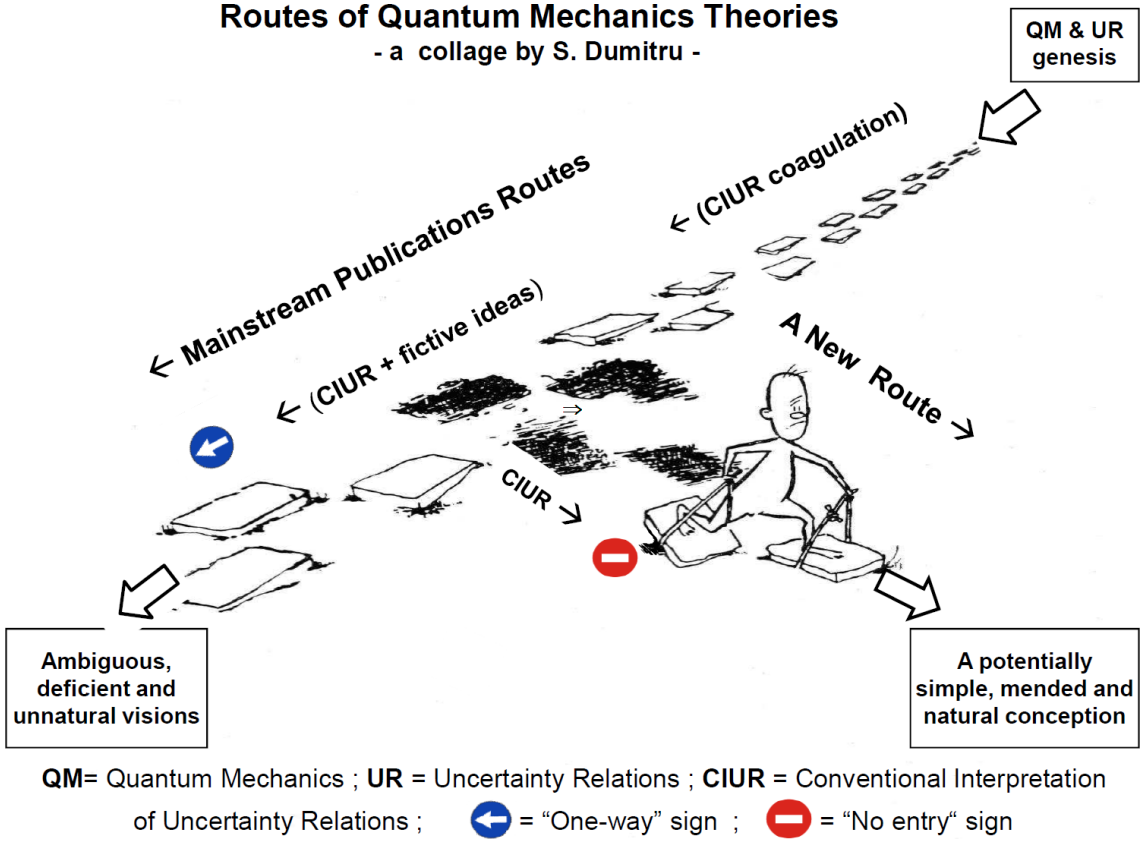

LETTERS TO PROGRESS IN PHYSICS

A Final Note on the Nature of the Kinemetric Unification of Physical Fields and Interactions

(On the occasion of Abraham Zelmanov's birthday and the near centennial of Einstein's general theory of relativity)

Indranu Suhendro
www.zelmanov.org

A present-day category of approaches to unification (of the physical fields) lacks the ultimate epistemological and scientific characteristics as I have always pointed out elsewhere. This methodological weakness is typical of a lot of post-modern "syllogism physics" (and ultimately the solipsism of such scientism in general). Herein, we shall once again make it clear as to what is meant by a true unified field theory in the furthest epistemological-scientific-dialectical sense, which must inevitably include also the natural kinemetric unity of the observer and physical observables.

Herein, I shall state my points very succinctly. Apart from the avoidance of absolutely needless verbosity, this is such as to also encompass the scientific spirit of Albert Einstein, who tirelessly and independently pursued a pure kind of geometrization of physics as demanded by the real geometric quintessence of General Relativity, and that of Abraham Zelmanov, who formulated his theory of chronometric invariants and a most all-encompassing classification of inhomogeneous, anisotropic general relativistic cosmological models and who revealed a fundamental preliminary version of the kinemetric monad formalism of General Relativity for the unification of the observer and observables in the cosmos.

1. A true unified field theory must not start with an arbitrarily concocted Lagrangian density (with merely the appearance of the metric determinant $\sqrt{-g}$ together with a sum of variables inserted by hand), for this is merely a way to embed — and not construct from first principles — a variational density in an ad hoc given space (manifold). In classical General Relativity, in the case of pure vacuum, i.e., $R_{\alpha\beta} = 0$, there is indeed a rather unique Lagrangian density: the space-time integral over $R\sqrt{-g}$, the variation of which gives $R_{\alpha\beta} = 0$. Now, precisely because there is only one purely geometric integrand here, namely the Ricci curvature scalar R (apart from the metric volume term $\sqrt{-g}$), this renders itself a valid geometric-variational reconstruction of vacuum General Relativity, and it is a mere tautology: thus it is valid rather in a secondary sense (after the underlying Riemannian geometry of General Relativity is encompassed). Einstein indeed did not primarily construct full General Relativity this way. In the case of classical General Relativity with matter and fields, appended to the pure gravitational Lagrangian density are the matter field and non-geometrized interactions (such as electromagnetism), giving the relevant energy-momentum tensor: this "integralism procedure" (reminiscent of classical Newtonian-Lagrangian dynamics) is again only tautologically valid since classical General Relativity does not geometrize fields other than the gravitational field. Varying such a Lagrangian density sheds no further semantics and information on the deepest nature of the manifold concerned.

2. Post-modern syllogism physics — including string theory and other toy-models (a plethora of "trendy salad approaches") — relies too heavily on such an arbitrary procedure. Progress associated with such a mere "sticky-but-not-solid approach" — often with big-wig politicized, opportunistic claims — seems rapid indeed, but it is ultimately a mere facade: something which Einstein himself would scientifically, epistemologically abhor (for him, in the pure Spinozan, Kantian, and Schopenhauerian sense).

3. Thus, a true unified field theory must build the spin-curvature geometry of space-time, matter, and physical fields from scratch (first principles). In other words, it must be constructed from a very fundamental level (say, the differential tetrad and metricity level), i.e., independently of mere embedding and variationalism. When one is able to construct the tetrad and metricity this way, he has a pure theory of kinemetricity for the universal manifold M: his generally asymmetric, anholonomic metric $g_{\alpha\beta}$, connection W, and curvature R will depend on not just the coordinates but also on their generally non-integrable (asymmetric) differentials: $\mathrm{M}(x, dx) \rightarrow \mathrm{M}(g, dg) \rightarrow \mathrm{W}(g, dg) \rightarrow R(g, dg)$. In other words, it becomes a multi-fractal first-principle geometric construction, and the geometry is a true chiral metacontinuum. This will then be fully capable of producing the true universal equation of motion of the unified fields as a whole in a single package (including the electromagnetic Lorentz equation of motion and the chromodynamic Yang-Mills

equation of motion) and the nature of pure geometric motion — kinemetricity — of the cosmos will be revealed. This, of course, is part of the the emergence of a purely geometric energy-momentum tensor as well. The ultimate failure of Einstein's tireless, beautiful unification efforts in the past was that he could hardly arrive at the correct geometric Lorentz equation of motion and the associated energy-momentum tensor for the electromagnetic field (and this is not as many people, including specialists, would understand it). In my past works (with each of my theories being independent and self-contained; and I do not repeat myself ever), I have shown how all this can be accomplished: one is with the construction of an asymmetric metric tensor whose anti-symmetric part gives pure spin and electromagnetism, and whose differential structure gives an anholonomic, asymmetric connection uniquely dependent on x and dx (and hence x and the world-velocity u, giving a new kind of Finslerian space), which ultimately constructs matter (and motion) from pure kinemetric scratch. Such a unified field theory is bound to be scale-independent (and metaphorically saying, "semi-classical"): beyond (i.e., truly independent of) both quantum mechanical and classical formalisms.

4. Such is the ultimate epistemology — and not just methodology — of a scientific construct with real mindful power (intellection, and not just intellectualism), i.e., with real scientific determination. That is why, the subject of quantum gravity (or quantum cosmology) will look so profoundly different to those rare few who truly understand the full epistemology and the purely geometric method of both our topic (on unification) and General Relativity. These few are the true infinitely self-reserved ones (truly to unbelievable lengths) and cannot at all be said to be products of the age and its trends. Quantizing space-time (even using things like the Feynman path-integrals and such propagators) in (extended) General Relativity means nothing if somewhat alien procedures are merely brought (often in disguise) as part of a mere embedding procedure: space-time is epistemologically and dialectically not exactly on the same footing as quantum and classical fields, matter, and energy (while roughly sharing certain parallelism with these things); rather, it must categorically, axiomatically qualify these things. Even both quantum mechanically and classically it is evident that material things possessed of motion and energy are embedded in a configuration space, but the space-time itself cannot be wholly found in these constituents. In the so-called "standard model", for example, even when quarks are arrived at as being material constituents "smaller than atoms", one still has no further (fundamental) information of the profounder things a quark necessarily contains, e.g., electric charge, spin, magnetic moment, and mass. In other words, the nature of both electromagnetism and matter is not yet understood in such a way. At the profoundest level, things cannot merely be embedded in space-time nor can space-time itself be merely embedded in (and subject to) a known quantum procedure. Geometry is geometry: purer, greater levels of physico-mathematical reality reside therein, within itself, and this is such only with the first-principle construction of a new geometry of spin-curvature purely from scratch — not merely synthetically from without — with the singular purpose to reveal a complete kinemetric unity of the geometry itself, which is none other than motion and matter at once. Again, such a geometry is scale-independent, non-simply connected, anholonomic, asymmetric, inhomogeneous: it ultimately has no "inside" nor "outside" (which, however, goes down to saying that there are indeed profound internal geometric symmetries).

5. Thus, the mystery (and complete insightful understanding) of the cosmos lies in certain profound scale-independent, kinemetric, internal symmetries of the underlying geometry (i.e., meta-continuum), and not merely in ad hoc projective, embedding, and variational procedures (including the popular syllogism of "extra dimensions").

"There are few who swim against the currents of time, living certain majestic smolderings and alien strengths as if they have died to live forever. There are so few who are like the vortex of a midnight river and the slope of a cosmic edge, in whose singularity and declivity the age is gone. There are fewer who are like a solid, unnamed, stepping stone in the heavy currents of the age of false light and enlightenment; as a generic revolutionary praxis goes, they'd rather be so black and coarse — solidly ingrained and gravitating — than smooth and merely afloat. But fewer still are those who are the thunder for all ages and in all voids: they are not grounded and sheltered on earth — they terrify it, — nor do they hang and dwell in the sky — they split it: — that light, so very few can witness its pure blinding longitude and touch its brief sublime density, is the truest Sensation (Sight-Sense, Causation-Reason) for real humanity to be the exact thing at the exact time in the Universe: itself."

Submitted on May 15, 2012 / Accepted on May 16, 2012

Progress in Physics is an American scientific journal on advanced studies in physics, registered with the Library of Congress (DC, USA): ISSN 1555-5534 (print version) and ISSN 1555-5615 (online version). The journal is peer reviewed and listed in the abstracting and indexing coverage of: Mathematical Reviews of the AMS (USA), DOAJ of Lund University (Sweden), Zentralblatt MATH (Germany), Scientific Commons of the University of St.Gallen (Switzerland), Open-J-Gate (India), Referential Journal of VINITI (Russia), etc. Progress in Physics is an open-access journal published and distributed in accordance with the Budapest Open Initiative: this means that the electronic copies of both full-size version of the journal and the individual papers published therein will always be acessed for reading, download, and copying for any user free of charge. The journal is issued quarterly (four volumes per year).

Electronic version of this journal: http://www.ptep-online.com

Postal address:
Department of Mathematics and Science,
University of New Mexico, 705 Gurley Avenue, Gallup, NM 87301, USA

Printed in the United States of America